Phase II Final Report
Early Stage Innovation
NASA Innovative Advanced Concepts (NIAC)

TRANSFORMERS FOR LUNAR EXTREME ENVIRONMENTS: Ensuring Long-Term Operations in Regions of Darkness and Low Temperatures

November 2017

Adrian Stoica, Brian Wilcox, Leon Alkalai,
Michel Ingham, Marco Quadrelli, and Robert Salazar
Jet Propulsion Laboratory, California Institute of Technology

and

Jim Mantovani, Kennedy Space Center

Including contributions from
Jim Henrickson and John Valasek, Texas A&M University

and

Joel Sercel, TransAstra

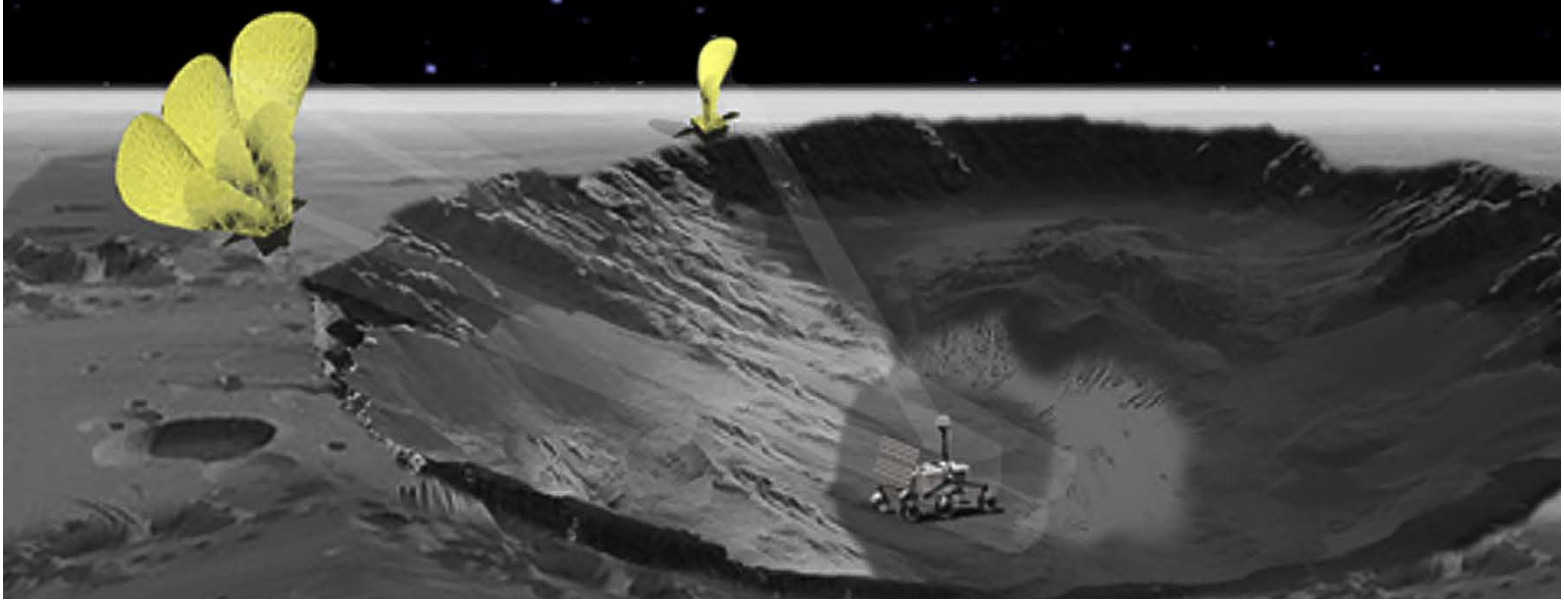

Acknowledgement

This research was carried out at the Jet Propulsion Laboratory, California Institute of Technology, under a contract with the National Aeronautics and Space Administration (NASA) and at the NASA Kennedy Space Center.

TRANSFORMERS FOR LUNAR EXTREME ENVIRONMENTS:

Ensuring Long-Term Operations in Regions of Darkness and Low Temperatures

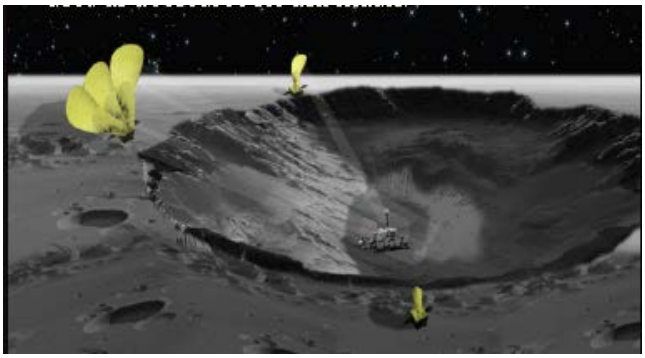

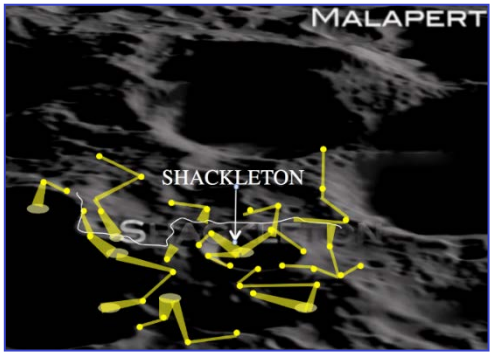

- This report shows how solar power could enable robotic operations in permanently shaded regions at lunar poles, to extract water ice and further produce liquid hydrogen and oxygen ($LH_2/LO_{2)}$ propellant.
- The power needs are derived from an Architecture for Human Exploration of Mars based entirely on lunar propellant. The extraction of 10 metric tons of water per day (at 10% water in regolith) requires ~0.6 MW thermal power. Additional ~2 MW electric power are required to produce 7.5 metric tons of LH_2/LO_2 propellant per day, as needed by the architecture.
- To provide power to processing equipment inside Shackleton Crater, optimal locations are determined on the crater rim, from which several reflecting TransFormers (TFs) would redirect sunlight, achieving a combined period of illumination of ~ 99% of the year.
- A single 40-m diameter reflector could provide up to 1 MW solar power. Inflatable rigidizable tower support structures raise reflectors above ground for better solar exposure. There are trade-offs: e.g., two reflectors at ground level would provide the same combined total illumination as a single tower ~100-m tall. Such a TF based on a 100-m tower made with inflatable 2-m beams and 40-m diameter reflectors would be of similar dimensions as an MSL-class rover (~1000 kg, 10 m^3). A TF-prospector rover combo could be designed and deployed in a Discovery-class mission searching for water.
- The TransFormers would be nodes of a Lunar Utilities Infrastructure that provides solar power year-round in the proximity of the pole, as well as local data transmission and intermittent direct to earth communications. This infrastructure would be instrumental in facilitating the development of a lunar economy.

Executive Summary: Main Findings and Recommendations

The Moon is a highly valuable asset in humanity's move beyond Earth. Its polar regions harbor some of the most valuable real estate in the solar system. The regions are rich in solar energy, as their elevated altitude and polar location (the rotation axis of the Moon is almost perpendicular to the incoming sunrays) enables them to see the Sun for extended periods of time. Their permanently shaded regions (PSRs), such as the polar craters, are also rich in water resources.

Yet, the Moon's natural environment is rather inhospitable for humans, as well as for equipment designed to operate on Earth, especially due to its freezing temperatures in areas that are not exposed to the Sun. The cold darkness restricts operations to 14 Earth days of exposure to sunlight (a lunar daytime), followed by 14 days of hibernation in the night, or to a few short hours, if robots venture into shaded areas like the polar craters powered only by batteries. Radioisotope thermal generators (RTGs) can ensure operation of certain classes of landers and rovers. However, each rover or asset deployed would need to carry one. They cannot satisfy the needs of power hungry equipment needed for mining and processing in-situ resources (MW).

There is, however, an intriguing alternative to warm up and power the robots, and illuminate the darkness: one can project solar energy into the area of exploration, *transforming the extreme environment (EE) of operation into a more hospitable one*. The transformation of the local environment around the robotic or human explorers could be done by TransFormers (TFs). This constitutes a novel approach to addressing NASA's Space Technology Grand Challenge of Surviving Extreme Environments. The simplest TFs would be reflective surfaces placed in Sun-illuminated places (e.g., on high ground, such as mountain peaks or rims of craters), which redirect sunlight onto the assets in the shaded areas, to power their solar panels, heat them, illuminate them and their surroundings, and relay communications.

The more sunlight is visible to TFs, the more it is potentially available to the assets they irradiate in the darkness. As a wider area gets illuminated, the sunlight can heat and power more than one asset operating in the light 'spot' at no additional cost. TFs also make possible the operation of multiple smaller rovers/probes, which are challenged to accommodate their own power due to their compact size. As such, TFs could enable lower-cost missions, with increasing cost benefits for repeated missions in the same area, and for powering/warming multiple rovers/vehicles/habitats.

TFs could redirect sunlight to locations kilometers away, e.g., from the rim of the lunar south pole's Shackleton Crater to its bottom, where it could ensure operations of both prospecting rovers and in situ resource utilization (ISRU) equipment. A 40-m diameter TF on the rim fully reflecting all incident solar radiation would provide an irradiation of ~300 W/m^2 at 10 km into the crater. A solar-powered MSL-class rover with 6 m^2 solar panels, operating inside the crater, would thus obtain the needed ~300 W electrical to move around and perform measurements, in what would otherwise be low 40–90 K temperatures. Ice water near the surface would take tens of minutes to sublimate under direct illumination of the soil, and longer for deeper ice deposits. Thus, short exposures, as may take place as 'side spill' during illumination of a rover as it traverses a region, should not impact the environment. On the other hand, in the absence of such concerns, concentrated heating from TFs could be used to sublimate water from the soil. In other words, rovers should not stop long over water deposits unless they are trying to extract the water; they should stop in rest areas or be prepared to protect the terrain otherwise, e.g., by using intermittent illumination, etc.

An important challenge in our study of the TF concept was to determine survivability in the PSR, by providing uninterrupted power (day and night, every day of the year). This was shown to be possible to a large extent: the projection of solar power from a set of TFs properly positioned on the rim of Shackleton Crater in an arrangement in which at least one is illuminated at any moment in time could ensure needed *quasi-continuous* illumination in specific areas where its rays can reach. Hours of darkness due to lunar eclipses are inevitable, and there is additional obstruction from some mountain peaks. Our study has examined trade-offs in the size, height, and number of TF reflectors. For example, either a single 1000 m^2 reflector at a height of 800 m, or an arrangement of two reflectors at 450 m, or of three reflectors at 300 m, could provide close to 99% continuous solar illumination within a few km from the reflectors; the coverage area depends on the topography (constrained by having a line of sight from the illuminated point on the ground to the reflectors). In principle, a single reflector, high enough to see the Sun continuously, and large enough so it is able to have the entire disc of the Sun seen at the locale of projection, would satisfy the requirements. However, by using multiple reflectors, the size of each reflector can be reduced, and the height at which they need to be positioned can be reduced because local obstructions of the Sun are mitigated. Energy storage is needed to deal with interruptions in sunlight, and it influences trade-offs. Ensuring higher energy storage capacity reduces the requirements on the height of the tower.

Another key challenge in our study was to consider the mass and volume constraints for packaging TFs for delivery to the surface of the Moon. The TFs need to be relatively low mass and low volume during transportation from Earth. Both Mylar and the more space-robust aluminized Kapton designs were analyzed. A TF reflector design with a Kapton layer, stowed using a spiral crease origami folding pattern weights 235 kg and fits in 1.34 m^3 volume. A tower over 100-m tall made of 2-m diameter inflatable beams to structurally support the reflectors was designed and analyzed. A 50 g/m^2 inflatable surface requires ~8 m^3 and ~900 kg, which means that a TF composed of the tower plus two 40 m-diameter reflectors could be built within the same mass and volume constraints of an MER-class rover A TF and a prospecting rover could be designed and deployed in a Discovery-class mission.

In addition to establishing the feasibility of TFs, examining trade-offs in their design, and analyzing their mass and volume packaging, the study focused on application of the TF concept to the development and maintenance of a Lunar Utilities Infrastructure at the lunar south pole. For this application, the amount of power to be projected relates to the amount of water needed in different scenarios. An affordable/sustainable humans-to-Mars architecture supported by lunar propellant was formulated during the study and indicates a need for 7.5 tons of propellant. To obtain it, it would require10 tons of water per day, for which an estimated ~0.6 MW thermal power (assuming 10% water in regolith), and, in a lossless transmission, ~0.6 MW solar power needs to be reflected. About 2 MW electric power, which may add to 6 MW of solar power reflected, would be needed for obtaining LH_2 and LO_2. From 10 km away, a 40-m diameter reflector would provide ~1.2 MW; a 100-m diameter would reflect ~8MW.

A more ambitious vision emerges. The TFs located on high ground could send energy to each other, not only to the energy ‘oases’ they are designed to illuminate. Energy could also reach the final destination through multi-hop relays. The network could extend tens of kilometers radially from the south pole (and similarly at the north pole). Such an energy infrastructure would be an enabler for establishing a Moon village and a true lunar economy. The energy infrastructure would to a large extent eliminate the extreme environment barrier. We would be able to send cheaper solar-powered robotic systems built for Earth-like conditions. Using this energy

infrastructure as the basis for establishing additional infrastructure for water and propellant processing would enable the lunar economy to truly flourish.

Contents

List of Figures

List of Tables

Acronyms

AAAI	Association for the Advancement of Artificial Intelligence
AGL	Above Ground Level
ALHAT	Autonomous Landing Hazard Avoidance Technology
AMIE	Advanced Moon Imaging Experiment
ATHLETE	All-Terrain Hex-Limbed Extra-Terrestrial Explorer
AU	Astronomical Unit
BLOS	Beyond Line-Of-Sight
CO	Crosslet Origami
CP	Crease Patterns
CPR	Circular Polarization Ratio
CRTS	Collapsible Rib-Tensioned Surface
DEM	Digital
DEP	Dielectrophoretic
DREAM	Dynamic Response of the Environment at the Moon
DRT	Dust Removal Tool
DSH	Deep Space Habitat
DSN	Deep Space Network
DTE	Direct To Earth
EAP	Electroactive Polymers
EDS	Electrodynamic Dust Shield
EE	Extreme Environment
EI	Flexural Rigidity
EML2	Earth-Moon Lagrangian point 2
ER	Exploration Rover
ESA	European Space Agency
GPR	Ground Penetrating Radar
HEO	High Earth Orbit
IEEE	Institute of Electrical and Electronics Engineers
ISRU	In-Situ Resource Utilization
JPL	Jet Propulsion Laboratory
KISS	Keck Institute of Space Studies
KSC	Kennedy Space Center
LAMP	Lyman Alpha Mapping Project
LED	Light Emitting Diode
LEO	Low Earth Orbit
LF	Lunar Flashlight
LH_2	Liquid Hydrogen
LLO	Low Lunar Orbit
LMO	Low Mars Orbit

LO_2	Liquid Oxygen
LOLA	Lunar Orbiter Laser Altimeter
LOS	Line-Of-Sight
LRO	Lunar Reconnaissance Orbiter
LROC	Lunar Reconnaissance Orbiter Camera
LUI	Lunar Utilities Infrastructure
MAV	Mars Ascent Vehicle
MER	Mars Exploration Rover
MSHAV	Mars Surface Habitat with Ascent Vehicle
MSL	Mars Science Laboratory
NASA	National Aeronautics and Space Administration
NIAC	NASA Innovative Advanced Concepts
NLSI	NASA Lunar Science Institute
NTR	New Technology Report
PSR	Permanently Shaded Regions
RASSOR	Regolith Advanced Surface Systems Operations Robot
RDS	Radio Data System
RF	Radio Frequency
RGD	Radiant Gas Dynamic
RP	Resource Prospector
RPR	Resource Prospector Rover
RTG	Radioisotope thermal generator
SC	Shackleton Crater
SCD	Screw Conveyor Dryer (aka Horizontal Agitator)
SMART	Small Missions for Advanced Research in Technology
SPI	Solar Power Infrastructure
STL	Stereo Lithography
TEI	Trans-Earth Injection
TRL	Technology Readiness Level
TF	TransFormer
TMI	Trans-Mars Injection
UHMWPE	Ultra High Molecular Weight Polyethylene
UV	Ultra-Violet
WAC	Wide Angle Camera
WEH	Water Equivalent Hydrogen
XRD	X-Ray Diffraction

1 Introduction

"If God wanted man to become a spacefaring species, he would have given man a moon."

Krafft Arnold Ehricke, Lunar Bases and Space Activities of the 21st Century (1985)

1.1 The Value of the Moon and of its South Pole

The polar regions of the Moon have been of interest for decades. Due to lunar orbital geometry (the inclination of the Moon's rotation pole to the ecliptic plane is 1.54 degrees), these regions are effectively in a state of perpetual twilight, in which the Sun continuously circles the horizon. The lighting conditions and the local relief result in certain areas being in constant darkness, while other areas in sunlight for the majority of the year (Bussey 2010).

Many authors have speculated that significant water exists in the permanently shadowed regions (PSRs) at the poles, such as the polar craters. According to Spudis, "both poles may contain several hundred million tons of water in the form of relatively 'clean' ice, all within the upper couple of meters of the lunar surface. The existence of significant water ice deposits enables both long-term human habitation of the Moon and the creation of a permanent cislunar space transportation system based upon the harvest and use of lunar propellant" (Spudis et al. 2013).

Hydrogen was identified in a polar PSR in the neutron spectrometry data from the Clementine mission and subsequent lunar orbiters (Williams 2012). Hydrogen abundances estimated from epithermal neutron counts are, in general, an average of 1.5% H_2O by mass within the PSRs (Feldman et al. 2001; Hayne et al. 2015). Many speculate that this hydrogen is in the form of water, either adsorbed as ice onto grains of regolith in the cold traps or as hydrated minerals (Colaprete).

Shackleton Crater, a permanently shadowed crater nearly coincident with the lunar south pole, has been a location of particular interest. Functioning as a cold trap, this crater represents a potential site of volatile accumulation, while areas of its rim see the Sun throughout the year with only small interruptions.

Orbital radar measurements of Shackleton Crater by the Miniature Radio Frequency (Mini-RF) radar instrument aboard the Lunar Reconnaissance Orbiter (LRO) set an upper limit of ~5–10 wt% (percentage by weight) for water ice within the uppermost meter of regolith (Thomson et al. 2012). Miller et al. (2014) indicate a hydrogen concentration of ~0.7 wt% water equivalent hydrogen (WEH) within tens of centimeters of the surface at Shackleton and are therefore consistent with the radar data (Sanin et al. 2017) show similar results though of a lower magnitude. **Figure 1.2** shows the map of the WEH abundance in wt% in the south polar region. The estimates for Shackleton seem to be at about half the value (~0.35 wt), thus up to 5 wt% for water ice. Other craters however, including Haworth, Shoemaker, and Faustini, as well as other polar regions seem to have double the amount.

Although the exact degree of volatile accumulation potential is disputed based on different measurements from different instruments and spacecraft (Zuber et al. 2012; Thomson et al. 2012; Miller et al. 2013, 2014; Feldman et al. 2001; Hayne et al. 2015; Sanin et al. 2017), the combination of in situ resource potential and energy availability has led to Shackleton Crater being frequently named as a potential location of a permanent lunar settlement (Al-Jammaz et al. 2004; Ohandev et al. 2001; Schrunk et al. 2007). In plans, many times delayed for financial

reasons, NASA has named the rim of Shackleton as a potential candidate for a permanent lunar base, targeted for continuous operation by 2020, and continually manned by astronauts by 2024. In recent news, the Trump administration has expressed interest in resuming funding for these missions.

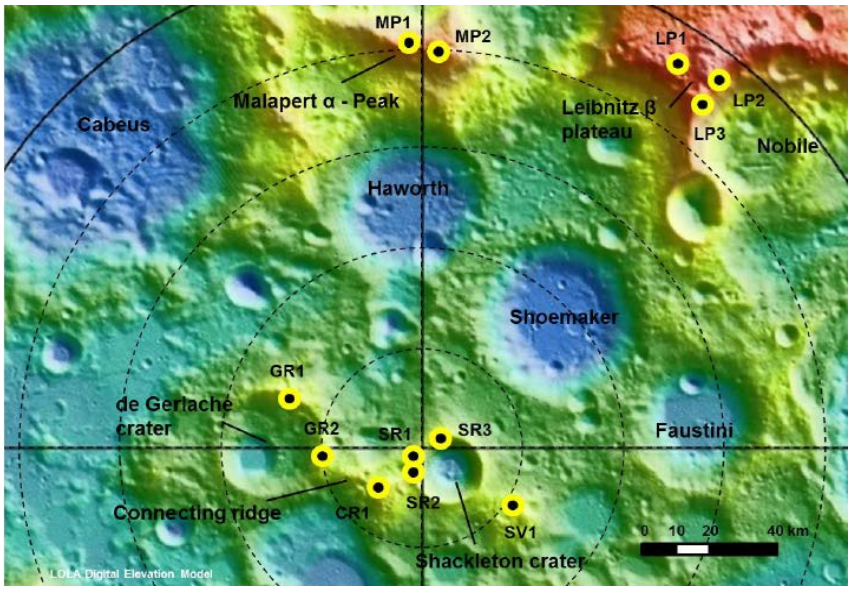

Figure 1.1. Map of the Moon's south polar region based on LOLA data (De Rosa 2012).

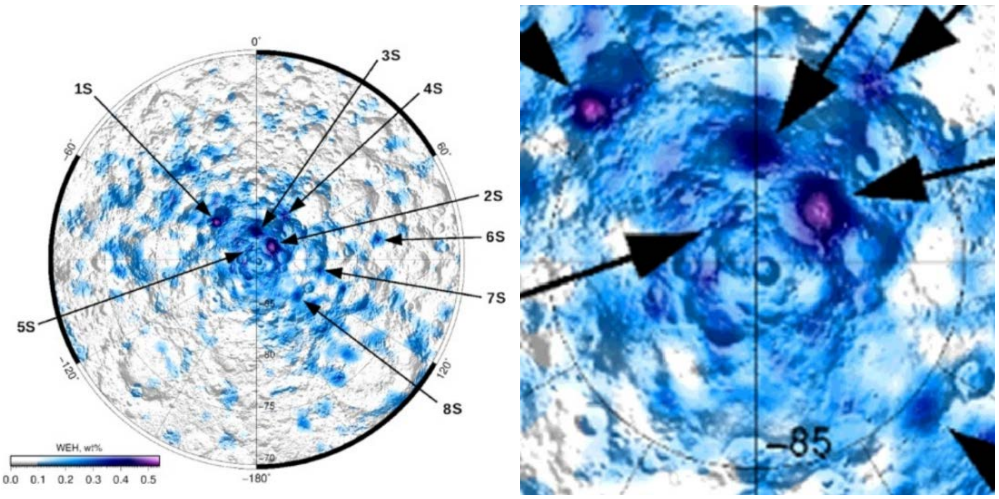

Figure 1.2. WEH abundance in the regolith distribution in the lunar south pole (Sanin et al. 2017). The image on the right is a zoom-in of the image on the left, around the center part, which is the south pole. Highest WEH concentrations are shown in areas marked by arrows.

Figure 1.3 provides topographical maps of Shackleton Crater. Located at center coordinates of 89.54°S latitude and 0.0° E longitude, the rotational axis of the Moon lies within the crater (about 150 m away from the rim). The crater is approximately 20.7-km wide and 4.2-km deep. The slope towards the interior is about 30° downward towards the crater floor, which is about 6.4 km in diameter.

The intensity of solar energy reaching the lunar surface is 1366 W/m^2; there is no atmosphere and hence no associated atmospheric loss.

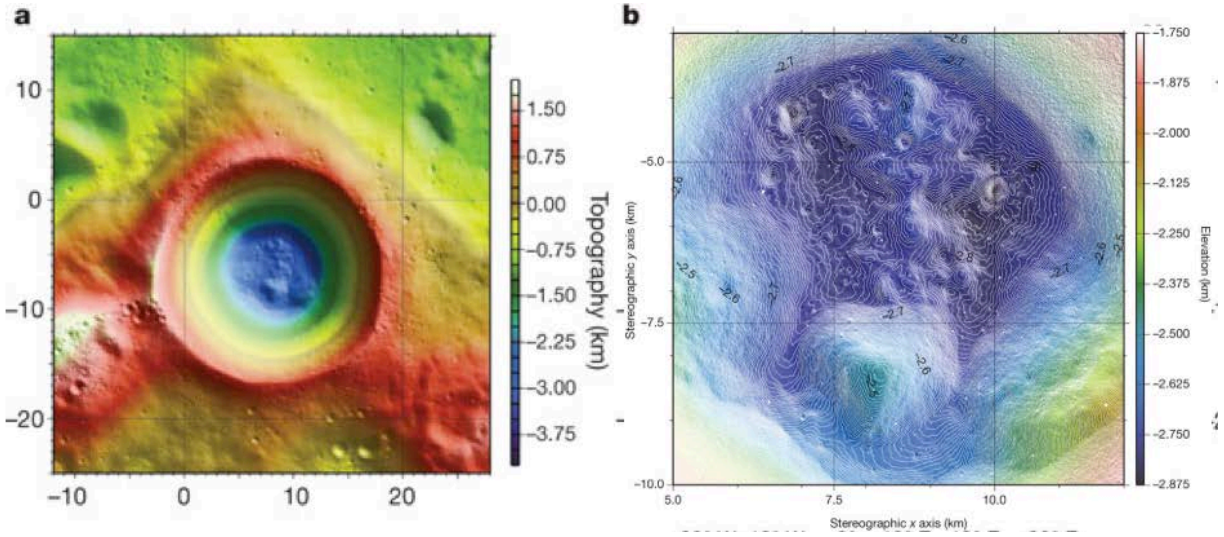

Figure 1.3. (a) Topography of SC sampled at 10-m spatial resolution; Elevations are contoured at 5-m intervals with colors indicating elevation with respect to 1,737.4 km. (b) a more detailed view of the topography of Shackleton's floor, which highlights the irregularly distributed deposits and numerous small craters (Bryant 2010)

The SC floor is never illuminated while the peak along the rim is illuminated by sunlight around 90% of the time. This makes the rim an ideal location for capturing/using the sunlight. Previous solutions were proposed for using solar panels that would convert light into electrical energy. The possibility of reflecting sunlight for illumination was suggested by Bryant (Bryant 2010), though no analysis was performed. A map of yearly average illumination is shown in **Figure 1.4** (Bryant 2010). **Figure 1.5** shows a map with candidate base sites, points As and Bs. In this discussion, we will focus in particular on points on the rim, thus the sites A1–A4 are most relevant. We will also discuss site B1 in a later analysis in this report.

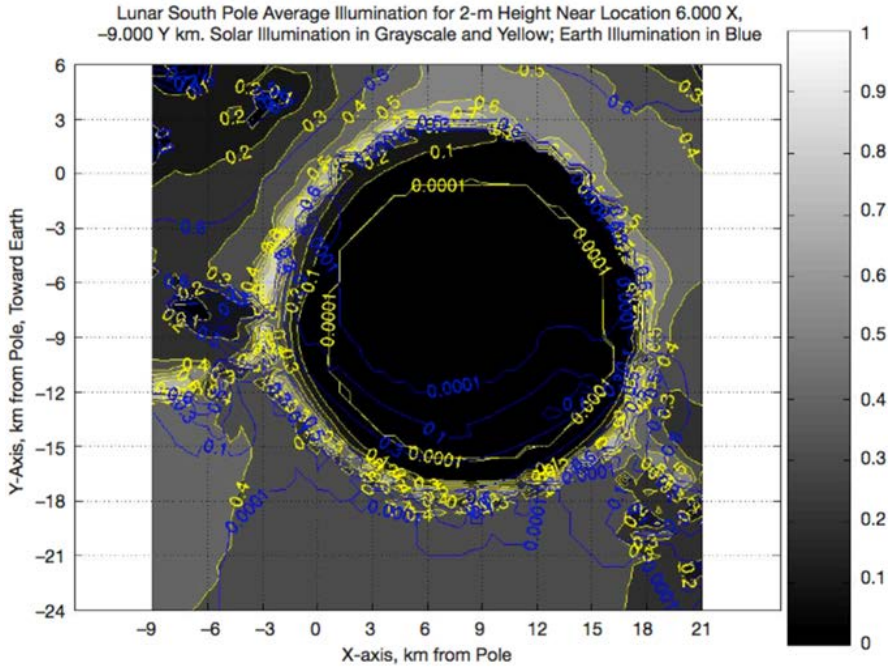

Figure 1.4. Shackleton Crater map of yearly average illumination, showing almost permanent illumination on the rim (Bryant 2010).

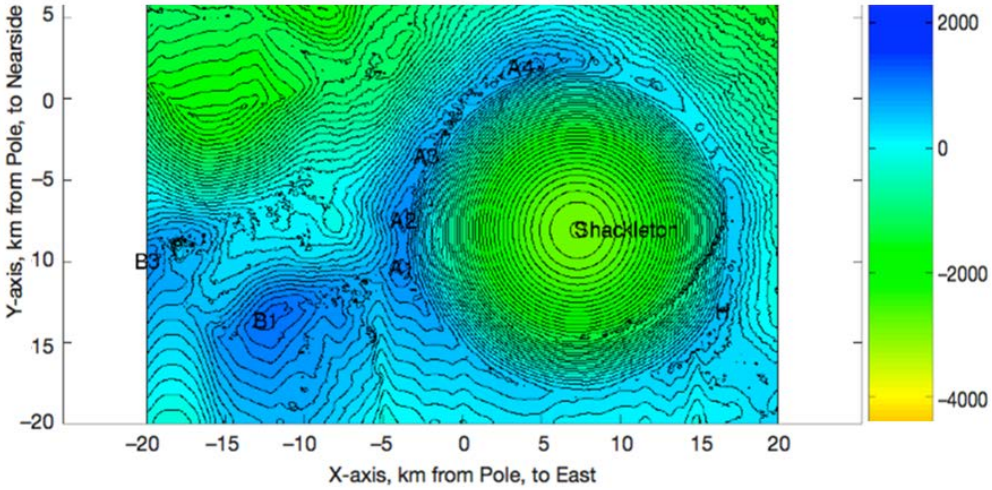

Figure 1.5. Shackleton Crater topographic map, with base sites (Bryant 2010).

The data in **Tables 1.1** and **1.2** provide illumination information for the Shackleton Crater area.

Table 1.1. Fine-resolution solar illumination statistics (top) with definitions (bottom).

			Multiyear Average Illumination (% of Sun Visible)			Months 100% Visible (% of Sun Visible)			Days Dark in Winter Month (% of Sun Visible)			Days Longest Continuous Darkness (% of Sun Visible)		
Site	X, km	Y, km	(0)	(50)	(100)	(0)	(50)	(100)	(0)	(50)	(100)	(0)	(50)	(100)
A1	−3.720	−10.440	93.46	90.36	86.31	4.05	2.98	1.92	8.94	12.06	15.99	2.46	2.71	5.50
A2	−3.680	−7.520	92.98	89.47	84.83	4.46	3.40	2.34	10.58	13.70	18.29	2.63	2.79	3.04
A3	−2.200	−3.560	85.36	80.75	75.22	0.05	0.00	0.00	14.03	18.37	20.43	4.92	8.86	9.19
A4	3.720	1.910	87.83	83.66	78.51	0.00	0.00	0.00	13.21	17.06	19.85	6.23	7.63	9.92
B1	−12.400	−13.680	97.01	94.79	91.67	8.02	6.96	5.90	6.32	9.59	11.73	2.79	4.10	7.54

Multiyear Illumination	0 % solar disk visible—the amount of time that any solar light is available; 50% solar disk visible represents half-strength solar illumination; 100% solar disk visible represents the percentage of the multiyear interval with full solar power available
Dark Days in Winter Months	Number of days during south pole winter with less than specified % of solar disk visible. For 0% of solar disk visible—sum of days without any solar light
Days Longest Darkness	Longest continuous period without solar power. For 0% of solar disk visible, this is the longest continuous period without any solar light. For 100%, this is the longest continuous period without full solar power
Battery Storage Considerations	Worst-case scenario: days dark in winter month associated with 100 percent of solar disk visible

Table 1.2. Solar illumination metrics for site B1 tower heights (selection to 1,000 m, from (Bryant 2009)).

Tower height	Solar illumination statistics, Assumed uniform distribution Multi-year average illumination		
meters	(0%)	(50%)	(100%)
2.0	97.01	94.79	91.67
4.0	97.11	94.91	91.81
8.0	97.24	95.08	91.99
16.0	97.42	95.35	92.29
32.0	97.60	95.67	92.69
64.0	97.89	96.15	93.41
128.0	98.21	96.79	94.56
256.0	98.56	97.46	95.74
500.0	98.90	98.14	96.90
1000.0	99.38	98.72	97.93

No single point on Shackleton rim, sees 100% of the solar disk more than ~86.3% of the time. The longest period of continuous (total) darkness for the best point is 2.46 days in a year, and the longest period of partial darkness (<100% solar illumination) is 5.5 days. Note that **Table 1.2** indicates an increase of ~2% in B1 for ~800 m elevation by a tower; it is probable that the same would apply to towers on the rim, which is confirmed in this study. Certain locations are especially precious, as one would be able to obtain maximum solar energy and redirect it with reduced costs. More details about the illumination are presented in our Phase 1 report (Stoica et al. 2014) and later in Chapter 4 of this report. The availability of both solar power and water deposits makes the polar region very valuable. This is expressed by Spudis as follows: "All of this new lunar data has countries around the world planning ways to access the energy and resource bonanza at the poles of the Moon available to those who arrive first" ("The Value of the Moon", Spudis 2016, p.14). Furthermore, he writes: "Prime locations on the Moon […] are not limitless, and access to and use of the most desirable and valuable sites for resource prospecting and harvesting may become contentious." (Spudis 2016, p.182)

1.2 TransFormers

Imagine an oasis of warm sunlight surrounded by a desert of freezing cold darkness. Robots inside the oasis perform scientific lab analyses and process icy regolith brought from excavations in the neighboring darkness. This oasis, about the size of a football field, lies in a valley about twice the size of Washington DC, surrounded by peaks the size of Mount Rainier. From its low angle on the horizon, the Sun's rays never shine over the peaks into the valley, until heliostats unfold on these peaks and redirect the rays down to form the oasis of sunlight. This place becomes a large science laboratory and the largest off-Earth producer of liquid hydrogen and liquid oxygen for fueling inter-planetary trips. This is the Shackleton Crater at the lunar south pole and TransFormers are the heliostats projecting sunlight onto the oasis. *This is the vision we propose to bring to life.*

Surviving extreme environments (EEs) is one of the main challenges of in-situ space exploration, both robotic and human. Providing remotely controlled protection to the in-situ explorers of EE, *projecting and controlling an ameliorated micro-environment* around them, is a novel idea, with *potential broad implications for both robotic and future human spaceflight.*

The TransFormers concept (Stoica et al. 2014) is a paradigm shift to operating in EEs. TFs are systems that direct energy into energy-starved (extreme) environments, *transforming* them, locally around robots or humans, into hospitable micro-environments. The TF itself undergoes shape transformation when unfolding from a compact package to a large reflective array. It makes sure the reflected sunlight reaches the solar panels of robots down in the crater and provides power. The robots would no longer need blankets and RTG heaters to survive the cold darkness.

The Phase I study examined the concept in the context of a mission scenario at Shackleton Crater (**Figure 1.6)** in which a rover transports a compactly folded TF from a landing module to the rim, then descends into the crater. The TF unfolds to reflect sunlight into the crater—it is placed at a location that provides line-of-sight coverage of the planned rover path. As the rover reaches areas with ambient temperatures below 100 K, it is powered and warmed by the TF projected energy. TFs would also act as communication relays and would have embedded solar cells for powering their own operation.

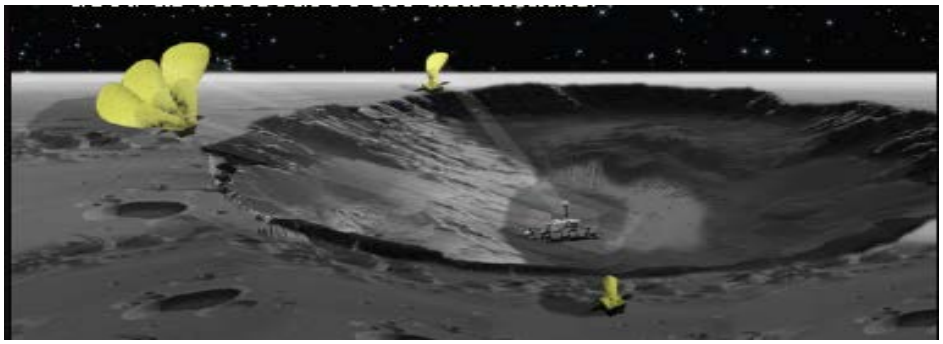

Figure 1.6. Lunar south pole crater: TransFormers on the rim, projecting a favorable micro-environment to the rover (artist's view).

Projection at a distance of many kilometers results in a reduced solar intensity for a rover with angular size (relative to mirror) less than that of the Sun (9.3 mrad). In this case, the rover only sees part of the Sun reflected, hence receives only a fraction of the incoming sunlight. The solar intensity at some distance from the reflector depends on how much of the solar disk is seen in the reflector from a point at that distance.

Bringing sunlight to target areas has been successfully demonstrated on Earth. The town of Rjukan, in Norway, is situated in a deep valley where mountains block the Sun's rays for months. The town has built computer-controlled mirrors that track the Sun and reflect sunlight downwards. Rjukan mirror reflects a 600-square-meter beam of sunshine into the town square below, as seen in **Figure 1.7**.

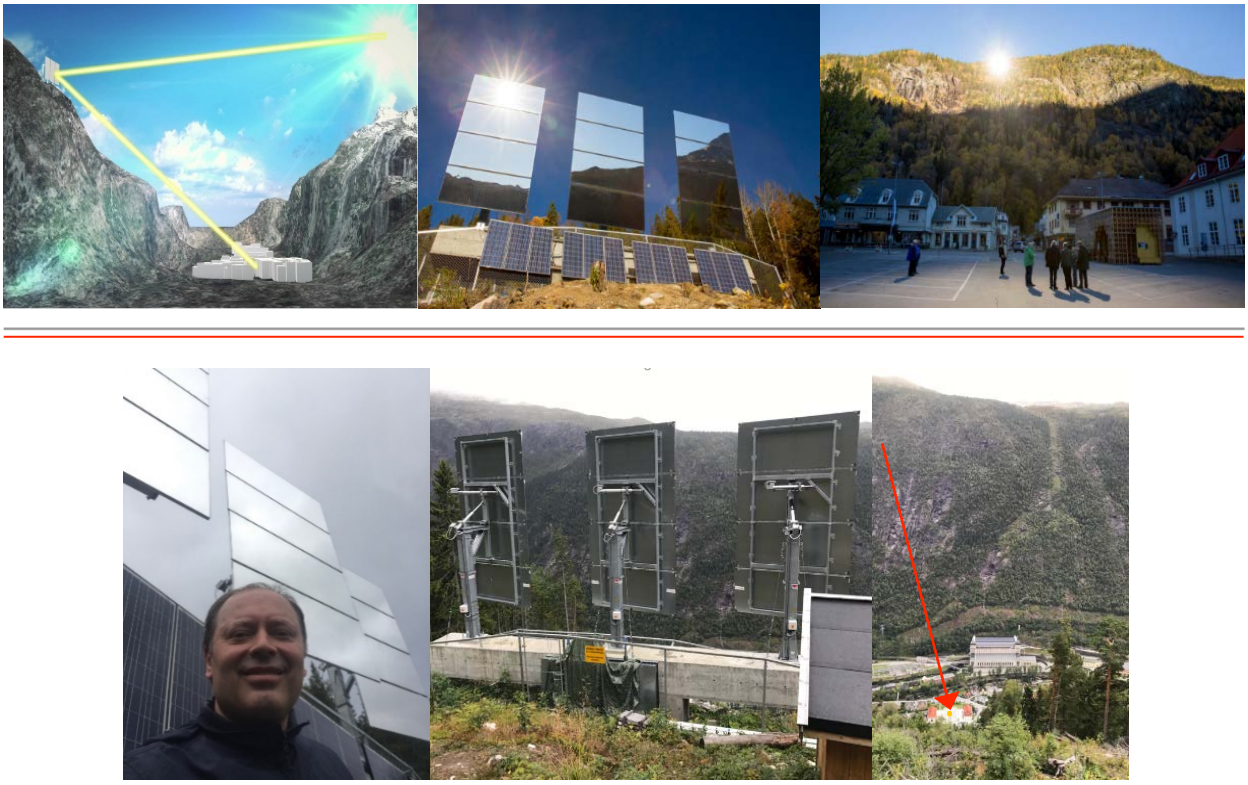

Figure 1.7. Top row: Heliostats illuminating towns in deep valley at Rjukan, Norway. Bottom row: NIAC Fellow Stoica, after a hike at Rjukan, next to the mirrors; back of mirrors and location where sunrays are redirected in town plaza, at ~700 m away from the mirrors.

The Phase I study analyzed the concept of TFs in the context of craters on the Moon and Mercury, and lava tubes on Moon and Mars. The study concluded that the most promising avenue was to focus on the Moon's permanently shaded polar craters. Thus, the main results of Phase I are enumerated in the following.

The analysis determined that it is possible to power and keep warm an MSL-class exploration rover 10 km away in the 20-km-diameter Shackleton Crater (SC), using a 40-m diameter (~1,250 m^2 surface) TF to project 300 W/m^2 onto 6 m^2 solar panels at 16% efficiency, sufficient to provide the ~300 W electric power needed to operate the rover. A 10-m-diameter TF is able to provide nearly full solar irradiation up to 1 km distance.

A first order estimate indicates that a 1,200 m^2 surface could be packed within 1 m^3, and could weigh ~100 kg. The study offered promise that needed functionality can be packed into a sub-mm thick layer, and large surfaces can be compactly packed and unpacked, origami style. The surface would need to be highly reflective (95% or better), with ~1 mm/m maximum surface deviation, and tolerance in the mirror segment tilt of 0.5 mrad.

An unanticipated finding was the understanding that such a reflector could power not only a single rover, but even *dozens* of MSL-class rovers operating in the illuminated footprint which receives in total over 1 MW from the 40-m diameter reflector. (The size of the footprint at 10 km would be over 5,000 m^2 in cross-section of reflected beam, more on the ground, depending on local angle of the receiving surface). It could power and warm up small rovers or devices that cannot carry RTGs. This insight encouraged the team to propose for Phase II a more ambitious

mission scenario, not only creating a micro-environment around a single exploration rover, but forming an entire 'oasis' where equipment for ISRU can also operate.

It is worth making a reference to the Lunar Flashlight (LF) mission, illustrated in **Figure 1.8**. Its objective is to project sunlight into a permanently shadowed lunar crater by using the reflection from its solar sail. At launch, the sail is packed in a 6-u CubeSat (1 u = 10×10×11 cm) that then unfolds to an 80 m^2 surface, which acts as a reflector. In many respects, one can consider LF as a precursor to a TF mission, as sunlight would be redirected by a reflector that deploys from a compact package. The objective here is simply illumination, as the power reaching the surface from 20 km (lowest orbit) is fraction of a Watt, about 3 orders less power than TFs (which are larger and closer) would reflect.

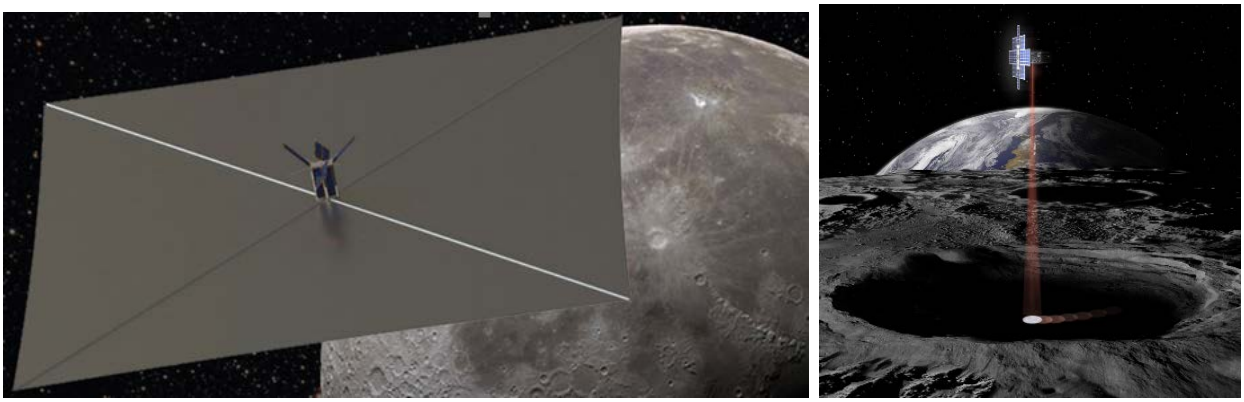

Figure 1.8. Lunar Flashlight solar sail reflecting sunlight into a shaded crater on the Moon. Image credits: NASA. Source: http://sservi.nasa.gov/articles/lunar-flashlight/

1.3 Study Objectives and Outline of the Worked Performed

The Phase II study had two objectives. The first objective was to advance the TF concept in the context of a lunar mission inside SC, to power, heat, and illuminate robotic operations enabling prospecting/excavation of lunar volatiles in the icy regolith, and to perform ISRU to extract water and produce LH_2/LO_2. We analyzed using TFs to power/heat/illuminate three classes of rovers: Resource Prospector (Andrews 2014), MSL, and Athlete (Wilcox 2007). We also assessed three methods of ISRU to extract water and evaluated their respective power needs.

An important outcome of this study is an architecture for affordable and sustainable human missions to Mars using lunar-produced propellant (Wilcox 2017). The architecture requires 7.5 metric tons (t) per day of LH_2/LO_2 propellant, for which 10 t/day water needs to be extracted. Based on the ISRU equipment power needs, at 10% water in regolith, an estimated 0.6 MW thermal power is needed to extract the water, and 2 MW electric for electrolysis, which at ~30% conversion efficiency brings the total to ~7 MW of solar power redirected into the crater. If reflecting from 10 km away (considered here conservative) a 40-m reflector would provide ~1 MW. Either a multitude of reflectors or larger ones (an 80-m-diameter would provide ~4 MW, while a 100-m-diameter would provide ~5 MW).

An important challenge in our study of the TF concept was to determine if one can ensure survivability in the cold, by providing uninterrupted power (day and night, every day of the year). This was shown to be possible to a large extent: projection of solar power from a set of TFs properly positioned on the rim of Shackleton Crater in an arrangement in which at least one is illuminated at any moment in time could ensure needed *quasi-continuous illumination (i.e.,*

only a few hours of total darkness) in specific areas where its rays can reach. Our study has examined trade-offs in the size, height, and number of TF reflectors. For example, either a single 1,000 m^2 reflector at a height of 800 m, or an arrangement of two reflectors at 450 m, or of three reflectors at 300 m, could provide ~99% continuous solar illumination within a few km from the reflectors; the coverage area depends on the topography-constrained line of sight from the illuminated point on the ground to the reflectors). In principle, a single reflector, high enough to see the Sun continuously, and large enough so it is able to have the entire disc of the Sun seen at the locale of projection, would satisfy the requirements. However, by using multiple reflectors, the size of each reflector can be reduced, and the height at which they need to be positioned can be reduced because local obstructions of the Sun are mitigated. This TF-based solar power infrastructure provides sunlight year-round to a target area within the crater, transforming an area of perpetual darkness into an "energy oasis." Tall mountains, such as Malapert and Leibnitz, obscure the Sun for hours; in addition, the Earth blocks the Sun during lunar eclipses (two to five times a year lasting ~4 hours). These interruptions, fortunately not too long, emphasize the need for storing energy. The higher the capacity for energy storage, the less stringent the requirements on the height positioning of the TF. We determined that an interesting option would be thermal storage using a modified Magaldi system (Magaldi 2015) using lunar dust as a thermal agent.

The study shows it is feasible to build the elements of such a power infrastructure. A more grandiose vision can be imagined. The TFs located on high ground could send energy to each other (not only to the energy oases they are designed to illuminate); energy could also reach its final destination through multi-hop relays. A true "ring of power" could be established around the rim of Shackleton Crater. Moreover, the network could extend tens of kilometers radially from the pole. A similar infrastructure can be established at the north pole.

The second objective was to advance the feasibility of TFs by performing a point design of a scalable TF that packs in a cube ~1 m on the side, weighs ~100 kg, unfolds to over 1,000 m^2 of reflective surface, with over 95% long-term reflectivity, and is robust to dust obscuration.

Several designs were analyzed, initially with Mylar, then with more space-robust aluminized Kapton. A TF reflector design with a Kapton layer, stowed using a spiral crease origami folding pattern has a mass of 235 kg and fits in 1.34 m^3 volume. A 133-m tall tower made of 2-m-diameter inflatable beams to structurally support the reflectors was designed and analyzed. A conservative 500g/m^2 inflatable material requires ~ 35 m^3 volume when packed, with a mass of ~8,000 kg. A 50 g/m^2 reflecting surface requires ~8 m^3 and ~900 kg, which means that a TF composed of the tower plus two 40 m-diameter reflectors could be built within the same mass and volume constraints of an MER-class rover and could be deployed, with a prospecting rover, in a Discovery-class mission.

This report contains the analysis and findings of the study, and is organized as follows:

Section 2 explores the power needs driving the architecture and sizing of the energy infrastructure. Specifically, it discusses the power needs for exploration and prospecting rovers and for ISRU. A Mars architecture with fuel from the Moon is introduced, which determines production needs. A brief analysis of the needs associated with launching from the Moon is also considered.

Section 3 examines the core element of the infrastructure—the TF. An economically feasible solution requires low mass and low volume during transport from Earth; thus, compactly stowed reflectors, deploying, for example, in origami folding patterns and telescopic/inflatable designs are analyzed, the robustness of designs is also discussed.

Section 4 addresses the infrastructure network of TFs. An analysis identifying optimal pairs of reflectors is performed, searching across optimal locations, height, and size of reflectors. Solutions for continuous illumination of locations both inside and outside SC are determined.

Section 5 summarizes the findings, presents a vision and possible technology roadmap.

2 Power Needs for Obtaining Water and LH_2/LO_2 Propellant

2.1 Scenario of Operations inside Shackleton Crater

As mentioned in Chapter 1, there is still debate about the distribution, abundance, its composition, etc. In this report, we consider values from a conservative 1% of water to a more optimistic 5–10% as in Spudis (2013). A smaller percentage may require more energy for extraction, which may be achieved by scaling up the power infrastructure but also, for example, by allowing for more time or larger collectors and concentrators, or improving conversion efficiencies.

To determine the amount of power required, we need to estimate the amount of water needed. This depends on assumptions on the amount of propellant needed. The current Mars architectures indicate 500 metric tons (t) per year (Lavoie 2016); informal discussions point to more, ~1,000 t per year. During this study, Co-Investigator (Co-I) Wilcox has proposed an affordable/sustainable architecture for human exploration of Mars fully powered by lunar propellant. The Wilcox architecture (Wilcox 2017) requires 7.5 t/day of LH_2/LO_2 propellant at a common O_2:H_2 mass ratio of 6:1 as used in rocket engines, which translates to *10 t per day of ISRU water extracted at the lunar poles*. Over an entire year, this adds to ~3,650 t, roughly 4 times the amount of the highest previous estimates. We will baseline using the more demanding Wilcox architecture.

The power needs are analyzed in two kinds of mission contexts: prospecting rovers and ISRU. A preliminary mission analysis in the Phase I study identified the following scenario: a lander delivers a rover, carrying a TF, in the proximity of the rim. The rover carries a compactly packed TF to a predetermined favorable position on the rim, where the TF unfolds and starts reflecting sunlight to help the rover. It allows the rover to characterize/map the crater before it goes in, and determines/plans a safe traverse path. A solarly charged, heliostat, autonomous with supervisory control from Earth, the TF deploys the surface needed and changes shape/orientation as heliostat/rover tracker. The rover descends into the crater, while being illuminated by the TF. In one scenario, the same rover can return to the rim and help position another TF, when a later one is landed. An alternative is to deploy, on a subsequent mission, a service rover with the role of rim operations, positioning and servicing TFs and possibly acting as a mobile relay on the rim. Some later prospecting rovers could be deployed directly in the crater.

The rover reaches regions of below 100 K, where the power projected by the TF is mission-enabling. The TF points the reflected energy into rover solar arrays, controls the spots of light for the rover to examine its surroundings and to take measurements, and acts as a communication relay. The TF can relay to an orbiter, or a surface relay on Malapert or Leibnitz Mountain, with permanent direct view to Earth, or it could transmit direct to Earth, which in fact, for cost reasons, is the preferred scenario for the first TF missions.

The scenario is illustrated in the following figures.

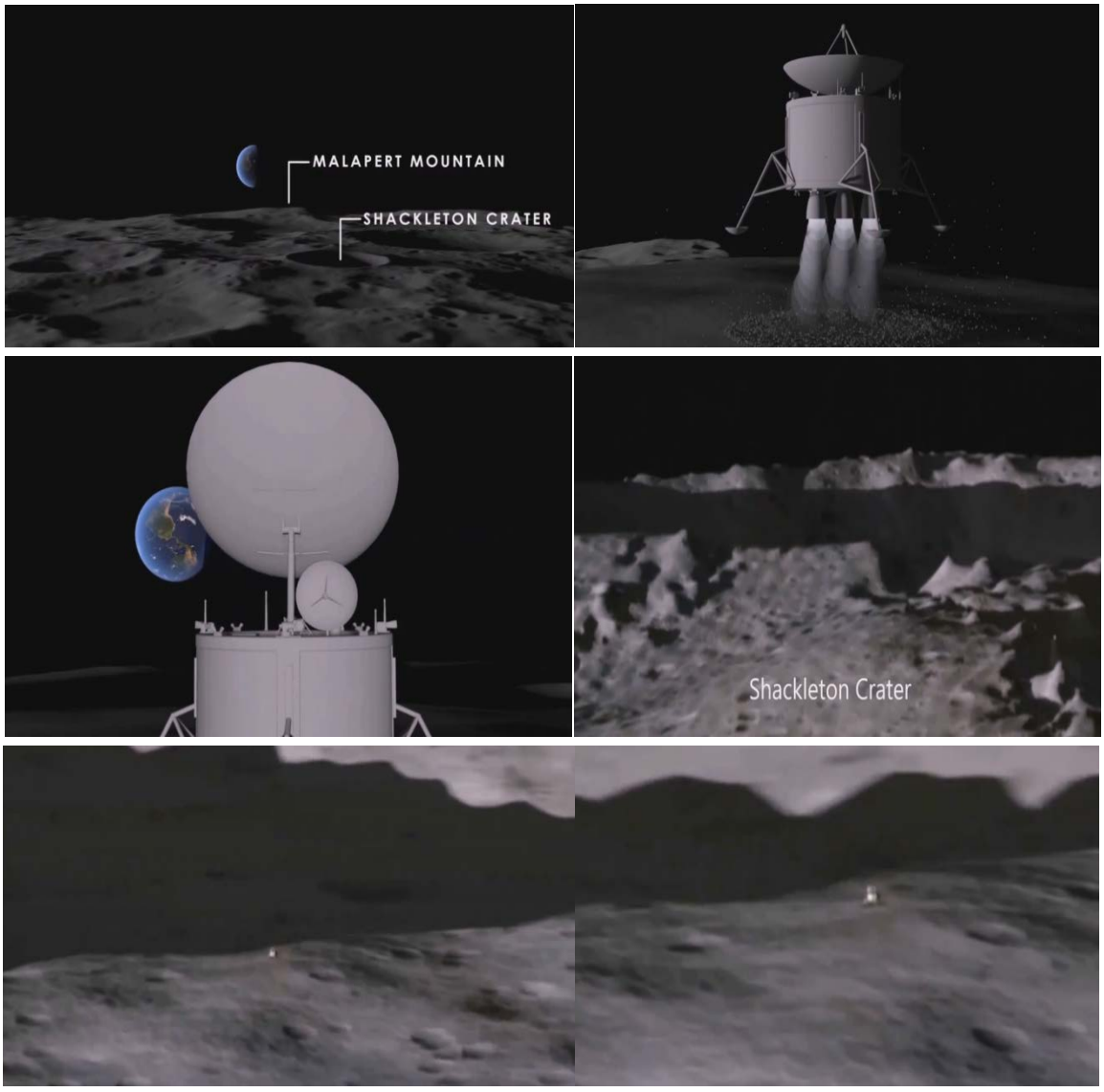

Figure 2.1. Position of Shackleton Crater and Malapert Mountain with Earth in view. Landing a communication relay on Malapert. A lander arrives near the rim of SC.

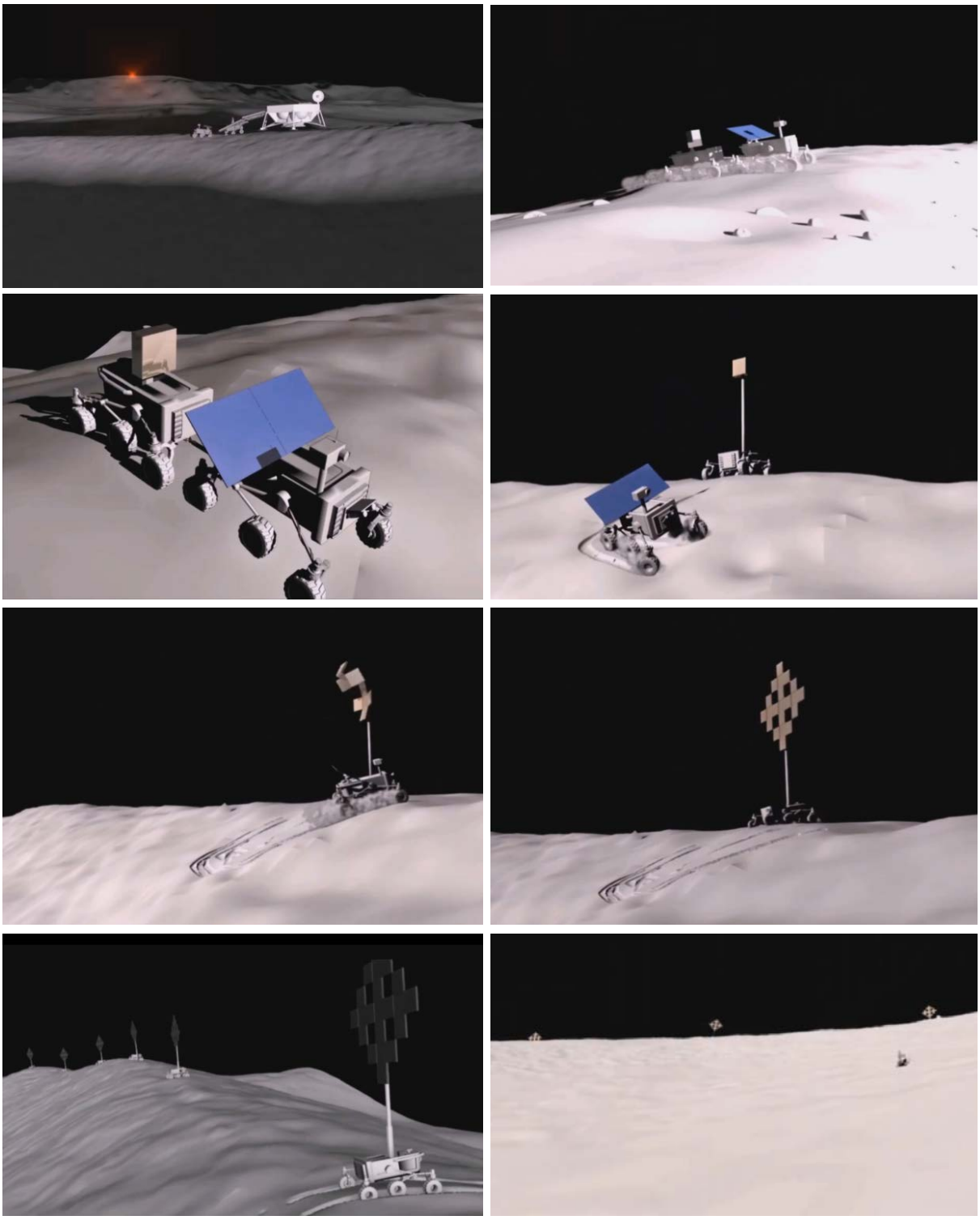

Figure 2.2. Rover gets out of the lander carrying the compactly packed TransFormer to the rim, where the TF deploys. Several TFs are positioned. Rover starts descent into crater. View of TFs aligned around the perimeter of the crater from the top of the crater looking to the side. View from the inside of the crater looking up at TFs.

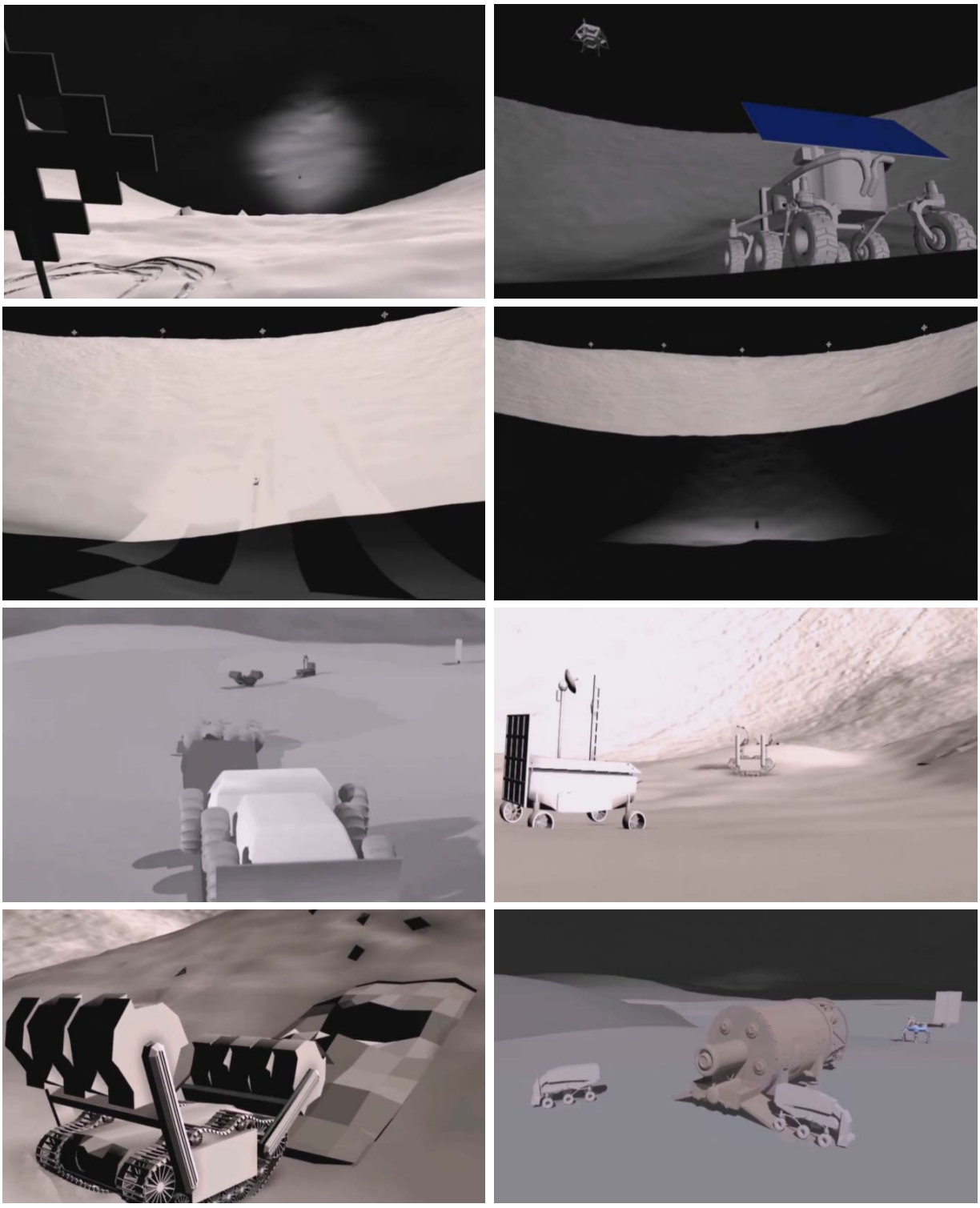

Figure 2.3. TFs illuminate the rover; rover looks up to the TFs. View from the bottom, shaded area of the crater showing reflection beams TFs illuminated rover during descent. After water reserves have been found and mapped, the ISRU equipment arrives and start operations illuminated by TFs.

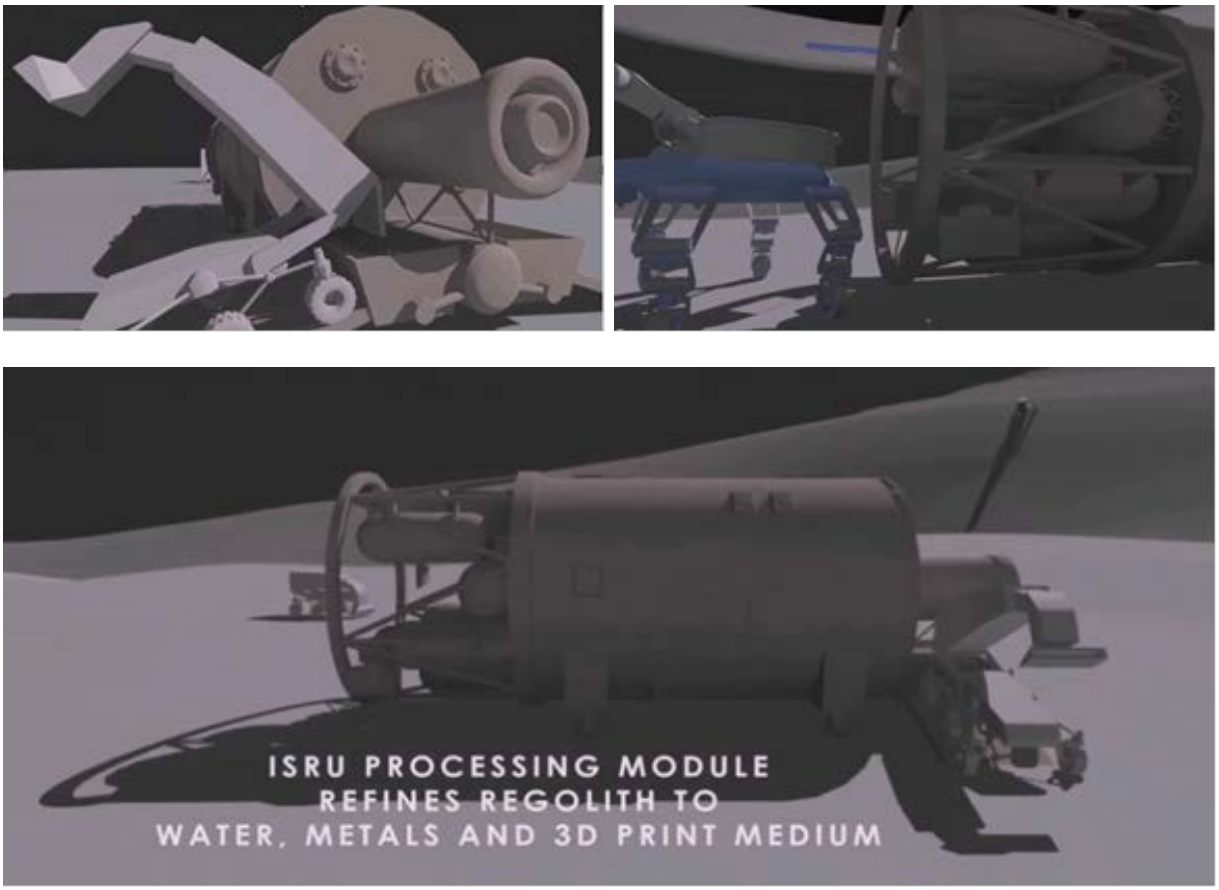

Figure 2.4. ISRU processing.

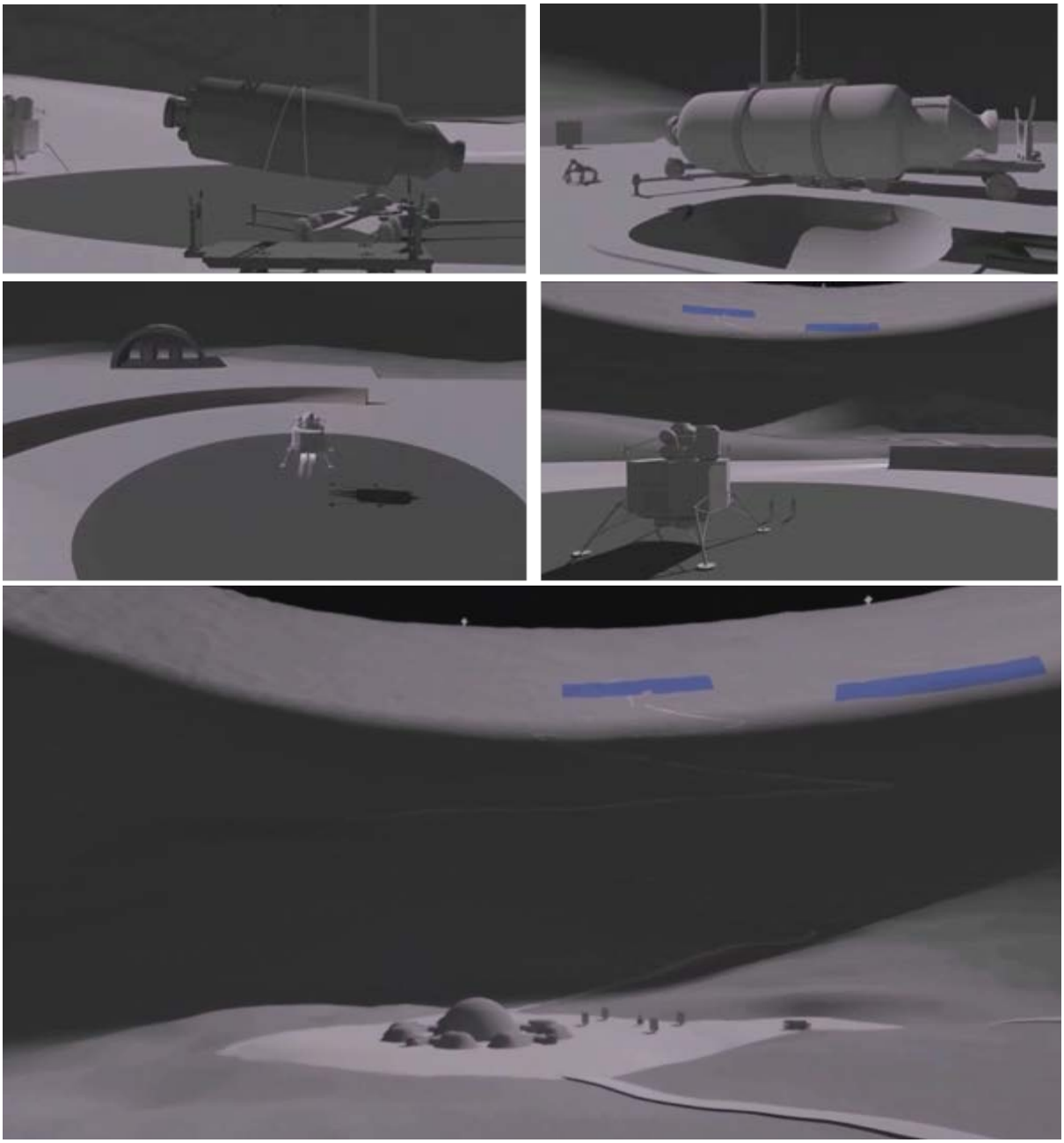

Figure 2.5. Resources and habitat are prepared for the arrival of humans. Humans arrive. An energy oasis operates inside the crater.

2.2 Rovers in Search of Water

Rover missions are needed to make in-situ measurements and map the resources. Proposed scientific objectives are to measure the distribution and abundance of water and other hydrous phases inside SC, and to understand the association of OH and water with mineral phases and landforms on the lunar surface. The rover would perform geological and mineralogical exploration, perform ice/mineral sampling and analysis, and determine subsurface structure. It would carry stereo cameras for geological analysis, and traverse, a spectrometer for ice/mineral detection. It would have a sampling arm/drill, a mass spectrometer for ice, chemical, carbon detection, an X-ray diffraction for mineralogy and a ground-penetrating radar for subsurface structure. The scientific payload would measure water ice at concentrations of 10 to ~1,000 ppm and OH and molecular water in minerals at sensitivities of 5 percent by weight. The mission would be capable of detecting water in the subsurface to a depth of 2 m. We analyze the power needs for three rover classes, the Resource Prospector rover, a lunar version of the Mars Science Laboratory (MSL) and an ATHLETE.

2.2.1 *Resource Prospector*

The objectives of the Resource Prospector (RP) rover mission are to characterize the nature and distribution of water/volatiles in lunar polar subsurface materials and to demonstrate ISRU processing of lunar regolith (**Figure 2.6**). The mission life is 6–14 Earth days (extended missions being studied) so the rover is to operate in lunar daytime. The rover mass, including payload, is 300 kg. The rover dimensions are 1.4 m × 1.4 m × 2 m; the nominal rover power being 300 W. The RP is to launch in 2021. It would be teleoperated from Earth with 10–30 sec DTE latency (light travel time and DSN catalog network latency). In principle, it could be powered as is from a TransFormer, though larger solar panels may be needed if the rover goes beyond a few hundred of meters away in the crater; yet, this should not be a complex design change.

Figure 2.6. Illustration of Resource Prospector rover. The rover probes and analyzes soil, searching for water. Unfortunately, it is designed for operation in lunar daytime (under solar illumination) only. (Credit: NASA)

2.2.2 *Solar-powered MSL-class Rover*

The MSL-class solar-powered rover for Alternative 2 (MSL 2006; NASA 2006) was designed to use a solar array as the source of electrical power for its engineering subsystems and science payload (JPL 2006). The solar array would attach to the back section of the rover and folded for stowage inside the entry vehicle (**Figure 2.7**). The array would be deployed after the rover has landed on the surface of Mars (**Figure 2.7**).

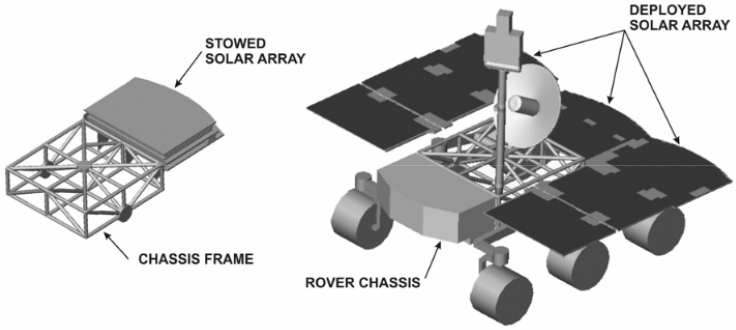

Figure 2.7. Illustration of a representative solar-powered Alternative 2 MSL rover.

The solar array would be deployed into seven separate panels surrounding the rover on three sides and would be in a fixed position parallel with the upper surface of the rover chassis. The deployed array would have a surface area of approximately **6 m^2**. The array would consist of the same type of multijunction solar cells used on the MER. The mass of the rover is ~1,000 kg, and it uses **~300 W power.**

2.2.3 *ATHLETE*

The ATHLETE rover is a component part of the reference lunar architecture. It is a multifunctional rover, which can perform a wide variety of operations including transport, repair, etc. The power consumption of ATHLETE peaks at **500 W** when the rover moves at 360 m/hr. Distance travelled during day: 200 meters; ATHLETE could perform both roles on the rim (Rim ATHLETE), such as installation and servicing of TFs, as well as roles related to ISRU and general transportation and servicing operations inside the crater (Floor ATHLETE).

The size of the solar arrays for the Rim ATHLETE would be 3 m^2. The Floor ATHLETE when at 10 km from a TF receives ~1/4th of the solar intensity through reflection. Its panels need to be a minimum 4 times larger, thus, 12 m^2; an additional reserve panel of 3 m^2 is considered; **Figure 2.8** shows the rover as built, and a design with 15 m^2 solar array.

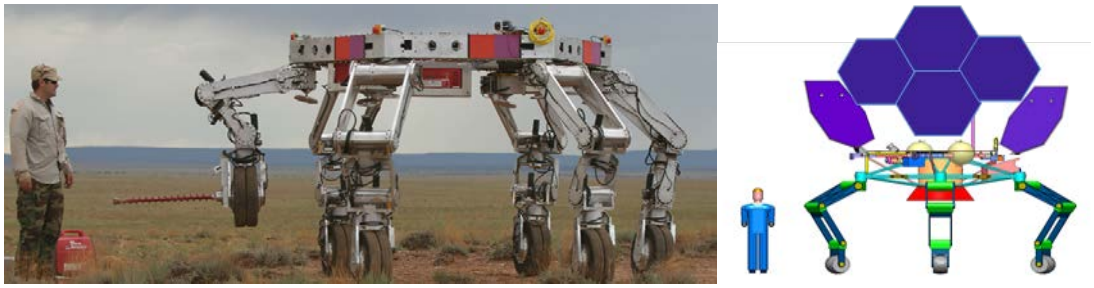

Figure 2.8. ATHLETE rover as built and version with solar panels.

2.3 Mining and ISRU – Mission Concept

2.3.1 *ISRU General Scenario*

This scenario addresses operations inside SC, and focuses on ISRU operations in a contained illuminated oasis. The goal of NASA's ISRU program is to enable future space pioneering by significantly reducing the financial cost of long-duration human missions. ISRU will accomplish this by producing consumable commodities (like water, oxygen, and hydrogen), spare parts, and structures (like radiation protection shielding, habitats, and landing pads) through the utilization of local planetary resources rather than transporting such items and materials out of Earth's deep gravity well. Typical ISRU operations include the chemical extraction of oxygen from mineral oxides found in planetary regolith, the separation of water from icy regolith by various heating methods, and additive construction using basalt found in regolith. ISRU also depends upon technologies involved with prospecting for local resources and especially for mining granular planetary regolith. This study focuses solely on ISRU for water processing. Water ice may exist in the form of icy regolith where it may be bound to regolith particles to form extremely hardened icy regolith. Excavating dry or icy regolith using large excavators and/or a swarm of small excavators on long-duration missions will be so energy intensive that it will require excavator systems to either carry large onboard power generation systems or batteries that can be recharged at a dedicated power generator station.

TFs will enable long-duration ISRU operations providing power, heat, and illumination to operate at otherwise low temperatures and in dark areas. In the long term, ISRU processing plants will also require considerable power to operate mechanical systems to convey regolith between the exterior vacuum environment and the partial atmosphere inside the reactors, and to transfer the regolith between various compartments within the reactors. The reactors will also need electrical power to heat cold regolith to an elevated temperature before it can be processed effectively; though the TF could provide at least in part the needed thermal energy.

Depending on the ISRU process, elevated temperature would be ~1,000°C for chemical reactions that extract oxygen from mineral oxides, or 300–400°C to evolve water from hydrated minerals by thermal heating. A batch size of 100 kg of regolith might have to be processed each time.

TFs would project sunlight to dedicated areas (see **Figure 2.9**). TFs would provide electrical power and direct lighting and thermal energy to enable ISRU processing reactors to pre-heat cold regolith and keep electronics above their minimum operating temperature. The area can be illuminated in zones, or intermittently, as needed.

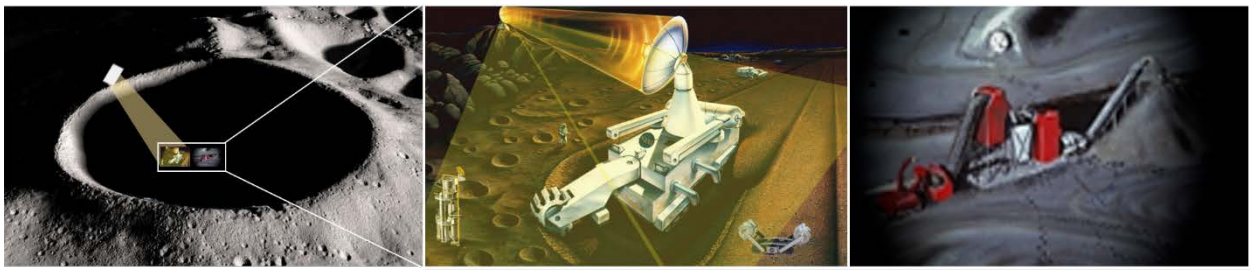

Figure 2.9. Illustration of lunar ISRU operations in oasis and excavations in the dark.

ISRU operations can be separated in phases with distinct power needs, such as a) the extraction of water, b) electrolysis to separate H and O, c) refrigeration to bring H to lower

temperatures, d) transportation between extraction site and collection site, and possibly to and from a maintenance site, if, for example, they need to get batteries recharged, warmed up, etc.

Assuming an architecture where a mass driver could be used to launch water to a propellant processing station at Earth-Moon L2 solar power needs are also determined. A figure of merit in W*h/kg or kW*h/t can be used to asses different approaches.

A section on ice sublimation is presented next, followed by three sections oriented on ISRU and associated power needs. The calculations come from different extraction methods. While some of the assumptions vary, the conversion or scaling to the same target parameters is direct.

2.3.2 *Ice Sublimation Analysis*

Vasavada et al. (1999) show that it takes on the order of 15 min to heat a high thermal inertia surface from 100–170 K by direct solar input (1362 Wm^2). In a different study, modeling by Andreas (2007) indicates that a 100-micron radius ice particle heated to 170 K would only lose about 10% of its original mass in an hour. The temperature on the floor of Shackleton is ~40 K. **Figure 2.10** shows the ice sublimation rate as a function of temperature (Andreas 2007). The left axis gives the sublimation rate as a mass flux; its units are μg $cm^{-2}h^{-1}$. The right axis gives the sublimation rate as the number of molecules of water vapor leaving a square centimeter of the ice surface per hour at about 70 K. Note that ice deposits on the Moon might be dirty—for example, mixed with regolith dust, carbon dioxide, or some other contaminant (Nozette et al. 2001). Any such contaminants will lower the saturation vapor pressure of the ice and, consequently, slow its sublimation rate. The fraction of initial mass (m_0) remaining after time t when spherical samples of pure water ice with initial radii (r_0) of 100 μm is also shown in **Figure 2.10**. Initial calculations predict that a spherical lunar ice deposit of initial radius 1 μm would lose 10% of its initial mass in only 32 s if it were heated to 170 K. A 100-μm-radius deposit, however, would require about an hour to lose 10% of its mass by sublimation if it were heated to 170 K. Larger samples suffer even smaller rates of fractional mass loss.

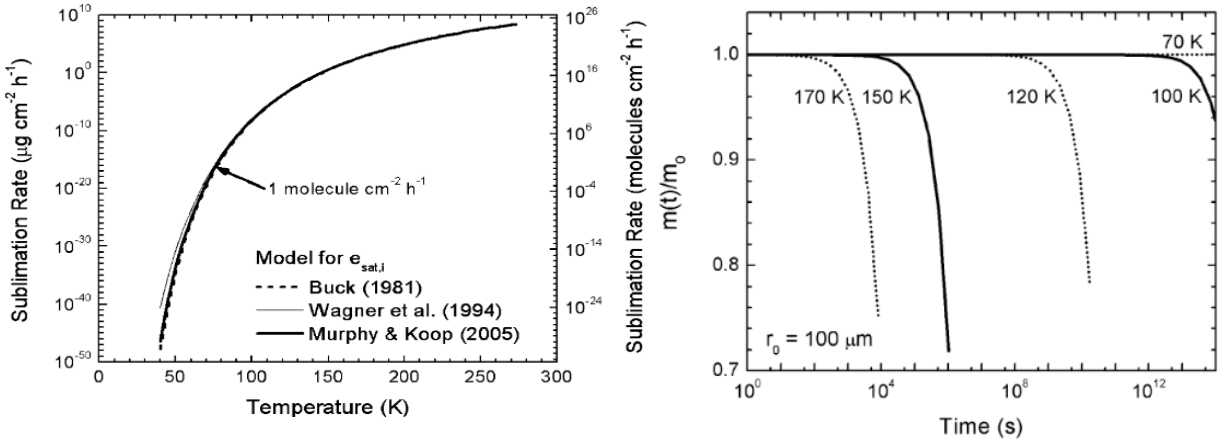

Figure 2.10. Ice sublimation rate vs. temperature, from http://www.nwra.com/resumes/andreas/publications/Icarus_Moon.pdf. Mass of ice as function of time (Andreas 2007).

Based on this this summary evaluation (there are many papers yet not enough ground information available for a good understanding of the nature of the ice in the craters) and the fact that the level of solar illumination targeted by TFs is smaller (a reduction of about 4 times compared to direct solar exposure), this would not have a significant impact over durations of

minutes to tens of minutes, if subjected to accidental illumination around the rover. This would not cause loss of the deposits, as the rover will be in an area just long enough to use the much higher concentrated power to extract the resources. On the other hand, concentrated illumination and increased temperatures will clearly result in sublimation, which is exactly what the ISRU techniques are aiming for.

2.3.3 *ISRU using KSC Zero Energy Direct Sublimation*

This section is based on KSC work (Co-I James Mantovani). An ISRU system model diagram demonstrating phases of ISRU system with regolith-water processing is shown in **Figure 2.11**.

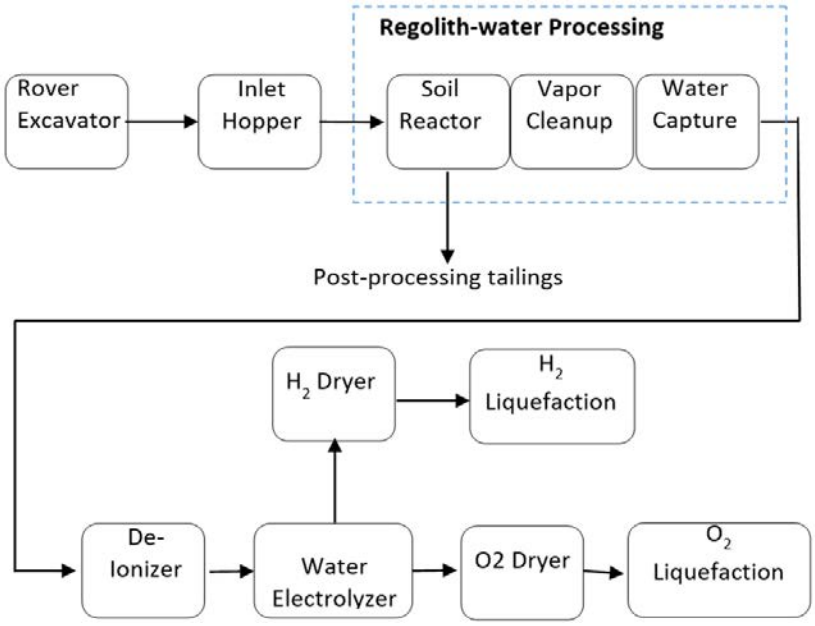

Figure 2.11. ISRU system model diagram demonstrating phases of ISRU system with regolith-water processing.

A regolith excavator designed and developed at NASA KSC called RASSOR is baselined to excavate the regolith, transport the regolith to a processing plant where the water and regolith will be separated, and then move the dehydrated regolith to a remote location.

Figure 2.12. KSC excavator RASSOR II, which is the current baseline for the case study. This technique enables the harvesting of large amounts of regolith on a low gravity body with a very low-mass vehicle.

RASSOR II (**Figure 2.12**) provides a low mass robotic vehicle (60 kg) that enables low reaction force mining of regolith and volatile ice in a reduced gravity environment. It allows surface excavation, deep trenching, dust tolerance and recovery from anomalous tumbling events through the use of acrobatic maneuvers to self-right itself. It has bucket drums that hold up to 80 kg of excavated regolith. This requires the development of an autonomous control system that uses stereovision and localized torque feedback from custom high torque harmonic drive lightweight rotary actuators.

The Zero Energy Direct Sublimation Device is described in NASA NTR #1506712978, Patent Pending.[1] It performs calculations for 100 kg of water per day.

The phase diagram for various phases of water is shown in **Figure 2.13**. The pressure of ice is on the vertical axis and temperature on the horizontal axis. The power calculations were based on a sublimation temperature of 200 K that was derived from this phase diagram.

The ISRU operates with production rate drivers of 0.1 t/day, 1 t/day, 10 t/day of water needed. ISRU production will last for 480 days of operations, 24 hours a day. The ISRU system only includes mass/power for cryo-coolers needed to liquefy. The storage of cryo liquids is not included in the current version of the model. Additional energy is required for storage.

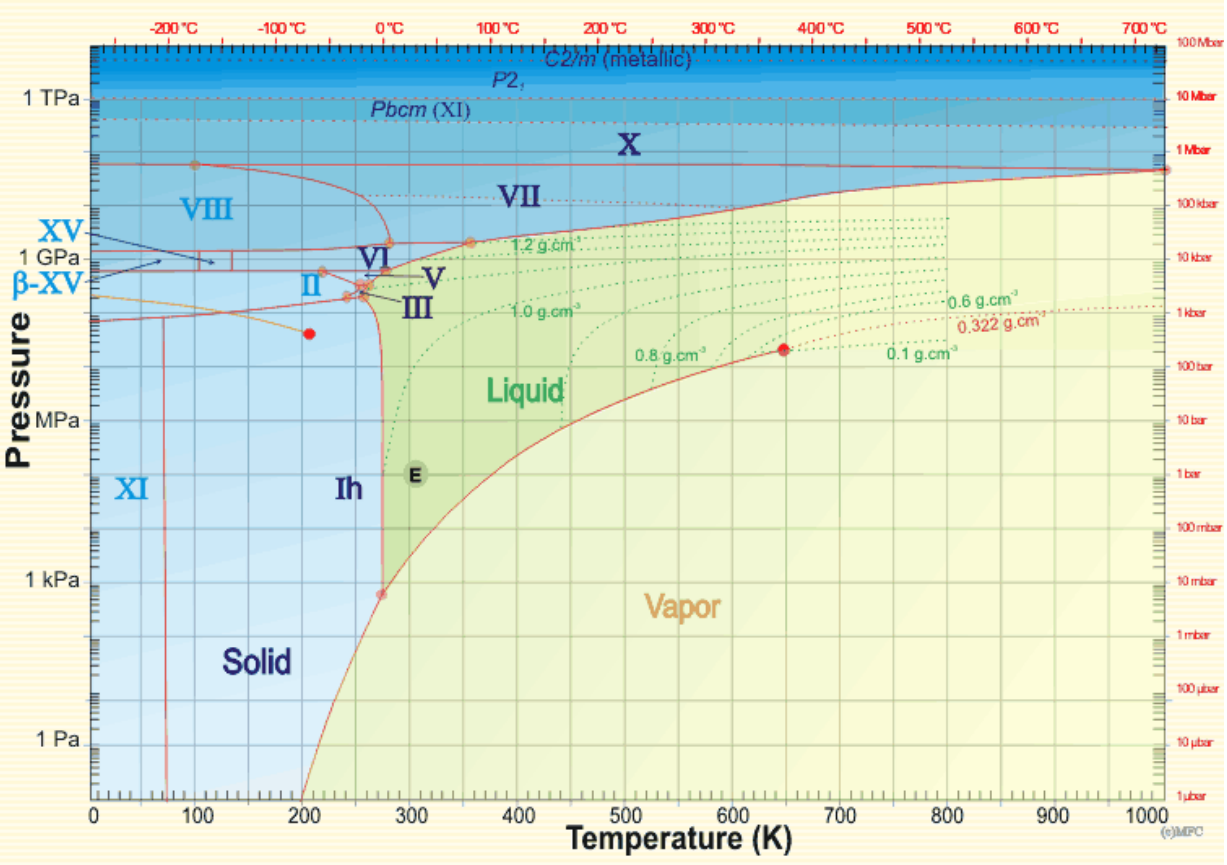

Figure 2.13. The vapor pressure of water ice as related to temperature http://www1.lsbu.ac.uk/water/water_phase_diagram.html

[1] Note: The Zero Energy Direct Sublimation Device is discussed in the NASA NTR #1506712978 "Utilization of Solar Energy for Direct Sublimation" and is proprietary to NASA in-house audiences only as a patent is being pursued for this technology.

The graph in **Figure 2.14** shows the minimum thermal power required to sublimate 100 kg of water in icy lunar regolith as a function of water concentration in icy lunar regolith. The thermal power required approaches a limiting value of 4 kW as the percentage of water in the icy regolith approaches 100%, while the thermal power required to sublimate water contained in very dry icy lunar regolith at 1% is **16 kW** (this corresponds to 13.8 kJ/g). The results shown in the thermal power graph are found to scale with the desired mass of water that is targeted to be extracted each day. If the targeted mass increases to 1,000 kg (a factor of 10), the power required to sublimate the water from the regolith will also increase by a factor of 10. Compared to the 4 kW needed to sublimate 100 kg of highly concentrated water in icy lunar regolith, sublimating 1,000 kg of water requires 40 kW, and that 10,000 kg of water ice requires 0.4 MW power, continually applied over a 24-hour operational day.

The power requirements for the RASSOR excavator and the water extraction system were calculated for a targeted daily collection of 100 kg of water during a 24-hour operational day. The results of these calculations are shown in **Figure 2.14**. If the icy regolith water content is 100%, then there is no need to sublimate the water. In this case, RASSOR would excavate the water ice directly and only require a solar collector diameter of 4.1 meters to recharge its batteries over a 2-hour recharge time per 8-hour operational time.

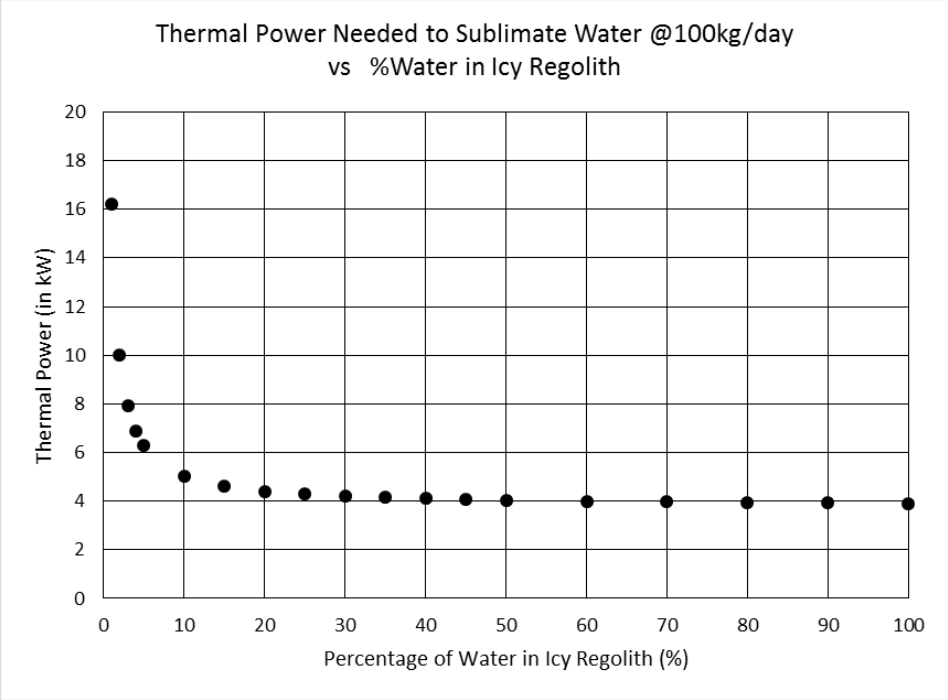

Figure 2.14. Continuous power required to sublimate 100 kg of water ice per 24 hours at different water ice–to–regolith ratios.

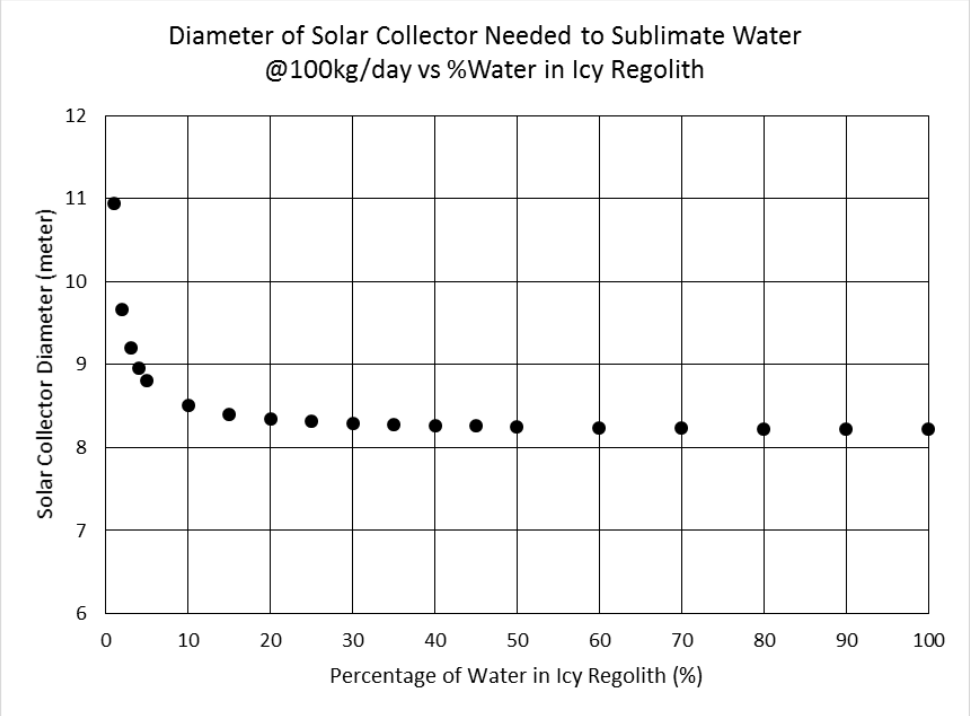

Figure 2.15. The diameter of the solar concentrator needed to sublimate water at 100 kg per 24 hours.

Water will be extracted from the icy regolith using a process called direct sublimation with the KSC-developed Zero Energy Direct Sublimation Device. The Zero Energy Direct Sublimation Device will use the TransFormers reflector in SC to concentrate solar energy transmitted into the shadowed crater as power to then direct the solar power to sublimate the icy regolith causing the water vapor to recondense onto a cold plate. The water ice would then be autonomously removed from the cold plate and stacked as ice sheets for storage until the clean water ice is needed for its intended purpose.

To summarize, based on the KSC model, for a 10% water in the regolith, 100 kg a day, the thermal power would be ~5.5 kW (@ 4.7 kJ/g) over 24 hours, i.e., **132 kWh**.

As a later analysis refers to **10 t of water per day**, the scaled number from here would be ~0.55 MW, or, rounded as **0.6 MW** as a baseline value (this is thermal energy).

A solar concentrator) of about 8.5 m diameter is assumed, for incident solar illumination of 1.3 kW/m^2 (on the illuminated area, e.g. on the rim). The total power received is 1.3 kW/m^2 × 56.7 m^2 = **73 kW.** If concentrator is in the crater, the solar illumination received depends on the distance from reflectors. As shown before, at 10 km away from a 40-m diameter reflector, the solar illumination drops by a factor of 4. (~300 W). This means the area of the concentrator needs to be 4 times larger for capturing the same power as a solar concentrator on the rim reflector on the rim. That is twice the radius, hence a 17-m diameter concentrator is needed.

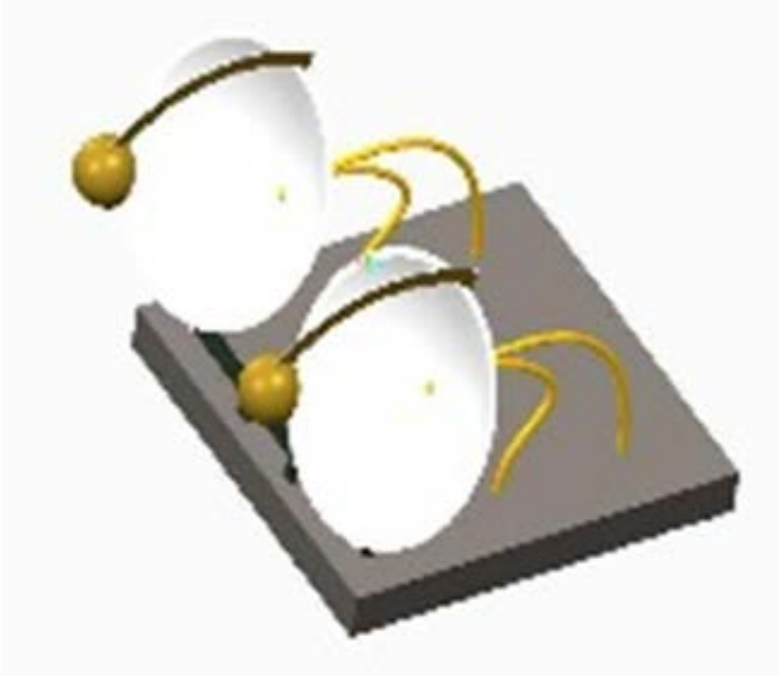

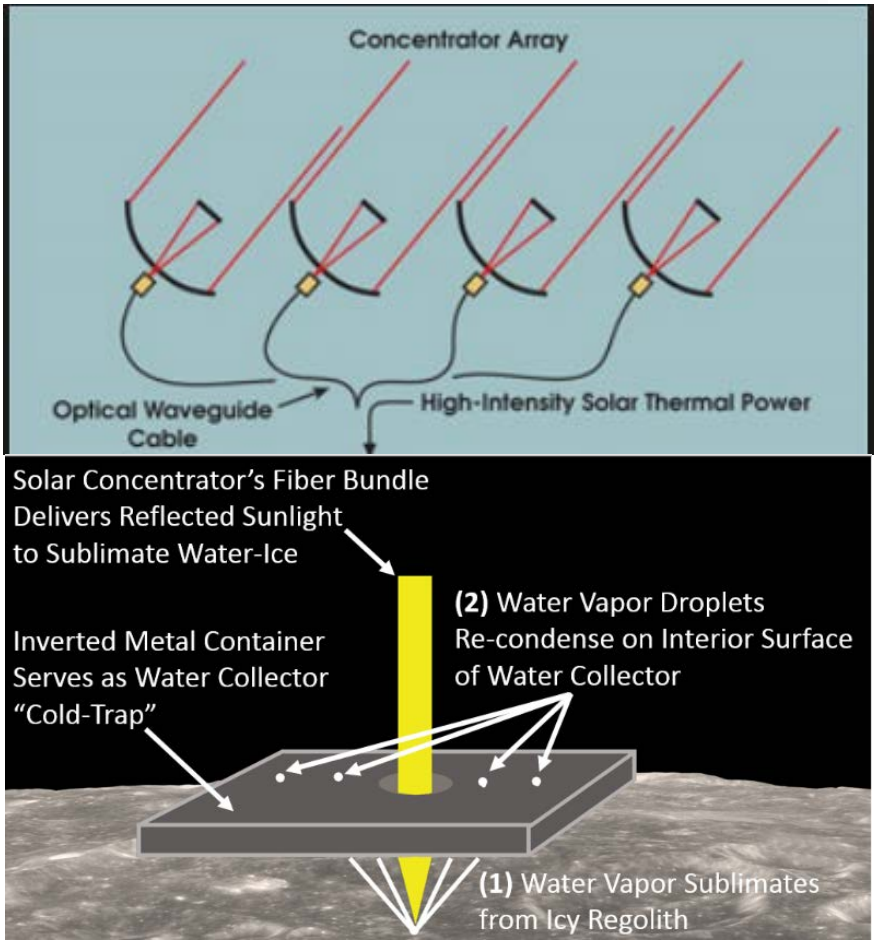

Figure 2.16. The Zero Energy Direct Sublimation Device. Concentrator array with optical waveguide cables.

2.3.4 *ISRU using TransAstra Radiant Gas Dynamic*

This section is adapted after (Sercel 2017).

This section determines the power required for extraction of 1,000 metric tons per year of trapped water from permafrost based on the use of a TransAstra corporation patent-pending process called Radiant Gas Dynamic (RGD) mining and associated patent-pending rover design. RGD mining is an approach in which radiant energy is used to sublimate ice without excavation coupled with water collection in vacuum traps.

The RGD extraction approach eliminates the need for standard mechanical excavation equipment. The rover/excavators are envisioned to mass 5,000 kg each and have a 5-m-diameter capture dome. For the purposes of this architecture, five rovers have been assumed. **Figure 2.17** and **Figure 2.18** illustrate some of the key elements of the rover architecture and the RGD mining approach, respectively.

Assume a ratio of 10% water and 90% regolith, with 1,850 kg/m^3 (a conservative estimate of regolith average density down to 1 m) (http://web.utk.edu/~alshibli/research/LR/lr.php for regolith density). Then 1 m^3 volume would contain 0.9 m^3*1,850 kg/m^3, 1,665 kg regolith and 0.1 m^3*1000 g/m^3 =100 kg water.

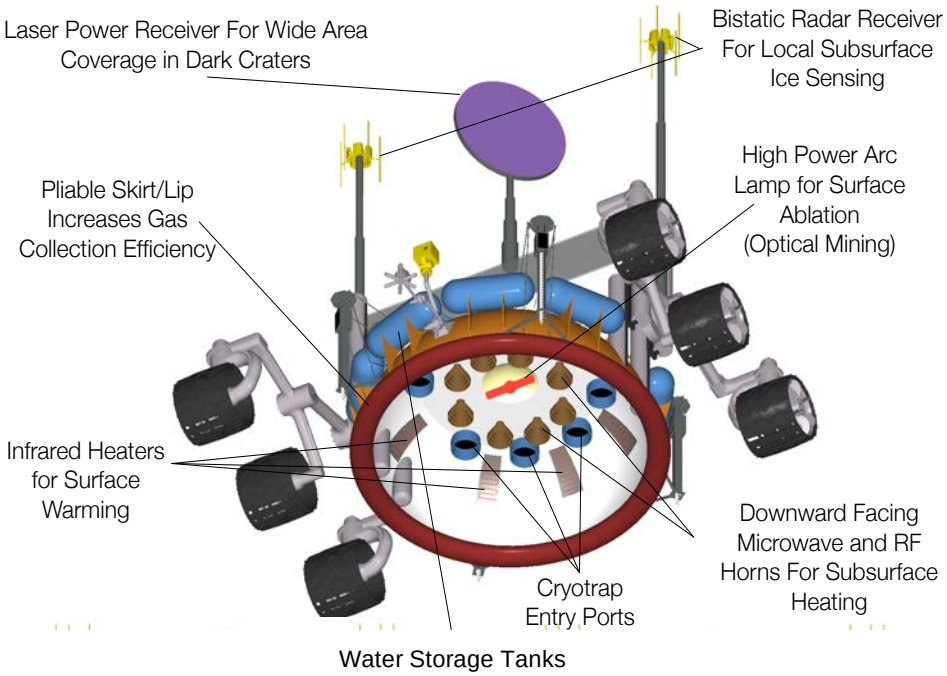

Figure 2.17. RGD rover concept schematic, Patent Pending, TransAstra Corporation.

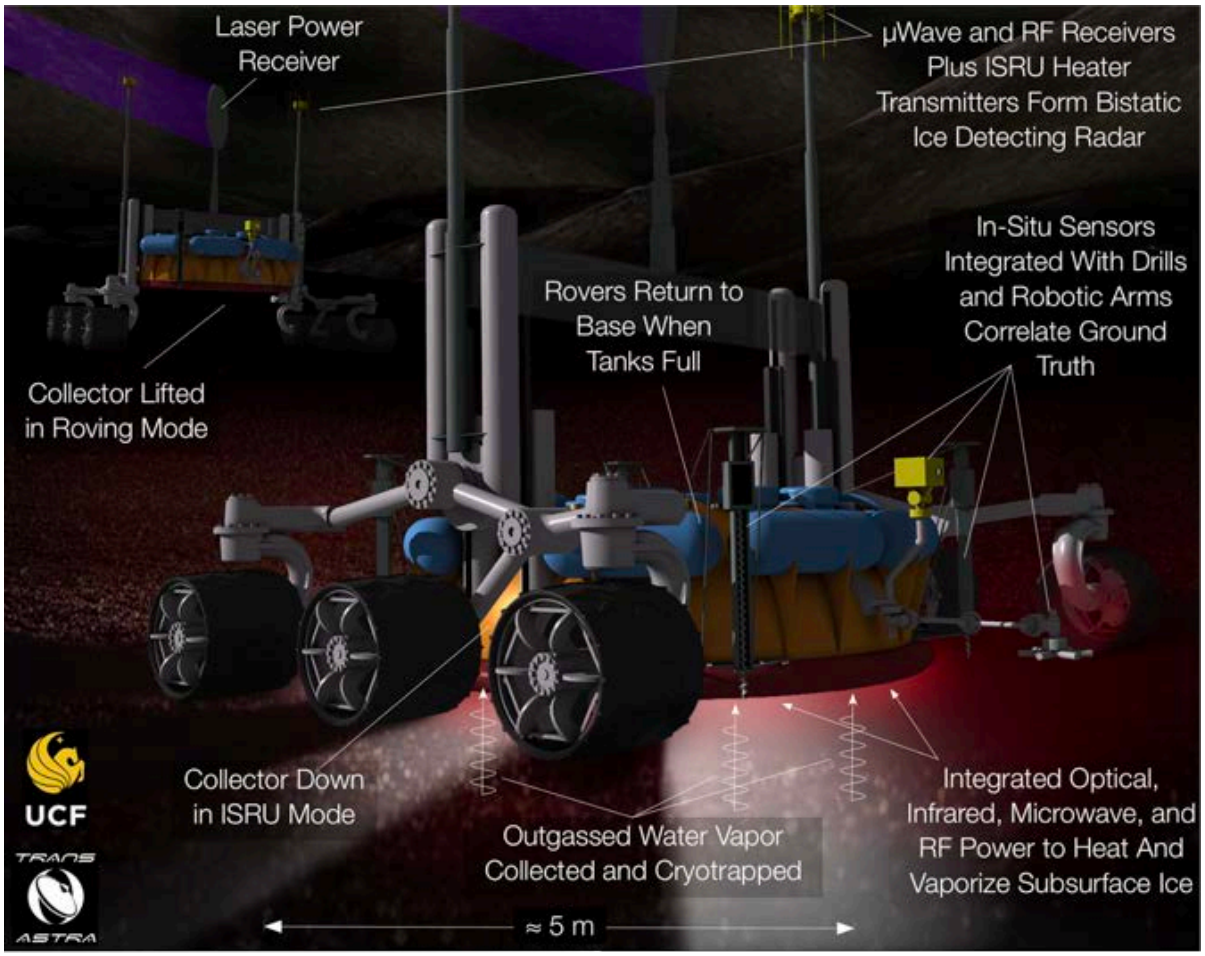

Figure 2.18. RGD rover operations concept, TransAstra Corporation.

Assuming *a circular excavation zone of 0.5 km radius* from a collection node (which could coincide with the transportation node, if a launch system does not impact environment over wide area) the excavated volume to 1 m depth amounts to $3.14*(500)^2*1 = 3.14*250{,}000\ m^3 = 780{,}500\ m^3$, in which, at 10%, would be *78,500 t of water*. Note that at 1,000 t per year this would last 78 years at the determined needed rate. Even only a fraction of this volume being accessible would still mean operations for a number of years. For example, if only ~25% of the area is actually accessible by the rovers, there is still almost 20 years' worth with the 0.5-km radius zone. It seems reasonable to assume that over the lifetime of this scenario, the average rover round-trip will be 1 km or less, making it a reasonably conservative estimate.

Given a 2.5-m radius collection system, this means $(3.14*2.5^2)*1 \sim 19.63$ kg of water can be obtained in a single rover extraction operation. Between the five rovers, this means 100 kg water over an extraction period.

The total number of trips can now be calculated as 510 (rounding up) or 102 trips per rover per year. Having each rover go out and back on a ~3-day cycle seems very reasonable, given the round trip traverse is estimated at 1 km. This only requires the rovers to travel at a speed of ~20 meters per hour and still have almost 24 hours to perform the extraction operations during each cycle.

Table 2.1. Energy consumption annually for RDS rover round-trips.

Value	Units	Comment
0.60	Whr/m*t	Using value based on Curiosity mobility
5	t	Rover Mass
3.00	Whr/m	Traverse energy use
1000	m	Average traverse during first 20 years (conservative)
3,000	Whr	per trip
3	KWhr	per trip
1530	KWhr	per year for traverses for all 5 rovers

Table 2.1 provides the key parameters for the energy calculation estimates in the context of extraction by RDS technology. Assuming the starting temperature is ~35 K, it is then necessary to raise the temperature ~240 K, as well as accounting for the heat necessary to melt and vaporize the water near its triple point. **Table 2.1** provides a breakdown of the calculations to determine the amount of energy required by a rover to extract 100 kg of water, based on **Table 2.3** and the additional assumption that the RGD system is only 30% efficient in converting power to radiant energy.

Table 2.2. Some important physical characteristics.

Parameter	Value	Units
Water Triple point	273.16	K
Heat of fusion of water	334	J/g
Heat of vaporization of water	2257	J/g
Specific heat of ice	2.09	J/g·°C
Specific heat of water	4.18	J/g·°C
Specific heat of steam	2.09	J/g·°C
Specific heat of regolith (average)*	0.6	J/g·°C

(*) Regolith specific heat varies with temperature – conservative average value used based on (Ritcher, 1993).

Table 2.3. Calculations for energy required by Rover to extract 100 kg of water.

Value	Units	Comment
3,092.6	J/g	Energy to raise water 240K
3,092,600	J/kg	Converting to J/kg
859.06	Whr/kg	1 Whr = 3600 J
85,906	Whr	Energy for 100 kg water*
286,352	Whr	30% efficiency penalty
144	J/g	Energy to raise regolith 240K
40.00	Whr/kg	Converting to Whr/kg
66,600	Whr	Energy for 1665 kg regolith
222,000	Whr	Efficiency reduction applied
508,352	Whr	TOTAL energy required by RGD rover to extract 100 kg of water from 1 m^3 of lunar regolith
508.4	KWhr	- or in KWhr

** The energy for obtaining 100 kg of water is of the same order of magnitude as KSC but the overall (which includes heating the regolith) factors of efficiency penalty are considered*

Table 2.4 shows the rather modest requirements for power for transfer of the water for storage and launch. It turns out to be almost negligible compared to the extraction energy required, and use of gravity or vacuum that is freely available will likely make it even less power intensive than shown.

Table 2.4. Energy required to transfer water for storage/launch

Value	Units	Comment
9.81	MJ/1000 t	To pump vertically 6 m on the lunar surface (1/6th Earth gravity)*
3.60	KWhr/MJ	Conversion factor
2.73	KWhr	To pump water per year
18.17	KWhr/year	Assume same efficiency for power transmission

(*)Online resource (CottonInfo, 2015).

We scale the result to evaluate the power needed for producing 10 t of water per day. From the 508.4 kWhr for 100 kg water, for a need of 3,650 t per year one would require, with similar water extraction technology, 3,650×100 times more energy, thus, 185,566 MWhr for the year, which is equivalent to ***a power of 0.58 MW, rounding to 0.6 MW prior estimate.*** This is in agreement with estimates from Schnitzler et al. (1997) and Larson et al. (1999), and the analysis in Zuppero (2005).

The RGD operation scenario has performed an analysis for the case in which power is transmitted to the RGD rover by laser. In this case, assuming the laser is 50% efficient based on current technology (G. Overton 2013; Koenning 2008) and the receiver is 30% efficient (allowing for spill and tracking errors, along with power conversion and management losses), for a total power transmission efficiency of 15%, the annual energy requirements can be calculated and are summarized in **Table 2.5**. The rover extraction process is clearly the dominant energy consumption, at more than 300× the energy used for traverse. The pump energy from **Table 2-4** is clearly negligible.

Table 2.5. Summary of results.

Value	Units	Comments
33,937	MWhr	Extraction Energy per year
10	MWhr	Travel Energy per year
33,947	MWhr	Total Rover Energy usage per year
6,433	MWhr	Launch Energy usage per year (discussed in 2.3)
40,381	MWhr	Total Energy usage per year
40	MWhr/t	Energy per metric ton of ice extracted
4.61	MW	Average solar array output required (solar array on the rim converting energy to laser for beaming)

This extraction approach and scenario requires ~4 MW captured by photovoltaic solar array on the rim, converting to laser (approx. 4,000 m^2) if one considers losses due to angle of incidence.

2.3.5 *An Architecture for Human Exploration of Mars Using Lunar Propellant*

This section is adapted after (Wilcox 2017), and is presented in more detail in Appendix A.

A transportation architecture for cislunar space that enabled by ISRU propellant has been previously proposed (Spudis 2010; Lavoie 2016). Here we consider how a lunar ISRU infrastructure might be used to enable a sustainable and affordable transportation architecture for humans to explore Mars, as an example of one attractive application for such an infrastructure.

We assume an ISRU water/propellant capability exists in a lunar polar crater, which can deliver *10 metric tons (t) of propellant-grade water per day*, and, in the cold and darkness of the lunar polar crater, is able to convert it into LH_2/LO_2 propellant at a common O_2:H_2 mass ratio of 6:1 as used in rocket engines (Online resource, Braeunig), that is 7.5 t/day of LH_2/LO_2.

We take as the central premise for this work that this 7.5 t/day of LH_2/LO_2 propellant is to be used to enable sustainable and affordable human exploration of Mars by launching one human exploration mission from Earth to Mars on each minimum-energy Hohmann transfer opportunity (every 26 months). Further, each such mission is to have as many reusable components as possible, and as few expendable components. It would take advantage of the high-thrust character of LH_2/LO_2, allowing "Oberth Maneuvers" deep in the gravity wells of Earth, Moon, and Mars wherever possible (online resource, Wikipedia).

The architecture involves a concept for a standardized "self-propelled tank" having an 85% propellant mass fraction that could hold up to 51 t of LH_2/LO_2 propellant. A variant of this tank would be equipped with landing legs so that, when fully loaded, it could lift another full tank into low lunar orbit (LLO), release it, and have enough propellant remaining to mate with an empty tank and to land safely back at the ISRU plant in a lunar polar crater. Two such pairs would be launched each lunar sidereal month such that the two payload tanks could mate together in LLO and depart to a carefully selected high Earth orbit (HEO). This orbit is such that exactly one tank would be consumed propelling one full tank to HEO and returning one empty tank from HEO to LLO, with both tanks arriving empty. Also, a low Earth orbit (LEO) is selected where two full tanks in HEO could mate together such that one full tank arrives in LEO while the other tank has just enough propellant left to return to HEO, arriving empty. This combination of capabilities allows payloads to be launched from Earth into LEO, where they could be ferried to HEO using lunar propellant. Such payloads could be assembled together as stacks in HEO, where an array of full tanks accumulated over time from lunar ISRU could propel them on Hohmann transfers to Mars on every opportunity (every 26 months).

The notional payload we envision launching to Mars every 26 months includes two 31 t Deep Space Habitats (DSHs; one for the outbound journey and one for the return journey) plus a 48 t Mars Surface Habitat with Ascent Vehicle (MSHAV). The stack departs HEO with a small burn from the array of 24 standardized propellant tanks—just enough to put it on an Oberth Maneuver trajectory, swinging by the top of the Earth's atmosphere where the main Trans-Mars Injection (TMI) burn occurs, consuming 7.8 of the 24 tanks. No tanks are jettisoned, so as to make this architecture sustainable and affordable. Upon arrival at Mars ~7–9 months later, another 9.2 tanks are burned to inject the stack into low Mars orbit (LMO). Exactly one tank is burned to de-orbit the MSHAV, reducing its velocity to zero at some point deep in the Mars atmosphere. The one tank that de-orbits the Mars entry stack is lost.

After ~500 days on the Mars surface, the MAV launches and mates with the main stack in LMO. The returning DSH and the 23 tanks depart LMO with a burn of 4.3 tanks for TransEarth Injection. Upon arrival at Earth, 1.7 tanks are burned to inject into HEO, where the tanks could be shuttled back to the lunar surface for refueling. The DSH is mated with a single full tank at HEO that brings it to LEO to rendezvous with a crew capsule for reentry.

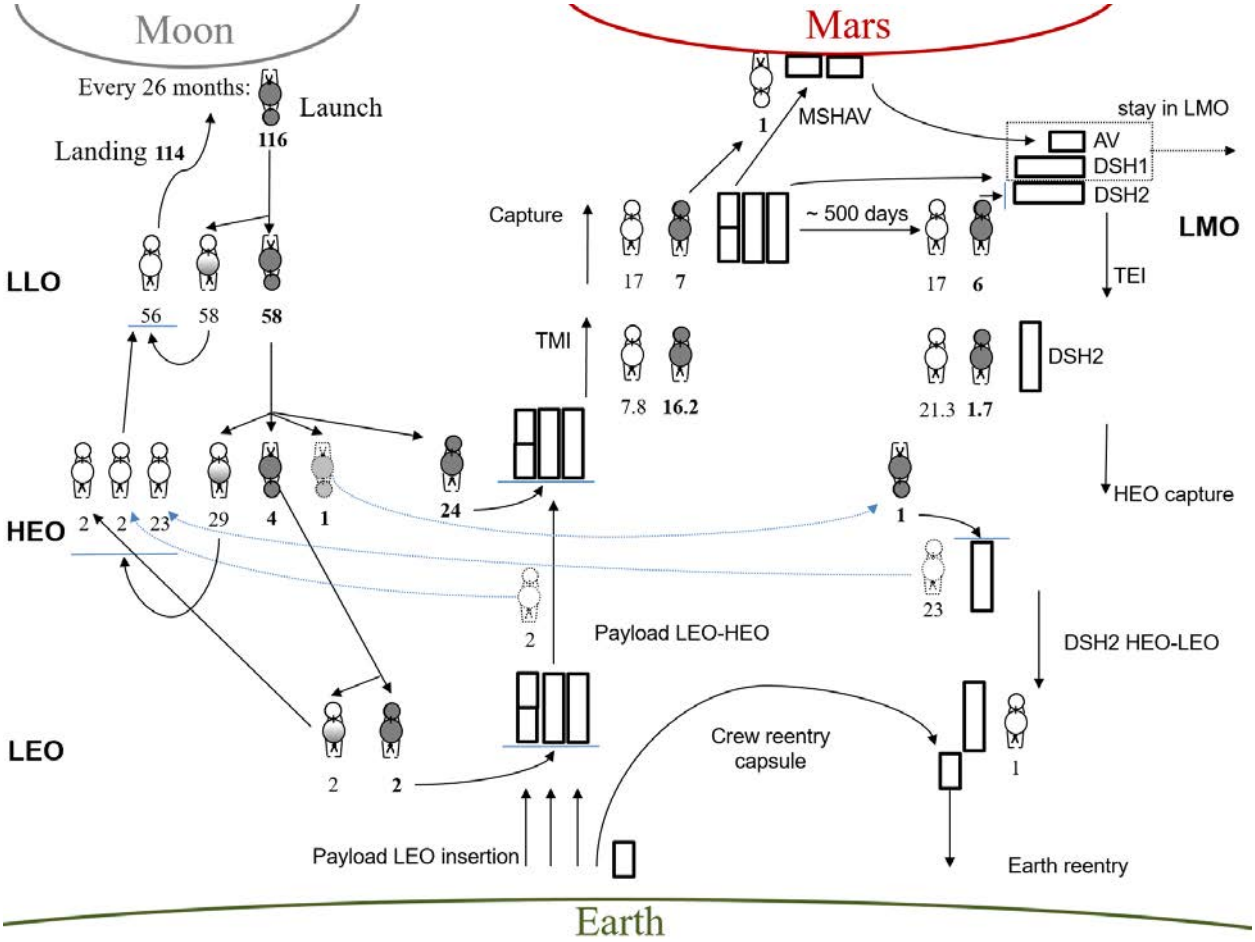

Figure 2.19. "Bat Chart" showing logistical flow with time moving from left to right and spatial relationships bottom to top. Lunar propellant production proceeds continuously on 26-month cycles, delivering 24 full tanks to HEO as needed to propel payload stack to Mars and back.

A summary of the infrastructure requirements is as follows. Two sets of 24 space-version tanks could be enroute to/from Mars at any given time, plus up to 7 full tanks stockpiled at HEO, plus at least 2 enroute to/from LLO and 4 being filled on the lunar surface, of which 2 are lander-versions. Thus, a total fleet of 2*24+7+2+4=61 tanks is needed, with one new tank being launched every 26 months to make up for the one lost in the Mars de-orbit maneuver. The architecture burns 3 tanks every 27.3 days, plus 28 tanks every 26 months (24 to push the Mars stack and 4 to lift the stack from LEO to HEO), for a total burn rate of 53 tanks/year.

The energy needs to obtain 10 t of water per day are as follows:

- The energy (thermal) for water extraction would range from 0.54 MW (at 4.7 kJ/g, for 10% water in regolith) to 1.58 MW (at 13.8 kJ/g, for 1% water in regolith).

- The separation through electrolysis (at 18 kJ/g) would require ~2 MW (electric), which would mean ~6 MW solar received from TF assuming ~33% efficiency.

Several MW are estimated to be needed for running refrigerators to liquefy hydrogen.

2.4 Electromagnetic Launches from the Moon

Figure 2.20 shows the trajectory profile that can be employed for an electromagnetic launcher (mass driver) to deliver payloads such as ice to Earth-Moon L2 from Shackleton Crater with minimal residual ΔV. The vertical axis (distance from Earth-Moon Line) is the distance from a line drawn from the center of the Earth through the center of the Moon in a coordinate system that rotates with the Moon in its trajectory around the Earth. The horizontal axis (Distance along Earth-Moon Line) is the distance along this line, in other words the distance from the launch point on the Moon to L2. This is a rather surprising and fortuitous result. Prior studies of mass driver launch from the Moon were based on horizontal launch from equatorial regions. A launch from inside Shackleton Crater may allow a mass to be delivered directly to L2 without rocket propulsion. The curve of the launched payload trajectory was generated by integrating the equations of motion and the launch angle and launch velocity were arrived at using a trial and error or "shooting" technique to minimize miss distance to the L2 target and minimize arrival velocity. Leaving the south pole of the Moon with a velocity of 2,224 m/s (just below the escape velocity of the Moon), at an elevation angle of 0.86 radians and "leading the target" by 0.53 radians allows a projectile to reach E-M L2 within 40 km after a 2.26-day coast at a velocity of 222 m/s at arrival with respect to E-M L2.

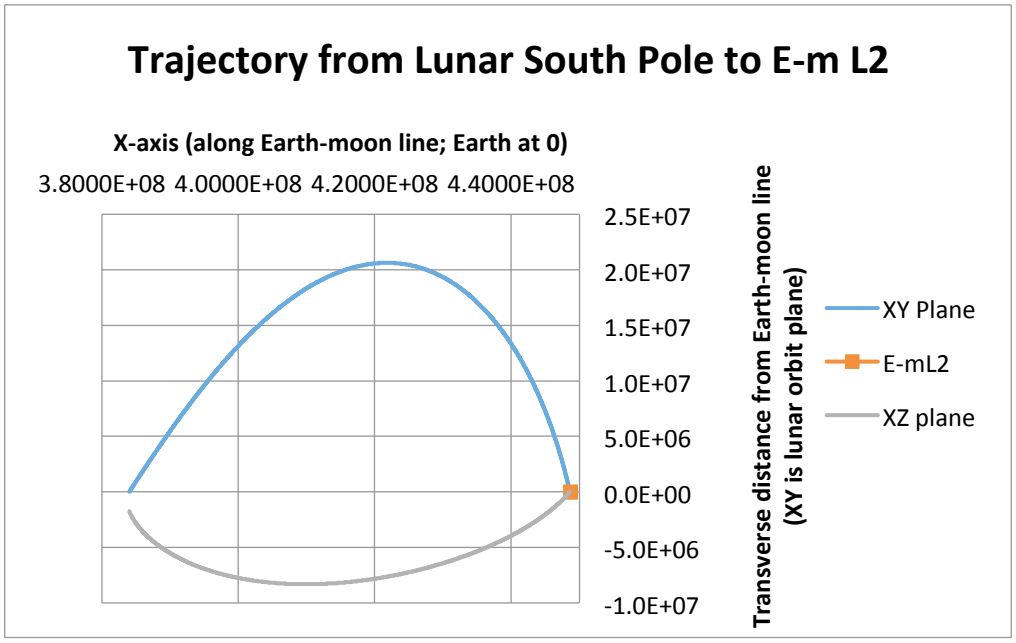

Figure 2.20. Shackleton Crater mass driver trajectory analysis. A mass driver built on the slope of the crater, can deliver ice payloads within 40 km of Earth-Moon L2 with 222 m/s arrival velocity (analysis by Brian Wilcox).

The following is a calculation purely from an energetic point of view, based on the needed kinetic energy of the mass of water at velocity for getting in orbit. Thus, $E = 0.5*mv^2$ gives a kinetic energy of 1 kg at 2.224 km/sec to be **~2.47 MJ.** This would be the energy that needs to be provided by TFs.

3 TransFormers as Key Nodes of a Solar Energy Infrastructure

3.1 TransFormers as Sunlight Reflecting Towers

3.1.1 *Reflection to Longer Distances*

This section summarizes the optical analysis from the Phase I report. The solar intensity at some distance from the reflector depends on how much of the solar disk is seen in the reflector from a point at that distance. For a rover with angular size (relative to mirror) less than that of the Sun (9.3 mrad), the rover only sees part of the Sun reflected, hence receives only a fraction of the incoming sunlight, as illustrated in **Figure 3.1**. The solar flux at 1 AU is 1,353.3 W/m^2. If we observe the Sun through an aperture that is smaller than the Sun's apparent diameter, the relative solar radiant power is shown in **Figure 3.1**. The Moon's axis of rotation is inclined to the ecliptic plane by 1.54 degrees. Thus, from the point of view of a mirror near the south pole of the Moon, the Sun would follow a circular path around the sky, no more than a few degrees above the lunar horizon.

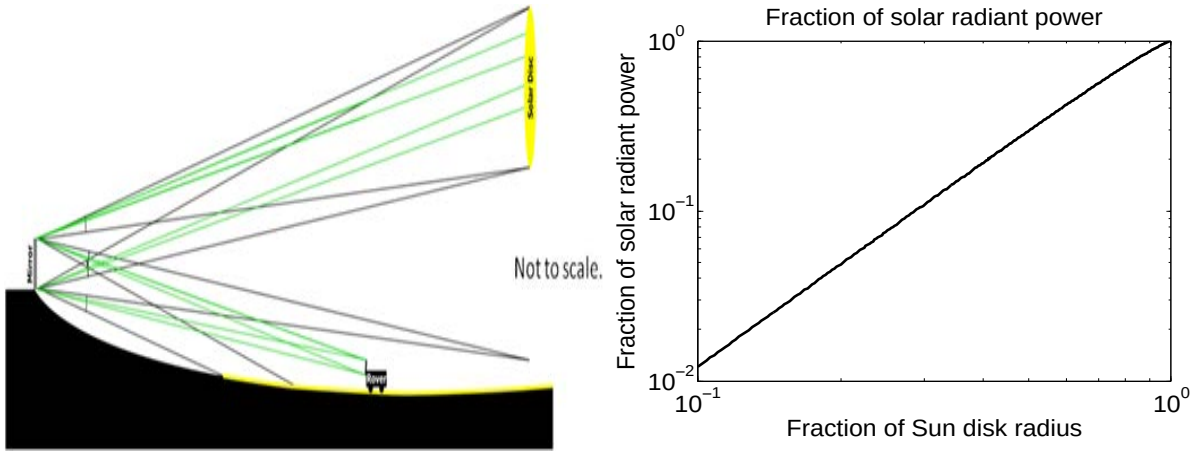

Figure 3.1. Ray tracing of the finite size of the solar disk onto the rover. Fraction of solar radiant power.

The size of flat mirror needed to create 1,353 W/m^2 at 10,000 m is similar to seeing the entire disk of the Sun through a circular aperture at that distance. The diameter of this aperture is then 9.3 mrad × 10,000 m or 93 m. If we assume that the maximum reflection angle is 90 degrees (corresponding to an incidence angle of 45 degrees), then the mirror must be elliptical with dimensions of 132 m × 93 m. Tracking the Sun through 360 degrees of longitude with an angle of incidence no greater than 45 degrees requires two mirrors.

To best track the Sun during the Moon's rotation, a dual elliptic reflector system is being investigated, where one reflector reflects light from the Sun downward onto a second reflector that reflects the sunlight onto the crater floor. In this heliostat arrangement, the top reflector rotates to track the sun, while the bottom reflector is positioned to illuminate select sites on the crater floor. The vertically collinear arrangement will maximize the available sunlight to the illumination region.

One possible arrangement is shown in **Figure 3.2**. While the Sun is in the Cartesian quadrant 1 (top right of figure, not shown), the light is reflected off mirror 1 to the rover. For quadrant 2 (as depicted), using mirror 1 would be a reflection of a too high incident angle, thus, the need for 2 mirrors: the Sun is tracked by mirror 2, and the light is relayed by mirror 1 to the

rover. For quadrant 3, sunlight goes from mirror 1 to mirror 2 to the rover. For quadrant 4, mirror 2 would be used, with mirror 1 as an alternate.

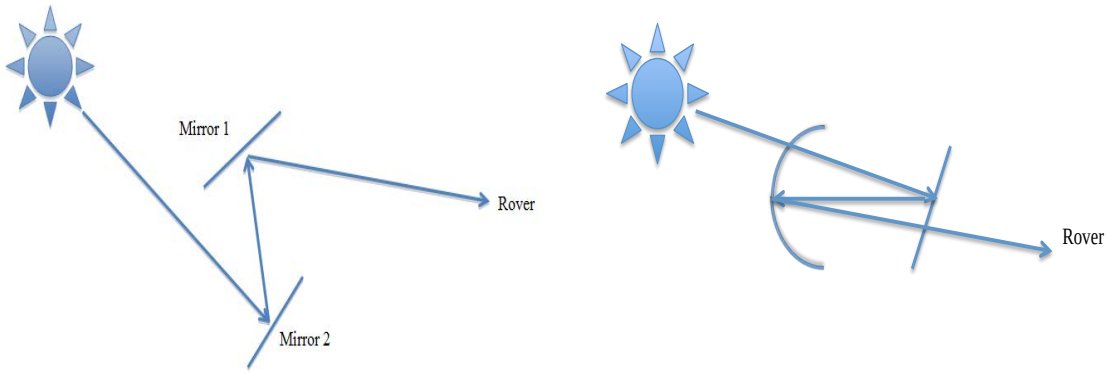

Figure 3.2. Tracking the Sun with two mirrors. Overhead view of flat + curved mirror system for relaying sunlight to a rover.

To derive the tolerance for the flatness of each mirror, regard each mirror as consisting of a large number of small, flat segments. Only the slope or tilt is significant. The tolerance in the mirror segment tilt of 0.5 mrad.

3.1.2 *A Two Mirror Rotational Heliostat*

A continuously operating photovoltaic or reflector power system needs to ensure efficiency as the Sun "rotates" around the horizon. A concept of a rotational system was proposed by Bryant (2010). He also described a TF-reflection functionality. He writes "flat periscope mirrors mounted on the crossbar could be used to direct solar light to areas nearby." He considers this an efficient method of lighting work areas, which bypasses the inefficiencies of the photovoltaic system, battery storage, and electric lighting. If the photovoltaic power system is located on a crater rim, a flat periscope mirror could provide continuous lighting to exploration crews in the permanently shadowed areas within the crater:

> *"Sufficiently large heliostat mirrors could redirect enough sunlight to run photovoltaic arrays at remote locations. This would provide very efficient power transfer for operating within the permanently shaded areas. Transferring solar power with heliostat mirrors can also extend the mission operations time in the permanently shaded areas by removing the need to return to the base for recharging batteries." (Bryant 2011).*

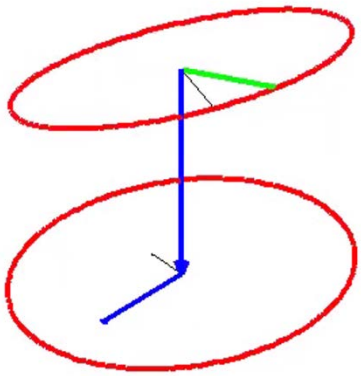

Figure 3.3. Illustration of the two mirror configuration options for the reflector, with the mirrors aligned on top of each other.

These mirrors could be stacked to form a periscope, thus simplifying the tracking of the Sun throughout the lunar day. The first mirror (on top) would rotate 360 degrees to track the Sun and reflect the light down a vertical axis to the second mirror. Mirror 2 would only need to pivot about two axes by a limited amount to track the rover. The lower mirror would be stationary if the target is stationary.

Due to the geometry of tracking the Sun and redirecting to a target area, it is evident that some sunlight will be lost if using circular reflectors. Power projection is limited by the amount of overlap between the mirrors when viewed from the top down, which changes with time (**Figure 3.4**). To roughly quantify the amount of loss we can expect from this dynamic, a plot is generated that shows the percentage of the lower mirror that is illuminated. It is evident in this case (assuming a target location 10 km away and 4 km down) that max solar flux loss would be roughly 25%.

This modeling allows a time-dependent projection coverage map animation, for which 2 frames are shown in **Figure 3.5.** The loss caused by the tilt of the lower mirror is not modeled.

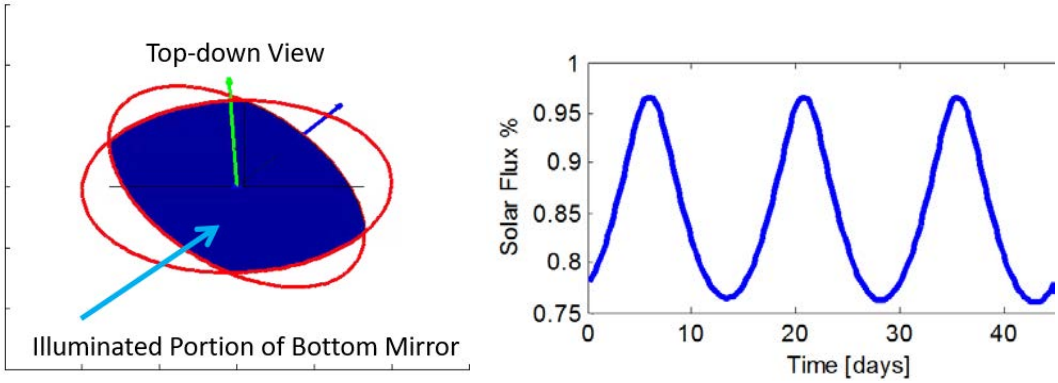

Figure 3.4. Top-down view of the mirrors aligned on top of each other and example of solar power flux available 10 km away and 4 km below.

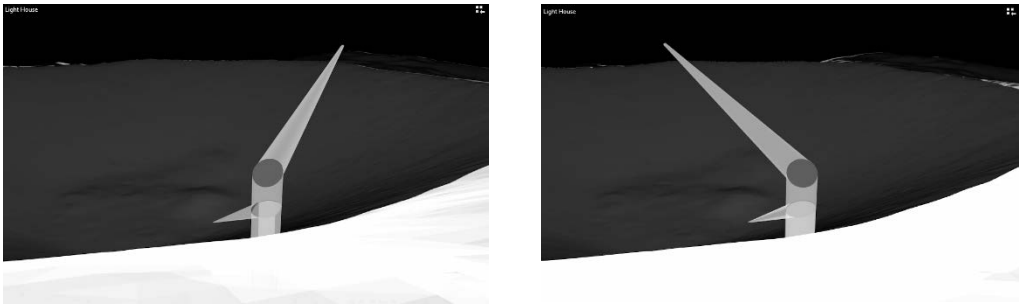

Figure 3.5. Snapshots from simulation of a periscope-like TransFormer, located on the rim of Shackleton Crater, redirecting sunlight as the sun moves around the horizon, reflecting the light to the area of interest inside the crater.

By using a curved mirror, it is possible to concentrate the sunlight somewhat at a range of 10,000 meters. The Sun's disk center has an intensity 1.22 times greater than the mean intensity across the entire disk. Thus, the mirror area can be reduced by 0.82 to give dimensions of 119 m × 84 m. The figure of the mirror would be approximately spherical with a 20,000-meter radius of curvature. The angular range of motion would be ±45 degrees about a vertical axis and ±12 degrees about a horizontal axis (to track the rover).

Due to the low tolerances, these mirrors could be constructed as a large number of flat segments made from a metallized plastic film mounted on a lightweight frame. **Figure 3.6** shows a plot of the solar irradiance vs. distance to mirror (left), and a plot of the solar irradiance vs. diameter of mirror (right).

Figure 3.6 and **Table 3.1** provide data on the solar irradiance vs. distance to mirror for various diameters. If we consider a given efficiency of solar conversion on rover solar panels, and we multiply the area of the panels, we could obtain a similar number for the power generated by the solar panels. For simplicity, we use ~16% efficiency and 6 m^2, their product being 1. Thus, the curves allow an easy reading—to obtain 300 W electric from rover solar panels, one needs a ~40-m diameter when at 10 km (considered as worst-case scenario for Shackleton).

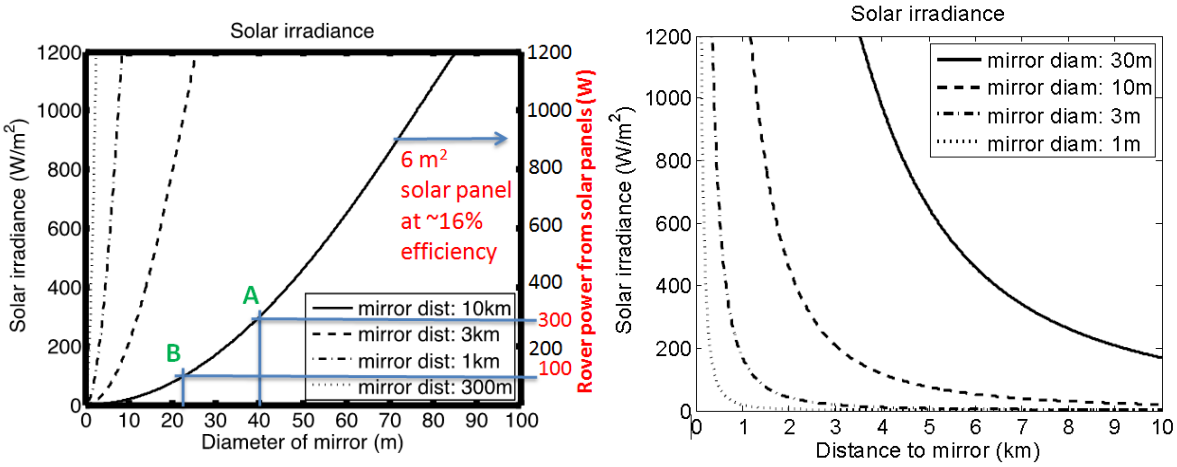

Figure 3.6. Solar irradiance vs. distance to mirror (left). Solar irradiance vs diameter of mirror (right).

Table 3.1. Lever of irradiation (W/m^2) at different distances, and for different mirror diameter.

Distance (km)	Mirror Diameter (m)				
	0.9	2.7	9.0	27.0	90.0
0.1	1300.505				
0.3	169.513	1300.505			
1.0	15.423	137.627	1300.505		
3.0	1.715	15.423	169.513	1300.505	
10.0	0.154	1.389	15.423	13.27	1300

Powering an MSL-like rover at 10 km would require a reflector on the order of 40 m in diameter. This assumes a conservative 16% efficiency in solar conversion, 6 m^2 solar array (increases in conversion efficiency will decrease solar array size); appropriately curved mirrors will buy additional ~10–20% benefit. Lower illumination level should be acceptable (e.g., MER) and can greatly reduce required transformer size. Powering an MER-level rover would require a 25-m diameter.

3.1.3 *A Comparison between Passive Reflection and Laser Beaming*

Assumptions:

- Laser system could have an erectable solar array and use the energy to power laser beams (one for each possible separate power user in the crater)

- The efficiency of conversion from sunlight to electricity would be about 30% (triple-junction solar cells)
- The efficiency of conversion from electrical power to laser light energy would be about 70% at wavelengths where single-junction silicon solar cells can be 80+% efficient (Crump et al. 2008).
- Triple-junction space solar arrays cost ~$1 M/kW and produce ~100 W/kg at 30% efficiency. Single-junction solar cells are available for terrestrial use at a few $/W and can presumably be packaged to produce also 100 W/kg using laser light as the source

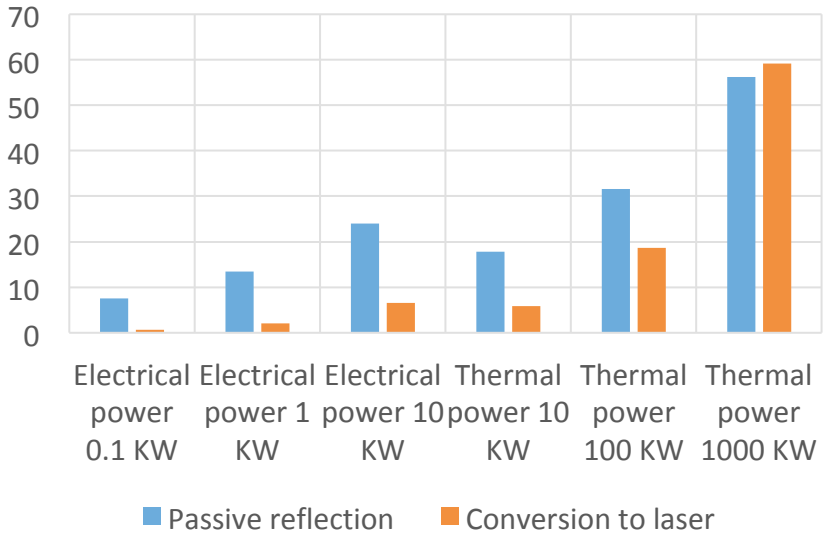

Figure 3.7. Passive reflection vs. laser beaming for various levels of power.

Laser beams pros: the beam divergence angle of a laser can readily be made <10 µrad, while the beam divergence angle of sunlight is fixed at 10 mrad (factor of 10^3).

Laser beams cons: the whole system is more complex and perhaps expensive.

For power <1,000 KW, the laser approach is superior for delivering electrical and thermal power (unless reflectors are much, much less expensive than solar arrays and lasers).

For power ≥1,000 KW, the passive reflection of sunlight is superior for delivering electrical and thermal power.

This concludes that the TF passive reflection approach is superior to the TF conversion to laser approach for power ≥1,000 KW. *As shown in Section 2, the power needed by ISRU is several MW.*

3.1.4 *Design and Operational Considerations for TF*

The scenarios addressed in this study focused on TFs that provide solar energy to rover solar panels, as well as heating, illuminating, and acting as a communication relay. They need to pack in compact form to deploy to a large surface, have good reflectivity, survive in the Sun, be able to provide pointing and, in general, shape control, to embed autonomy for its operations.

Some general considerations for TF are:

- Should use solar energy to power its own operation

- Should use a cellular/modular structure with largely similar modules (except a few possible exceptions), maxing the fabrication cheaper and the design more robust (by redundancy)

The specific requirements driving the design of the TF for the selected set of mission scenarios:

1. Compact volume when packed: ~1 m^3, ~1 m in each of the 3 dimensions;
2. Large surface when deployed: a 40-m diameter circular surface, i.e., ~1,256 m^2 (for simplicity this was rounded to 1,000 m^2 in a number of calculations). This means ~1 mm thin, however, technologies below 100 microns are explored for the surface, with possibly thicker structural elements)
3. Low mass: ~100 kg
4. Highly reflective surface (95% or better, with ~1 mm/m maximum surface deviation, tolerance in the mirror segment tilt of 0.5 mrad)

3.2 Reflectors and How to Fold Them in Small Packages

3.2.1 *Elliptic Origami Reflector*

As an alternative to a reflector composed of many interlocking rigid panels, a single continuous taut membrane has the potential to be much lighter and less complex to design and deploy. To meet required flatness, the reflector membrane must not deform too much under lunar gravity and it must be capable of being pulled sufficiently taut. The deviation from flatness of two taut laminar composite reflector membranes were simulated at a 45-degree angle from lunar gravity.

1. 25 μm aluminized Mylar on a 500 μm die-cut carbon fiber polymer sheet.
2. 25 μm aluminized Mylar on 600 μm Dyneema composite fabric SK99 with a carbon fiber fabric tape spanning the length of the reflector on the opposite side of its reflective surface.

Aluminized Mylar was most often chosen for prototype testing because it can maintain long-term directional reflectivity exceeding 95% and is an order of magnitude cheaper than aluminized Kapton HPP-ST. Since the Young's modulus of Kapton HPP-ST is much higher than Mylar, it is expected that simulations showing the viability of Mylar maintaining flatness under lunar gravity will also show the viability of Kapton HPP-ST as well. The 25 μm reflective membrane thickness is enough for the membrane to resist wrinkling during fabrication. Each laminar composite can be stowed elastically while being rolled around a diameter small enough to be folded in accordance with the crease patterns presented in Section 3.2.3.

A circular reflector ~36 m in diameter, or an elliptic reflector ~33 m by ~46 m, would have the target reflective area of 1,000 m^2. With a packing efficiency[2] of 50%, the reflector must be less than 1 mm thick to fit within the stow volume. The reflector must deviate less than 1 mm/m of distance across the surface so reflected light does not scatter or disperse away from the target illumination area. The reflector must have over 95% long-term directional reflectivity to withstand constant operation under harsh sunlight and to maximize the power reflected.

Previous work on large deployable reflectors has been done for radar systems using mesh membranes, such as the European Space Agency's CRTS reflector, and continuous membranes, such as L'Garde's inflatable rigidizable deployable antennae. In order to generate crease patterns

[2] The percent ratio of reflector volume in the stow envelope to the volume of the stow envelope.

that allow the reflectors to stow to their specifications, the algorithm that generated the crease patterns for the optical shield of JPL's starshade was used. The algorithm receives input such as material thickness, deployed diameter, stowed outer diameter, stowed inner diameter, stowed height, and the number of rotationally symmetric gores that will be produced.

Each long flexible panel that spans from the perimeter to the central disc and is rotationally symmetric about the center is called a gore. Gores are joined together along their creases with Dyneema Composite Fabric tape that is bonded with epoxy to each gore perimeter.

The crease pattern that satisfies those requirements is output along with the packing efficiency, stow volume, gore strain from stowing, and a factor of material compression if applicable.

3.2.1.1 Reflector Materials

The materials were selected such that each of the solar reflector's components would function in the environment of its service for its service lifetime. Materials were selected for their performance under stress, temperature extremes and exposure times, solar illumination, ionizing radiation, micrometeoroid flux, and potential for fabrication.

Lunar Gravity – The gravitational acceleration on the Moon is ~1.6 m/s^2, or ~0.16 g.

Lunar gravity is the greatest source of stress on the torus and the solar reflector. Lunar gravity is also the chief cause of the solar reflector's deviation from flatness. Lunar gravity also complicates the deployment of the solar reflector.

Temperatures and Duration – Solar reflector temperatures were assumed to be less than 373K, with exposures of up to 1 year before cooling to less than 273K for a few Earth days. Materials were also chosen to minimize thermal expansion.

Solar Luminous Flux – Materials must withstand solar illumination with 1367 w/m^2 of radiance with its extraterrestrial spectra.

Ionizing Radiation – Radiation striking the surface of the Moon is composed of galactic cosmic rays with energies of 1–10 GeV/nucleon and a flux of 864 M nuclei/m^2day, solar flare particles with energies of 1–100 MeV/nucleon and a flux of 86.4 G nuclei/m^2day, and solar wind particles with energies of ~1 keV and a flux of 93.3 G nuclei/m^2day.

Micrometeoroid Flux –

30,000 microcraters/m^2yr are expected with diameters $\boxtimes$0.1 μm.

1,200 microcraters/m^2yr are expected with diameters $\boxtimes$1 μm.

300 microcraters/m^2yr are expected with diameters $\boxtimes$10 μm.

0.6 microcraters/m^2yr are expected with diameters $\boxtimes$100 μm.

0.001 microcraters/m^2yr are expected with diameters $\boxtimes$1000 μm.

Micrometeorites are expected to contribute 0.3–42 cm^2/year of lost surface, or <0.00042% of the surface area.

3.2.2 *Origami Stowable Ultralight Reflective Laminar Composite Membrane*

In order to minimize weight, minimize strain, and maintain >95% directional reflectivity in the environment of its service, a laminar composite was chosen whose layers are each well suited to a subset of the design requirements. The laminar composite could be bound using adhesives or sewn in place. <200 mgrays/m^2day of galactic cosmic radiation, <200 mgrays/m^2day of solar

flare particles, and <2 μgrays/m^2day of solar wind particles are expected to be absorbed by the reflector.

Reflective Membrane Layer

Aluminized Kapton® Type HPP-ST was selected due to its low density, high dimensional stability at temperature extremes of −269°C to 400°C, modified surface for better adhesion, and its long-term resistance to ionizing radiation and UV. Its thin film aluminum coating has a broadband reflectivity of >95% in the visible and UV regions. Aluminized Kapton® Type HPP-ST can also be precision cut to distances of many meters with a vinyl cutter.

Creased Gore Assembly Layer

Dyneema® Composite Fabric SK99 tapes were chosen to join reflective gores together and serve as creases along those joints. Dyneema® Composite Fabric is composed of two unwoven layers of parallel running UHMWPE fibers oriented 90° from the other layer, and sandwiched between two layers of polyethylene terephthalate about 1 μm thick. UHMWPE has a very high specific modulus for its density, approaching that of carbon fiber but with much higher abrasion resistance and resistance to flexural fatigue from many cycles of sharp folding. Despite this, UHMWPE creeps under sustained load, whereas carbon fiber fabric tapes do not. Since we are not yet certain if lunar gravity will exceed the threshold to cause creep in an unsupported Dyneema composite fabric reflector, we've assumed that carbon fiber reinforcement is necessary for sustained use. Though the Young's modulus of UHMWPE can be increased substantially and the sensitivity to creep largely removed, by cross linking the polymer under large exposures of γ-radiation.

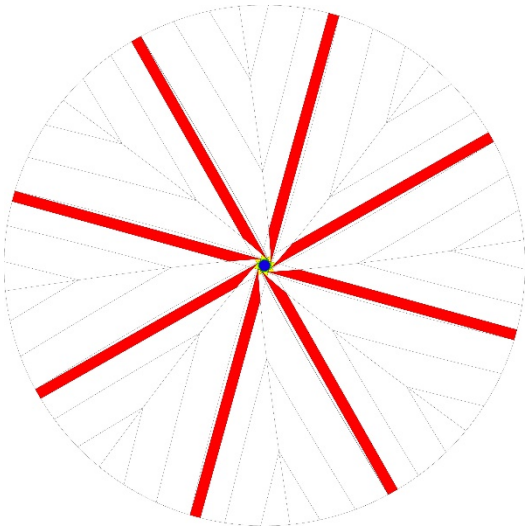

Figure 3.8. Reflector example showing attachment sites of carbon fiber fabric tapes in red.

Load-Bearing Layer

Carbon fiber fabric tapes were selected to maintain flatness and bear the weight of the reflective membrane due to its very high specific modulus and stability under UV and other forms of ionizing radiation. The carbon fiber fabric tapes would span the diameter of the reflector beneath the reflective membrane and adhere only to the inner area of the gores where no creases would intersect the tape. In the stowed configuration, the innermost portion of the tape would cross the central cavity of the stowed origami reflector, and the outer portion of the tape would remain adhered to the gores inside the stowed form. The carbon fiber fabric tapes would extend beyond the dimeter of the reflector and be bonded to the constant force springs that are attached to the torus.

A 1,000 m^2 reflector made from a 50 μm thick layer of Kapton HPP-ST with Dyneema Composite Fabric tapes for gore assembly and carbon fiber fabric tapes for load-bearing capacity would have a mass of 74 kg and have a stow envelope of 1 m^3 with 0.5 m^3 of volume remaining in the center of the stow envelope for other components.

Inflatable Torus

The inflatable torus would be made of a thin gas-impermeable laminar composite membrane that can cure under sunlight and or applied heat and rigidize to maintain its deployed shape. The allowable absorption, reflectivity, and emission spectra of the laminar composite will be determined to choose gas-impermeable membrane materials. If heat would be applied to the torus, a layer of thin electrically conducting wire would be included also. The torus would also have constant force springs attached to the torus' large inner diameter for articulating with the reflective membrane.

Inflation Gas

Due to passive inflation's heightened sensitivity to micro-leaks, the torus could be inflated by pressured gas or evaporating cryogens stowed with the torus and reflector.

3.2.3 *Origami Crease Pattern*

The crease patterns that were generated to suit our design requirements were made using an improvement to the algorithms that generated the crease patterns of the optical shield of JPL's starshade. The algorithm receives input such as thickness of the material, deployed diameter, stowed outer diameter, stowed inner diameter, and stow height, and generates a crease pattern that, when folded, will meet those requirements. See **Table 3.2** for a cross-comparison of crease patterns, associated stow dimensions, and the number of regions, or panels,[3] the membrane must be folded into, to stow the crease pattern.

Two varieties of origami crease patterns of a specific thickness and reflector area (1,000 m^2) were designed and assessed for their packing efficiency and number and type of panels the crease pattern could be folded from. The type that stow material by wrapping are called spiral crease patterns (CPs) and those that stow material through concentric compression folds are called concentric CP here.

[3] The region of a crease pattern bounded by creases or the perimeter. In this report, a rigid panel is a panel that can be made from rigid or flexible material, and a flexible (soft) panel is a panel that must be made from flexible material.

Table 3.2. A comparison of different stowed crease patterns and their stow dimensions. 1,000 m² panels in Crease Pattern 3: reflector vs. thin film photovoltaics – 50% more weight but within same ballpark – very light.

Properties of Solar Panel Spiral Crease Pattern in context										
	Spiral CP1	Spiral CP2	**Solar Panel Spiral CP3**	Spiral CP4	Spiral CP5	Spiral CP6	Spiral CP7	Concentric CP1	Concentric CP2	Concentric CP3
Reflector Area (m2)	1000	1000	**1000**	1000	1000	1000	1000	1000	1000	1000
Thickness (μm)	25	100	**150**	500	500	500	1000	25/100	25/100	1000
Mass (kg) (**Mylar on Die Cut Carbon Fiber Polymer**)	35	139	**235**	695	695	695	1390	34.75/139	34.75/139	1390
Mass (kg) (**Sealed Thin Film GaAs Solar Cells on Kapton**)			**355**							
Envelope Volume (m3)	0.785	1.23	**1.34**	1.38	1.73	2.16	2.68	0.785	1.1	4.21
Packing Efficiency	96%	87%	**84%**	58%	66.50%	74%	39%	3.80%	4.50%	12%
Height (m)	1	1.17	**1.22**	1.2	1.3	1.4	1.5	1	1.4	1.75
Stow Outer Diameter (m)	1	1.16	**1.2**	1.2	1.33	1.4	1.5	1	1	1.75
Stow Inner Diameter (m)	0.96	1	**1**	0.6	0.8	1	0.8	0.21	0.2	1
Number of Rigid Panels	36,176	23,712	**21,804**	24,104	18,816	14,480	12,284	2,520	1,800	1,504
Rigid Panel Width(s) (m)	0.056 - 0.11	0.066 - 0.076	**0.068 – 0.0824**	0.041 - 0.082	0.060 - 0.098	0.068 - 0.13	0.079 - 0.11	0.39	0.39	0.37
Number of Soft Panels	112	96	**92**	92	84	80	74	2520	1800	1504

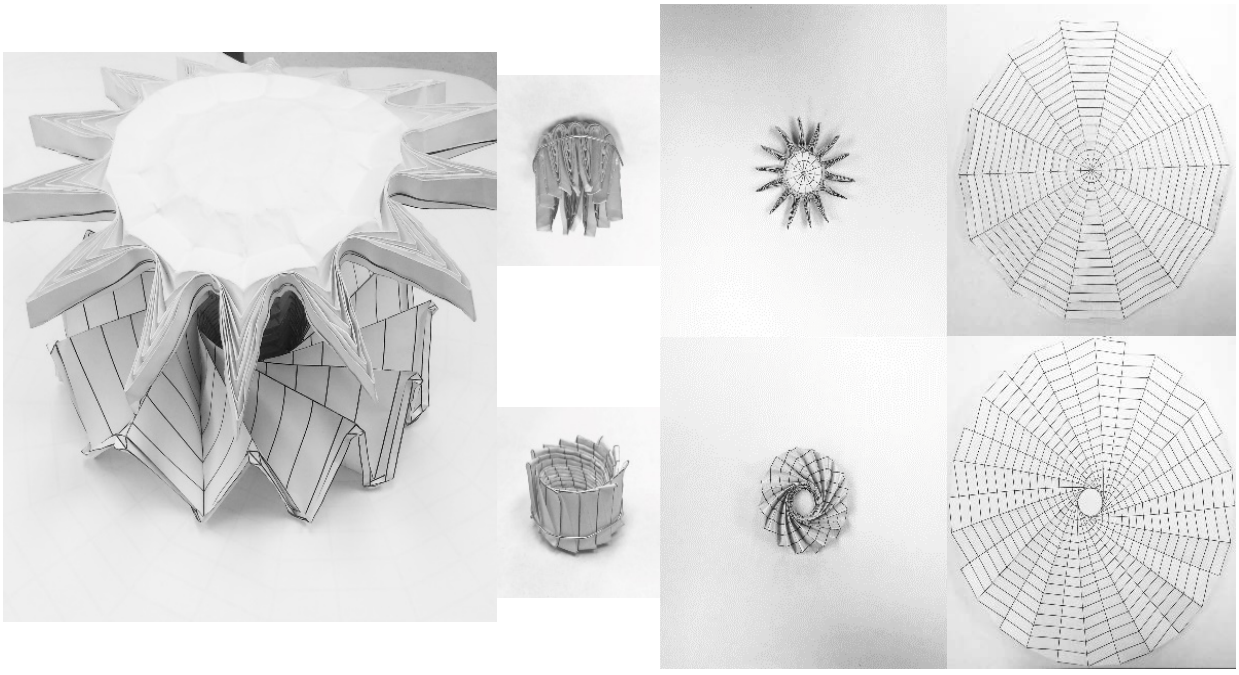

Figure 3.9. Pair of stowed crease patterns stored for joint minimal volume.

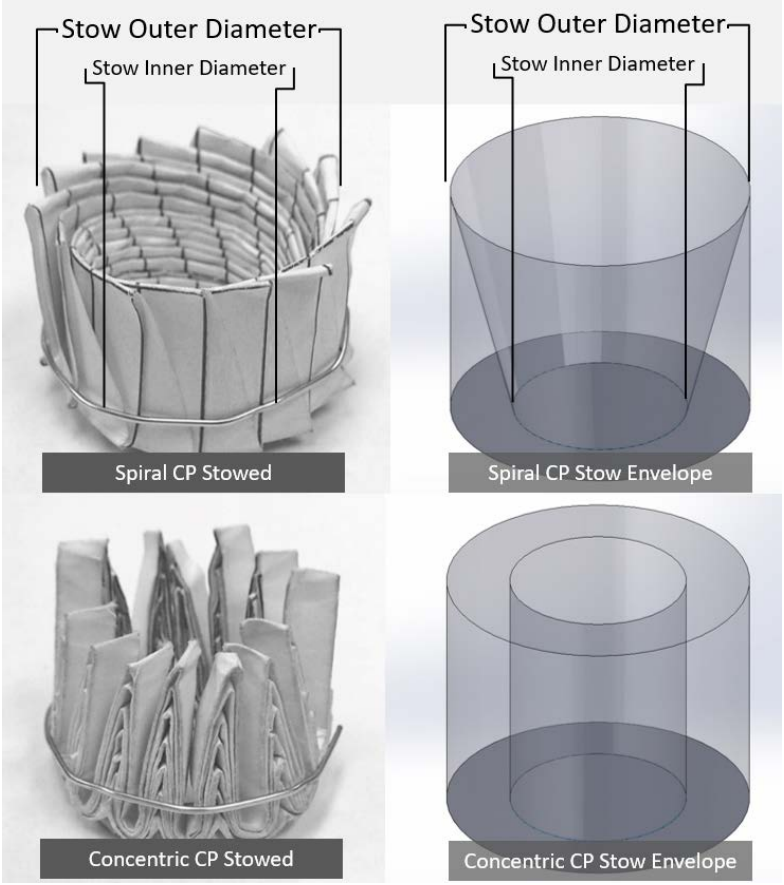

Figure 3.10. Envelope shapes of stowed crease patterns.

Table 3.3. Characteristics of Kapton on die-cut carbon fiber polymer of spiral CP3.

Kapton HPP-ST with Dyneema and Carbon Fiber Fabric	Spiral CP70
Area (m^2)	1000
Thickness (μm)	100
Mass (kg)	74
Volume (m^3)	1
Packing Efficiency	50%
Height (m)	0.88
Number of Flexible Panels	128

3.2.4 *Deployment Mechanism*

An inflatable rigidizable torus was selected to deploy the elliptic reflector. The torus lines the circumference of the reflector and folds with it, with specialized folds that allow for continuous pneumatic channels in the fully folded torus. We considered a passive inflation of the torus with subliming benzoic acid at first, coupled with rigidization of the torus under sunlight. High altitude balloon testing of the torus' inflation mechanism showed that reliance on a passive

inflation system dramatically increases the inflatable's sensitivity to leaks that could be avoided with a single rapid inflation from compressed gas or from evaporating cryogens. Rigidization could be achieved with either a UV-curing resin or a heat-curing resin that relies on sunlight alone or with the assistance of embedded inductor coils. A laminar composite of Dyneema Composite Fabric and Kapton could be used to make the torus.

Maintaining Flatness

Given the very large surface area of a reflector, maintaining flatness is essential in ensuring that sunlight is accurately redirected. The two primary means of achieving the required flatness that were investigated were are a constant-force spring catenary tensioning system and a carbon fiber polymer frame backing system.

The catenary system would be composed of the reflector's perimeter of catenary curves and constant-force springs that are bonded to the reflector's underlying Dyneema composite tapes and similar tapes bonded to the torus.

The second system would be composed of thin sheets of carbon fiber polymer die-cut into a lattice and bonded to the back of the gores of the reflective membrane.

The general approach to evaluate both systems' potential is by developing CAD models and running finite element analyses on each design in Solidworks and Abaqus static simulations.

3.2.5 *Results*

Flatness

A reflector membrane made from 25 µm Mylar on 600 µm Dyneema fabric SK99 with a 40-cm wide, 100-µm thick carbon fiber fabric tape spanning the ellipse opposite the reflective side, fixed along its perimeter, and oriented 45 degrees from lunar gravity should incur no more than 0.00645 mm of deviation over a minimum span of 30 m according to simulation. The simulated maximum displacement is well below the 1 mm/m deviation from flatness requirement as can be seen in **Figure 3.11**. (This is only a first order analysis, and considered only the ideal case of a perfect surface to start with, which will not be the case for a deployable). Being able to nearly fix the perimeter of the reflector by deploying the inflatable torus would be required to achieve this degree of flatness.

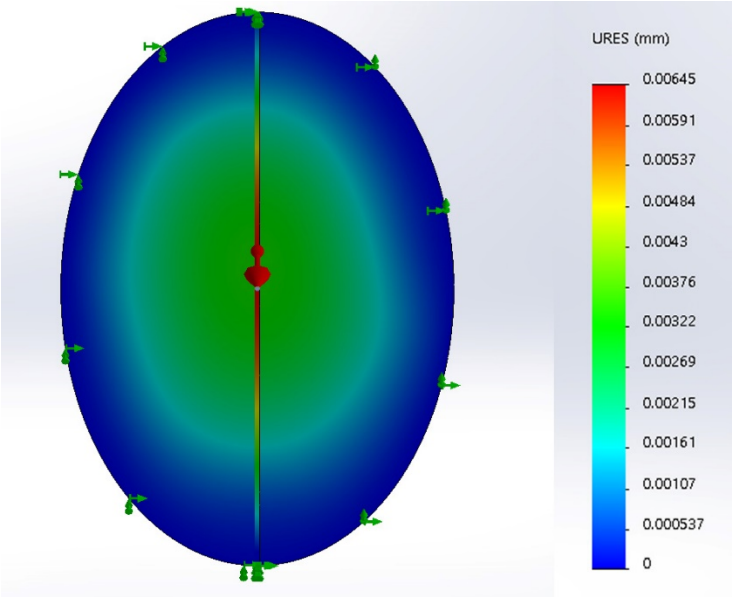

Figure 3.11. Simulation of reflector displacement. Orientation is at 45 degree angles from lunar gravity. Maximum displacement is 0.00645 mm.

Analysis of Potential Rigidizers

A structural analysis of carbon fiber polymer frame systems was evaluated to determine their efficacy in maintaining flatness, and ensuring that the deflection will remain within 1 mm/m deviation. In particular, we used Abaqus to run finite element analysis of a few frames made up of a carbon fiber polymer and Mylar composite. The composite is inspired by tape measure material, whose stiffness is achieved by its unique transverse curvature—in effect, it can only bend along one axis, perpendicular to the longitudinal curvature. This would be effective for a frame that ran along the designed crease pattern, where the maximum reflector deflection exists. Both the models below are of 500 μm carbon fiber polymer sheets, with a diameter of 40 m, 1,550 kg/m^3 mass density, 0.3 Poisson's ratio, and 1.05×10^{11} Young's Modulus.

Figure 3.12 (left) shows the simulation results of a carbon fiber sheet and deflection it experiences when the lunar gravitational force, 1.622 m/s^2, acts at a 45-degree angle. The max deflection is 4.761 cm. **Figure 3.12 (right)** shows the simulations results of a carbon fiber polymer sheet under lunar gravity with 500 μm thick carbon fiber polymer supports extending radially under each gore—there are a total of 21 supports, each of which around 18 m in length. The max deflection is only 4.072 cm. The carbon fiber polymer splines, therefore, make a significant impact in the overall deflection.

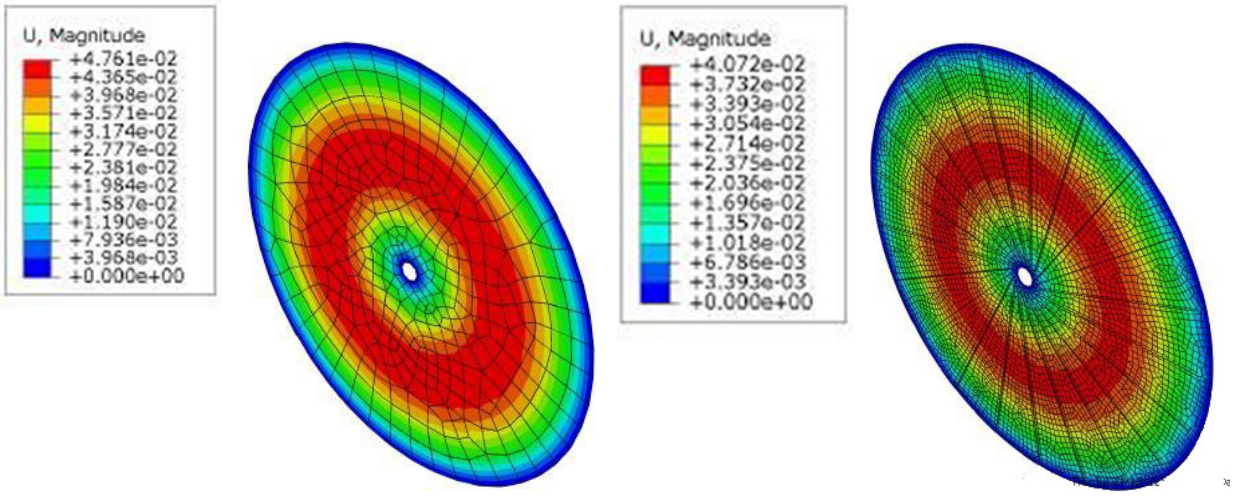

Figure 3.12. Simulation result of carbon fiber polymer sheet without (left) and with (right) radial carbon fiber polymer supports.

Origami Prototypes

An elliptic crease pattern was designed to be folded from a membrane 42.4 m × 30 m and from material up to 700 μm thick, see **Figure 3.13**. The folded form is 1.41 m in height, has an outer diameter of 1.05 m, and an inner diameter of 0.4 m. 0.54 m^3 of volume remains free in the stow envelope, giving the origami a 49% packing efficiency. The radial creases divide the crease pattern into gores that can be adjoined along their perimeter. This crease pattern, **Figure 3.13**, would allow a ~1,000 m^2 solar reflector to be stowed in an envelope 1.8 m^3 in volume with 0.54 m^3 of free bulk volume within the envelope volume that could partially stow another reflector or another item.

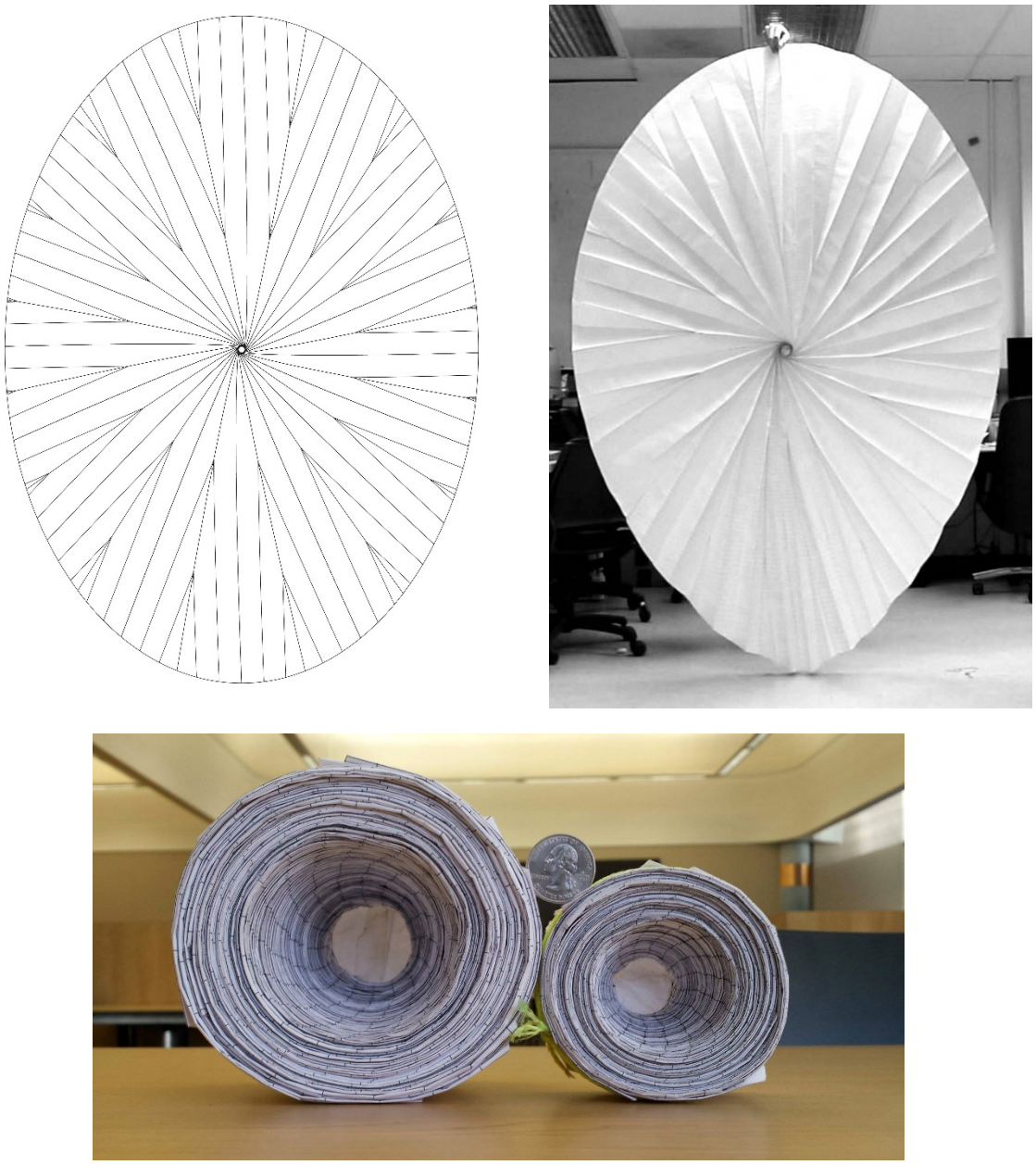

Figure 3.13. Crease pattern that stows to 1/40th of its longest dimension. A 1/16 scale model of an elliptic reflector was also folded demonstrate how it stows and deploys. Partially deployed origami ellipse (top) and same ellipse stowed (bottom). Ellipse is 106 cm × 183 cm.

Deployment Testing

Reflectors deployed with inflatable rigidizable torus have been demonstrated in space (example shown in **Figure 3.14**). The solar reflector designed is a few hundred kilograms of mass and can deploy up to 40 times its stowed diameter. Achieving a torus inflation pressure that can deploy the reflector sufficiently taut to meet the flatness requirement is challenging.

A 1/18 physical model of the Mylar reflector attached to a vinyl and Mylar torus was built to demonstrate the deployable properties associated with expanding the reflector via inflation (**Figure 3.15**).

Three passive inflations of the inflatable torus were tested on a high-altitude weather balloon, though none successfully deployed the torus. The successful inflation of small pouches through low pressure evaporation evidenced the torus' much greater sensitivity to microleaks due to its significantly longer collective seam length.

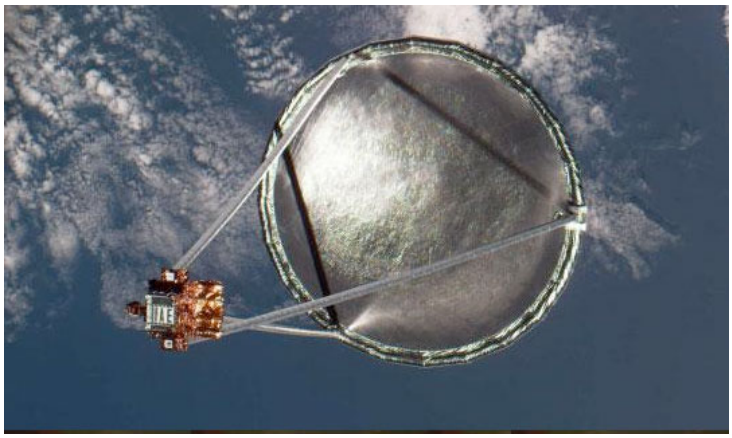

Figure 3.14. Deployed reflector with inflatable rigidizable torus along perimeter by L'Garde.

Figure 3.15. Deployable Mylar sheet with inflatable Mylar and vinyl torus; 2-meter diameter.

3.3 Tower Structure to Support the Reflectors in Periscope Arrangement

This section is based on work performed by NASA KSC and Tectoniks (subcontracted by KSC) for the design and analysis of a Lunar Reflector Inflatable Support (LURIS) structure.

An effective method for supporting the upper and lower suspension points for the reflective surfaces would be a catenary curtain arrangement similar to those used in airship design for the suspension of components such as gondolas and payloads. These have the benefits of distributing the loads evenly into the structure, are very lightweight and pack into a very small volume.

The structure is intended to be deployed from a single container and secured using a spiral anchor from the same container inserted into the lunar regolith. The specifics would depend on the final design. The structure would self-deploy from the container when inflated with gas from a pressurized bottle. The two reflective surfaces are suspended from an inflatable framework and

are adjusted in pitch and yaw by varying the length of their suspension cords. These would be two reflective aluminized Mylar surfaces in a periscope arrangement, with a reflective area of 1,256 square meters each; would maximize the surface flatness of the reflectors by maximizing the tension in the Mylar films; would minimize the structure weight and to minimize the pre-deployment packing volume

The structure would be deployed on the raised rim of the crater to aid with anchoring using minimal ground attachment points. The volume of inflation gas required to deploy the full-scale structure and maintain integrity for 1 hour is also included in this analysis. We do not address here the methods to harden the structure with UV curing or aerosol activated resins pre-impregnated into the inflated structure fabric. The structure is comprised primarily of interconnected inflatable tubular beams with circular cross-sections. Data from tests have been used to develop a means of determining the flexural rigidity for any size of inflatable beam with a circular cross-section at any given inflation pressure, provided the material modulus is broadly similar.

Flexural rigidity varies as the cube of the tube radius. Doubling the radius of a tube would therefore increase flexural rigidity by a factor of 8. However the stresses in the tube would also double. If the pressure in the larger tube was then halved, the stresses would remain the same as those in the smaller tube but the effect upon the flexural rigidity of the larger tube would not be significantly reduced. There is therefore a clear mechanism for significantly increasing flexural rigidity by increasing the tube radius without increasing the loads due to the inflation pressure.

Varying the inflation pressure has a minimal impact upon the flexural rigidity of an inflatable beam (compared with the beams cross-sectional dimensions) but a significant impact upon the induced stresses; thus, it seems that minimizing the inflation pressure would be desirable.

This would permit the use of lighter materials for the construction of the beam. The LURIS periscope tower schematic is shown in **Figure 3.16.**

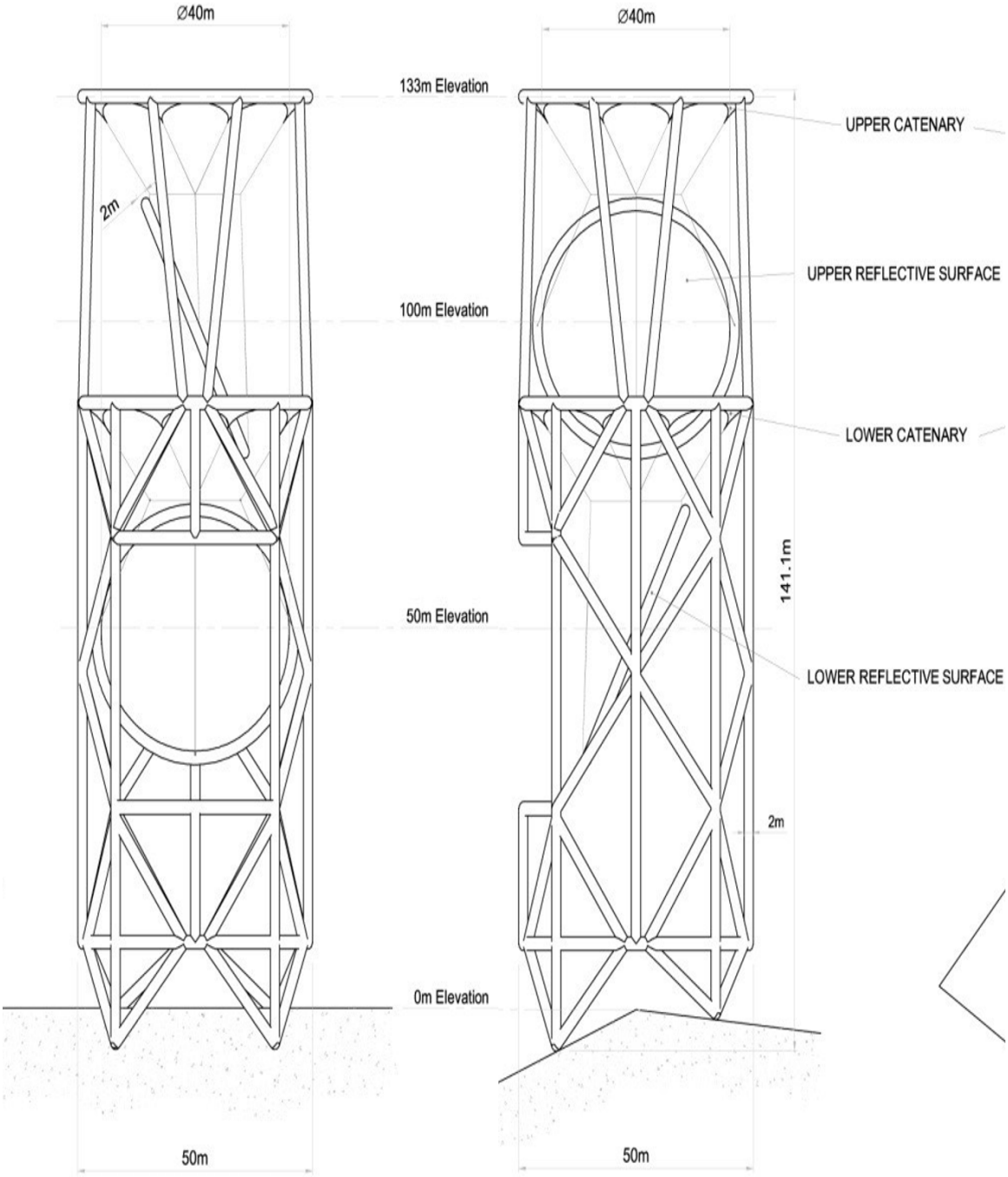

Figure 3.16. Schematic representation of the Periscope Tower with the two reflective surfaces (mirrors).

A thin, flexible membrane cannot support planar compressive loads without wrinkling so these must be removed from the beam by the introduction of pretension in the form of internal pressure. A 2,000-mm diameter tube at a pressure of 18.7 mbar has the same stresses due to the inflation pressure as the 750-mm diameter tube, but has a flexural rigidity of 2.58×10^{11} Nmm^2 (11.7 times that of the 750 mm tube).

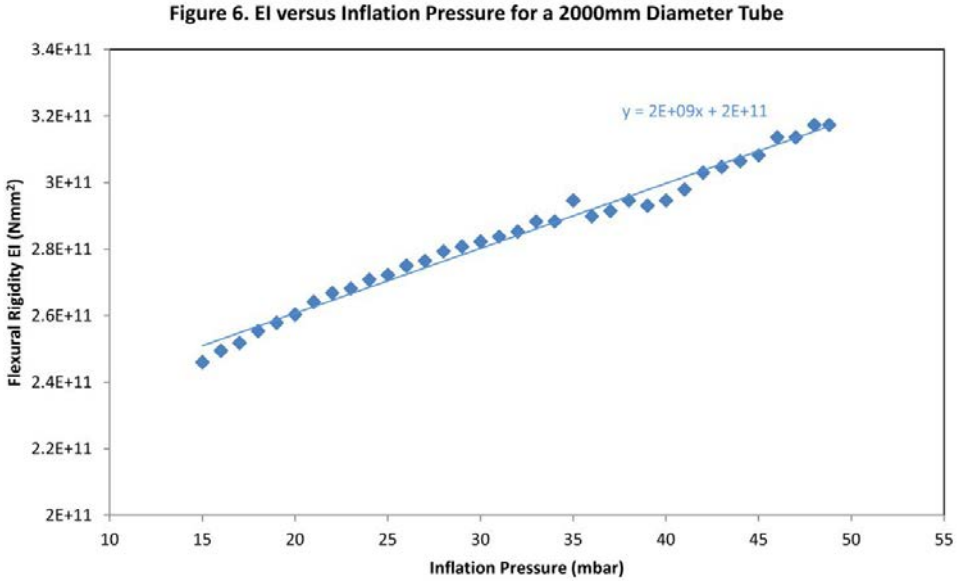

Figure 3.17. Flexural rigidity as a function of inflation pressure for a 2-m diameter tube (Tectoniks).

Figure 3.18. 2-m diameter inflatable beam (Photo courtesy Tectoniks).

3.3.1 *Finite Element Analysis*

The 3D wireframe was imported into the Finite Element Analysis package Strand7. Loads and restraints were then applied to the model. The four contact points of the legs with the ground were restrained in translation but not in rotation. Distributed loads were applied to the beam elements to represent the self-weight of the structure based on Earth's gravity (lunar gravity is accounted for at a later stage when generating load cases).

The self-weights calculated were based on having inflatable beams, which are 2.0 m in diameter constructed from a material weighing 500 g/m^2. These values are used merely to estimate the typical self-weight of the structure as it is not known at this stage what materials would be used for the construction of the full-scale structure, since the aim is to develop methods to harden the structure with UV curing or aerosol activated resins pre-impregnated into the inflated structure fabric.

For the inflatable framework the load per unit length was calculated as follows:

- Beam diameter, d = 2.0 m
- Mass of material, w = 500 g/m^2 (0.5 kg/m^2)
- Mass/weight per unit length of beam (Earth) = n × d × w = 3.142 kg/m (0.03 N/mm)

For the reflector and inflatable rim, the load per unit length was calculated as follows:

- Area of reflector surface = 1256 m^2
- Mass per unit area of 12.7 micron Mylar film = 20 g/m^2 (0.02 kg/m^2)
  - Weight of reflector surface (Earth) = 0.02 × 1256 = 25.12 kg
- Surface area (from CAD model) of inflatable reflector rim = 830 m^2
  - Mass of inflatable reflector rim (Earth) = 830 × 0.5 = 415 kg

The circumference of the inflatable rim (to its centerline) = 131.9 m

Since the weight of the inflatable rim and the reflector film is carried evenly around the perimeter of the rim, the load per unit length to be applied to the rim is:

$$\frac{415 + 25.12}{131.9} = 3.34 \text{ kg/m } (0.033 \text{ N/mm})$$

The weight of each mirror assembly is distributed evenly around the corresponding supporting ring on the main structure via the catenary curtains. The additional distributed load due to this is calculated as follows:

- Mass of mirror assembly = 415 + 25.12 = 440.12 kg
- Circumference of support ring = 150.1 m
- Distributed load = 440.12/150.1 = 2.93 kg/m (0.029 N/mm).

These distributed loads were added to the appropriate beam elements.

The beam elements were then assigned properties to represent their cross-sectional dimensions and material properties. For the purpose of the analysis, the beams were defined as being of a solid circular cross-section, 2.0 m in diameter (note that at this stage these figures are arbitrary).

The maximum deflection of the structure is this case is 363 mm and occurs vertically in the dark blue area shown in **Figure 3.19**. For a structure measuring 133 meters in height, it is assumed that this level of deflection is acceptable.

The modulus of the material used to produce this level of deflection was 318035 Pa.

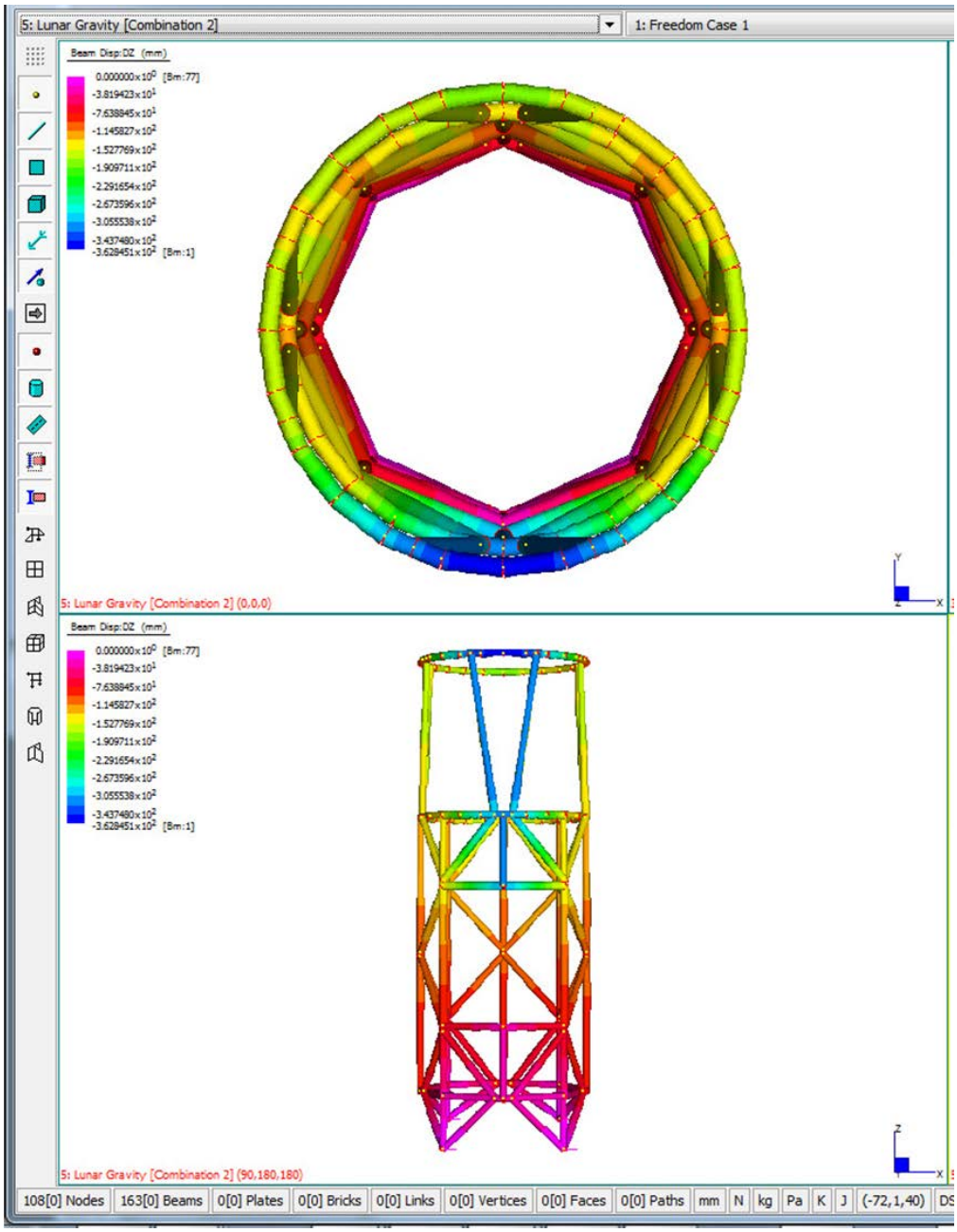

Figure 3.19. Deflection of structure.

3.3.2 *Inflatable Beams*

The beams modelled in the finite element analysis were of a solid circular cross-section, 2.0 m in diameter with a material modulus, E = 318035 Pa (0.318 N/mm^2).

The corresponding dimensions and operating pressure of an inflatable tube with the same flexural rigidity are now calculated and optimized. The flexural rigidity (EI) of the finite element model beams is, therefore:

$$EI = 0.318 \times 7.85 \times 10^{11} = 2.49 \times 10^{11} \text{ Nmm}^2$$

From the testing of inflatable tubes undertaken by Tectoniks, this equates to a 2-m diameter inflatable tube pressurized to 17 mbar. From the testing of inflatable tubes of various diameters

over a range of inflation pressures, the following table (**Table 3.4**) has been compiled showing the tube diameter and inflation pressures of a range of tubes with a flexural rigidity of 2.49×10^{11} Nmm^2.

Table 3.4. Inflatable tubes with equivalent flexural rigidity

Tube Diameter (m)	Inflation Pressure (mbar)
1.0	1045
1.5	138
1.75	30
2.0	17

From the Finite Element Analysis, the peak bending moment in the structure, M, is 948 Nm.

It has been calculated that the peak bending moment in the structure requires a minimum inflation pressure of 6.03 mbar to prevent wrinkling/collapse. This is the case when the tube is inflated to 6.03 mbar (603 N/m^2). If the tube is inflated to 17 mbar (1700 N/m^2) as proposed, then the maximum stress (at point C) is increased by an amount equal p_a*r/2, where p_a is the additional pressure $p_a = 1700 - 603 = 1097$ N/m^2

The peak longitudinal stress is therefore:

$$(603 \times 1) + \frac{(1097 \times 1)}{2} = 1151.5 \text{ N/m}$$

A 500 g/m^2 coated textile (such as a coated polyester) typically has a uniaxial UTS of around 250 daN/50 mm (50,000 N/m). By comparison, a typical coated textile weighing 100 g/m^2 (such as a coated high-tenacity nylon) has a uniaxial UTS of around 90 daN/50 mm (18,000 N/m). A typical lightweight coated textile weighing 50 g/m^2 (such as a coated 30 denier, high-tenacity Nylon) has a uniaxial UTS of 39.5 daN/50 mm (7,900 N/m).

The stresses predicted in the lunar reflector inflatable support structure are within the limits for such textiles, depending upon the factors of safety required:

- Arrangement of the structure
- Buckling check

The peak compressive axial load is 2581 N.

3.3.3 *Mass of the Structure*

The surface areas of the various sections of the structure are:

- Main inflatable framework: 15,105.5 m^2
- Inflatable mirror rims: $2 \times 873.4 = 1{,}746.8$ m^2
- Reflective surfaces: $2 \times 1256.6 = 2{,}513.2$ m^2
- Catenary curtains: 323.2 m^2

Assuming **a mass of 500 g/m^2** for the inflatable elements and 20 g/m^2 for the reflective surfaces (based on a 15 μm metallized film), **the total mass of the structure is:**

$$(15{,}105.5 + 1{,}746.8 + 323.2) \times 0.5 + (2513.2 \times 0.02) = \mathbf{8{,}638\ kg}$$

If it is found that the requirements for strength and other parameters can be met using lighter materials, then the weight of the finished structure will decrease accordingly. For weight of the

inflatable materials remaining larger than that of the reflective surfaces, a reduction in weight follows an approximate linear reduction in surface weight; for 10× reduction to **50 g/m^2 material**, the total mass becomes about 10 times less, i.e., ~ **900 kg**.

3.3.4 *Packed Volume*

For a given surface area of material, the packed volume of the finished structure will depend primarily upon the thickness of the material used and the packing efficiency that can be achieved. **Table 3.5** shows a comparison of inflatable structures of various types and their typical packed volumes and packing efficiencies.

Table 3.5. Comparison of packed volumes of inflatable structures.

Structure Type	Structure Surface Area (m^2)	Structure Weight (kg)	Packed Volume (m^3)	Material Weight (g/m^2)	Material thickness (m)	Volume of material Used (m^3)	Packing Efficiency (%)
Hot air Balloon	909.7	95	1.96	104.4	0.00015	0.136	6.96
Inflatable Building	4000	1960	16.67	490.0	0.00041	1.640	9.84
Echo 1 Satellite	3532	59.1	0.15	16.7	0.000012	0.042	28.26

The packing efficiency has been calculated as follows:

$$\text{Packing Efficiency} = \frac{\text{Volume of Material Used}}{\text{Packed Volume}} \times 100\%$$

Both the hot air balloon and inflatable building structures were packed with no particular folding sequence into flexible (fabric) packaging and compressed as tightly as possible using manpower alone. It can be seen that despite the significant differences between the material weights and thicknesses, the packing efficiency for both fell in the range of 5–10%. These types of structure are packed repeatedly with the time taken to pack them being a primary factor, hence, the absence of a specific folding sequence. The Echo 1 satellite used a specific folding sequence. The data (Hansen 1995) show a much higher packing efficiency—typically 3 to 4 times that of the other structures.

The packing efficiency of the lunar reflector inflatable support structure is anticipated to fall somewhere between the two levels. Assuming a packing efficiency of 18% can be achieved, its packed volume is as shown in **Table 3.6**.

Table 3.6. Packed volume of the lunar reflector inflatable support structure – 500 g/m^2 material.

Structure Component	Structure Surface Area (m^2)	Material thickness (m)	Volume of material Used (m^3)	Packing Efficiency (%)	Packed Volume (m^3)
Main Inflatable Framework	15105.5	0.00041	6.193	18	34.41
Inflatable Mirror Rims	1746.8	0.00041	0.716	18	3.98
Catenary Curtains	323.2	0.00041	0.133	18	0.74
Reflective Surfaces	2513.2	0.000015	0.038	18	0.21
				Total	39.33

This is based on using a 500 g/m^2 coated textile for the inflatable elements and a 20 g/m^2 metallized film for the reflective surfaces. Taking the analysis further, if a 50 g/m^2 material was used with a thickness of 0.076 mm (akin to a lighter-weight hot air balloon fabric), the packed volume is reduced further as shown in **Table 3.7**.

Table 3.7. Packed volume of the lunar reflector inflatable support structure – 50 g/m^2 material.

Structure Component	Structure Surface Area (m^2)	Material thickness (m)	Volume of material Used (m^3)	Packing Efficiency (%)	Packed Volume (m^3)
Main Inflatable Framework	15105.5	0.000076	1.148	18	6.38
Inflatable Mirror Rims	1746.8	0.000076	0.133	18	0.74
Catenary Curtains	323.2	0.000076	0.025	18	0.14
Reflective Surfaces	2513.2	0.000015	0.038	18	0.21
				Total	7.46

3.3.5 *Inflation Gas Volume*

From the CAD model generated, the total volume of the inflatable portions of the structure is 8,382.75 m^3. The target inflation pressure (differential) is 17 mbar (1700 Pa). Assuming a total vacuum exists on the lunar surface, the absolute inflation pressure is therefore also 17 mbar (1,700 Pa). Assuming an atmospheric pressure of 101325 Pa on Earth, the volume of gas required at standard atmospheric pressure is found from the equation:

$$P_1V_1 = P_2V_2$$

Which becomes:

$$1700 \times 8{,}382.75 = 101325 \times V_2$$

Therefore, the volume of gas required at standard atmospheric pressure is 140.6 m^3.

This calculation neglects the effects of temperature as it is anticipated that the deployment of the structure on the lunar surface would occur at the point in the temperature cycle when the temperature is similar to that of the standard atmospheric temperature on the surface of the Earth.

Based on experience with leakage rates in inflatable structures, it is anticipated that the volume of gas required to maintain integrity for 1 hour once the structure is deployed would be less than 5% of the volume required for the initial inflation making the total volume of the inflation gas required:

147.6 m^3 (at standard atmospheric pressure of 101325 Pa).

It is worth noting that inflatable structures maintain their pressure for longer when the ratio of surface area to volume is lower. This is another advantage of using larger diameter tubes for the lunar reflector inflatable support structure.

Reflector Actuation – A mechanism was designed consisting of two motor/gearheads, a cable management system, motor controller, and software code. This system suspends the upper reflector from cables and rotates the reflector to follow the sun as it moves around the horizon above the Shackleton Crater rim. The lower reflector is suspended by cables and is able to be positioned such that it is able to reflect the sunlight from the top reflector to any desired area the crater floor. This technology is described in NASA NTR #1506720006 “Inverted Stuart Platform Reflector Positioning Mechanism.”

Figure 3.20. (Above) Tectoniks inflatable TransFormer scaled prototype in its deflated configuration in the NASA KSC Swamp Works Laboratory.

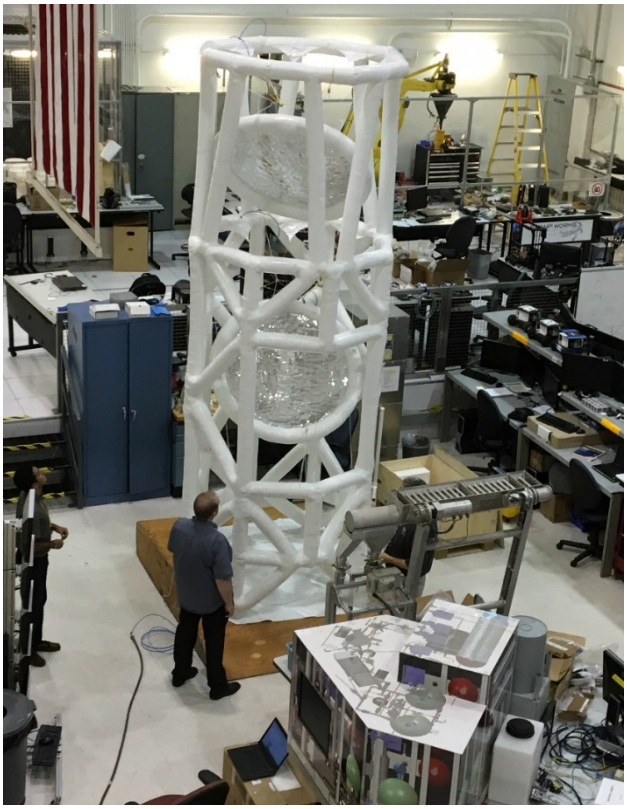

Figure 3.21. (Right) Tectoniks inflatable TransFormer scaled prototype in its fully inflated configuration in the NASA KSC Swamp Works Laboratory. The lander in the lower right of the photo is a an ISRU lander mock-up containing a hopper lift system, soil dryer, water clean-up module, and umbilical to transfer the water to rovers.

A pre-prototype TransFormer reflector was designed and fabricated by NASA/KSC and by University of North Dakota Associate Professor Pablo de Leon to better understand reflector deployment and tensioning techniques. This reflector deployment technique worked well and should be considered in the trade space for future reflector deployment/tensioning mechanisms (**Figure 3.22**).

Components/Materials

a. Controller – LININ Model # 302
b. Pan/tilt – LININ Model PTS-303Q
c. Camera tripod – ADORAMA 3POD Orbit 4
d. Reflector – emergency Mylar thermal blanket
e. Bladder material – Herculite

3.3.6 *Reflective Materials in Extreme Lunar Environment*

Visible light reflectance testing of a reflector was performed in which the team used an LED array (lower left) positioned 4 meters above the reflector (center) at a 19-meter distance to test the visual effects of reflecting light onto the laboratory floor from an unfolded (wrinkled) aluminized Mylar sheet (**Figure 3.23**).

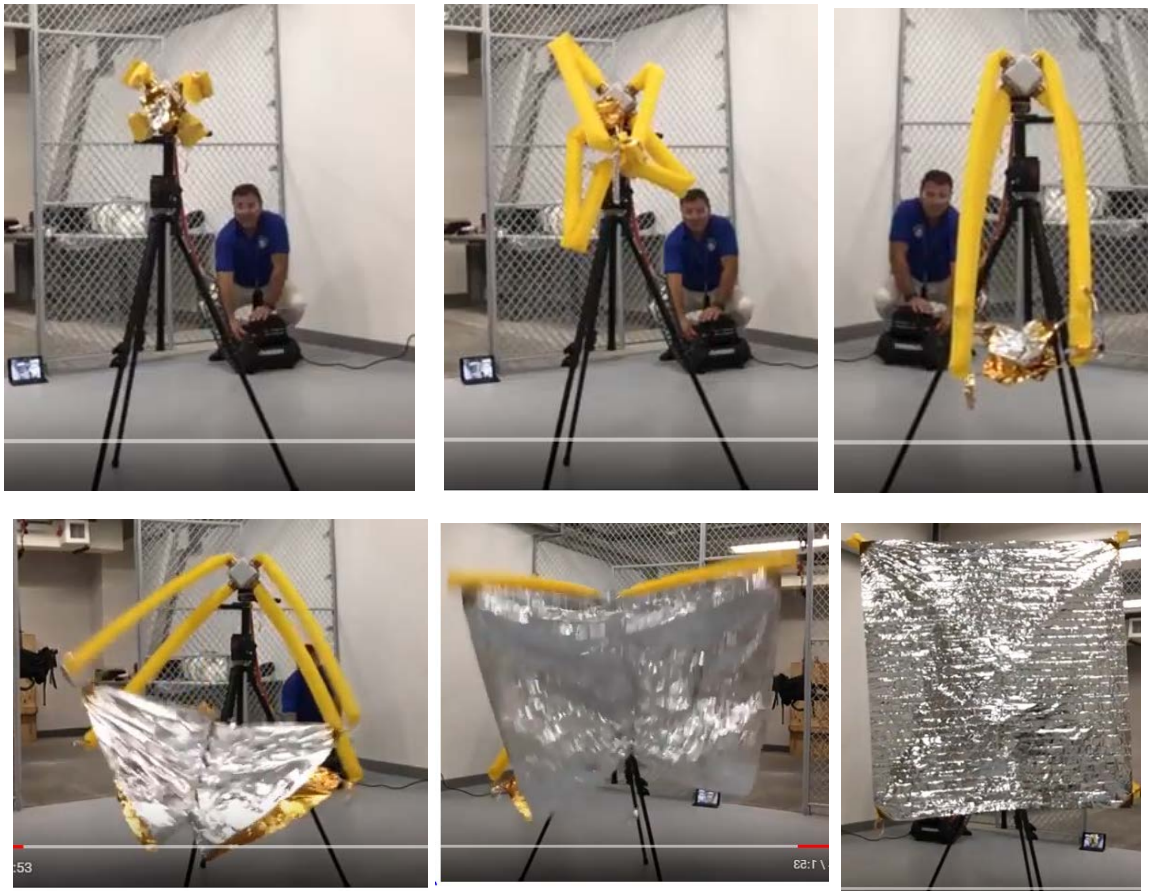

Figure 3.22. Inflation test of a pre-prototype reflector.

Figure 3.23. TransFormer reflectance testing. An LED array is shown reflected by a wrinkled Mylar sheet onto a laboratory floor.

3.4 Coping with the Dust

During NASA's Mars Exploration Rover Mission, dust accumulation on MER's solar panels resulted in a 0.14% loss in power per sol and no power generation after one year. The solar reflective surfaces of a NIAC TransFormer are expected to be positioned several meters above the lunar surface at the rim of Shackleton Crater. Absent any nearby operations that disturb the surface regolith, the importance of dust mitigation for a TF diminishes with increasing altitude above the lunar surface. However, spacecraft landing within sight of a TF, as well as vehicles traversing over the nearby lunar surface, might produce streams of dust that can reach the height of the TF's reflective surfaces. In this case, dust mitigation must be implemented since any dust that adheres to the reflective surfaces will reduce the efficiency of solar energy reflectance (Landis & Jenkins 2002).

The NASA Lunar Science Institute (NLSI) Dynamic Response of the Environment at the Moon (DREAM) team has proposed that any permanent light/dark boundary will give rise to oscillations, in the form of vertical and horizontal movement, of lunar dust (Collier et al. 2013). This movement coupled with the electrostatically charged state of lunar dust creates an environment where a TF surface may become quickly covered with lunar dust hampering its effective operation.

A potential mitigation strategy that uses alternating electric fields to clean solar panels (Sims et al. 2003) could be leveraged. During the deployment of a TF, there is a risk of the reflective surface of a TF making contact with lunar regolith dust either directly or indirectly by some other mechanism interacting with the regolith so as to lift dust, such as by the motion of wheels of a nearby rover or the digging of an excavator. Methods of mitigating dust buildup on the reflective surfaces of TFs include active and passive strategies.

A key technology for protection from dust is an electrodynamic dust shield (EDS) (Stankie 2013). Thin wires made from conducting film are embedded in surfaces; these can be made transparent when used with the reflective surface. An electric field is created through the wires, which propagates outward in a transverse wave-like motion carrying the dust particles along. For solar panels, Indium-tin-oxide wires have been used, similarly, for reflective films that cover infrastructure components including rovers, and ISRU units one have used aluminum or silver wires. The power requirement for EDS are in the milliWatts range. Honeybee Robotics has developed dust-tolerant utility connectors and related mechanisms. The EDS is been extensively tested in the laboratory under simulated lunar and martian conditions, and on a reduced gravity flight at lunar and martian gravity.

3.4.1 *Definitions*

Regolith: General term for the mantle of a planetary body consisting of loose, incoherent, or unconsolidated rock material, of any origin, size or character, that forms the surface of nearly every rocky planetary body.

- Definition adapted from the Glossary of Geology, 1972
- Most lunar regolith is formed by hypervelocity meteorite impacts
- Lunar regolith is spatially very heterogeneous in composition and particle size distribution compared to terrestrial regolith

Dust: An informal term – governmental regulatory definitions of "dust"-related health issues are established for particle sizes smaller than 10 μm and 2.5 μm, where 1 μm (micron) is 10^{-6} meter.

Lunar Dust: Particles of lunar regolith <20 μm in size.

- Convention informally adopted at a NESC Lunar Dust Workshop at Ames Research Center, Jan 2007
- The departure from American regulatory definitions in part reflects the lower surface gravity of the Moon

Lunar Regolith Simulant: Synthetic analogue that approximates, to a known extent, one or more regolith properties at a particular lunar location or region.

Lunar Dust Simulant: A regolith simulant where virtually all particles are less than 20 μm in size.

3.4.2 *Triboelectric Charging*

Fine dust on the micron scale can adhere to a surface via van der Waals and electrostatic forces. A moving body, such as a rover or an astronaut, will experience triboelectric charging as a result of motion through or over lunar regolith. The basic mechanism involved in triboelectric charging, also known as tribocharging or the triboelectric effect, is a result of contact charging, whereby surfaces become electrically charged after making contact with each other. Often associated with frictional contact, such as rubbing, the effect only requires that the materials first come into contact and then separate. The strength of the resulting charge as well as the polarity acquired by each of the two materials depends on material properties. While the most important of these properties is known to be electron work function, properties such as surface roughness and temperature can compound the problem. For this reason, attempts to predict the actual response of engineering systems are often only partly successful and generally require testing under realistic conditions. The magnitude of the effect depends on the difference in work function between the materials involved. While the effective work function of in-situ lunar dust is not known, and probably differs from that of any lunar regolith simulant, it is believed to be approximately equivalent to that of platinum. What is not known is how sensitive tribocharging is to the effective work function. It is likely that careful attention to work function in the selection of materials and coatings can considerably reduce the charging problem.

3.4.3 *Dust Mitigation Techniques*

3.4.3.1 Electrodynamic Dust Shield (NASA KSC)

NASA Kennedy Space Center developed a dust mitigation technology called EDS that uses electrostatic and dielectrophoretic (DEP) forces to disperse and remove dust particles already deposited on a surface, thus preventing the accumulation of dust that either approaches the surface or is already deposited on the surface. The dust particles move in reaction to an applied electromagnetic field due to their electrostatic charge and dipole moment. The electromagnetic field is generated by supplying a three-phase voltage to an array of parallel metal conductors embedded in a dielectric substrate (Johansen et al. 2017; Macket et al. 2016; Dominguez et al. 2017).

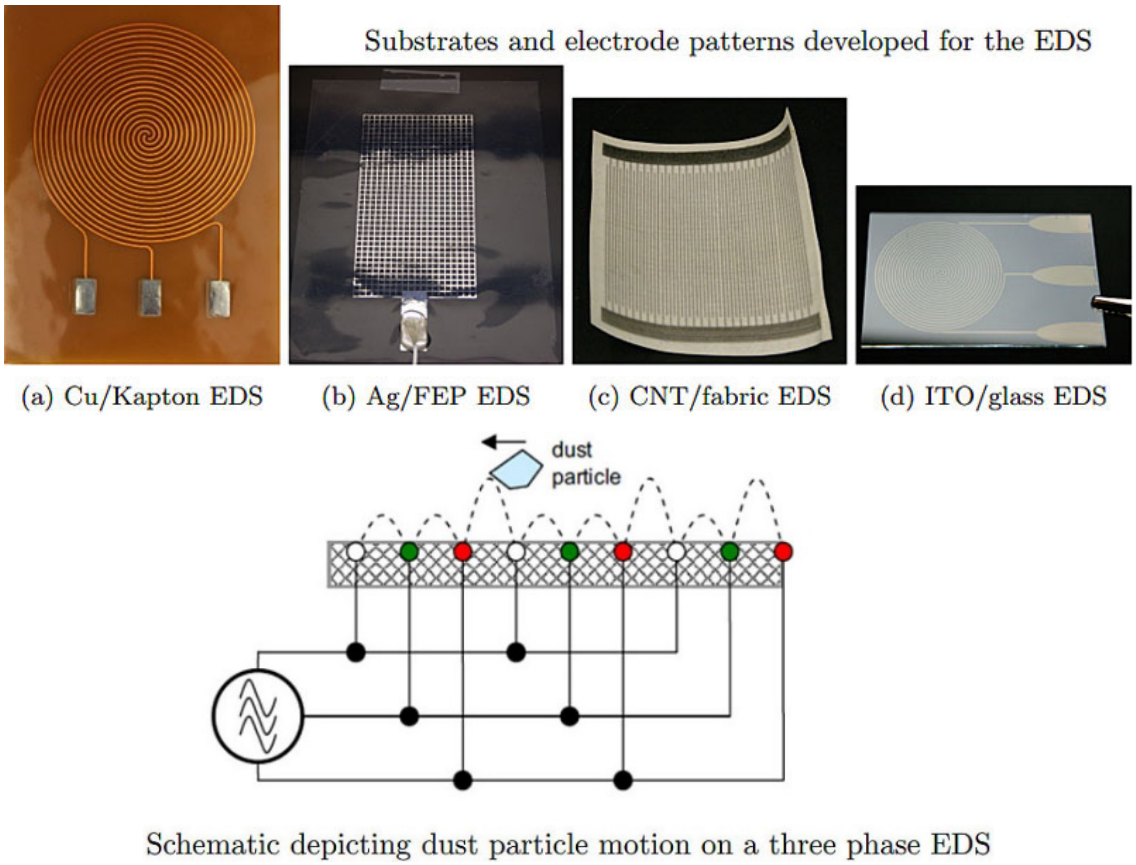

Figure 3.24. Various substrates and electrode patterns for developed EDS (top) and schematic depicting dust particle motion on a three phase EDS (bottom).

3.4.3.2 Anti-dust Coatings, e.g., Lotus Coating (NASA GSFC/KSC)

The lotus coating sheds dust particles by utilizing anti-contamination and self-cleaning properties that minimize dust accumulation on spacecraft surfaces. Shedding of dust particles is accomplished by reducing the surface energy and the amount of surface available for attachment (Margiotta et al. 2010; O'Connor & Abraham 2015; Margiotta et al. 2011).

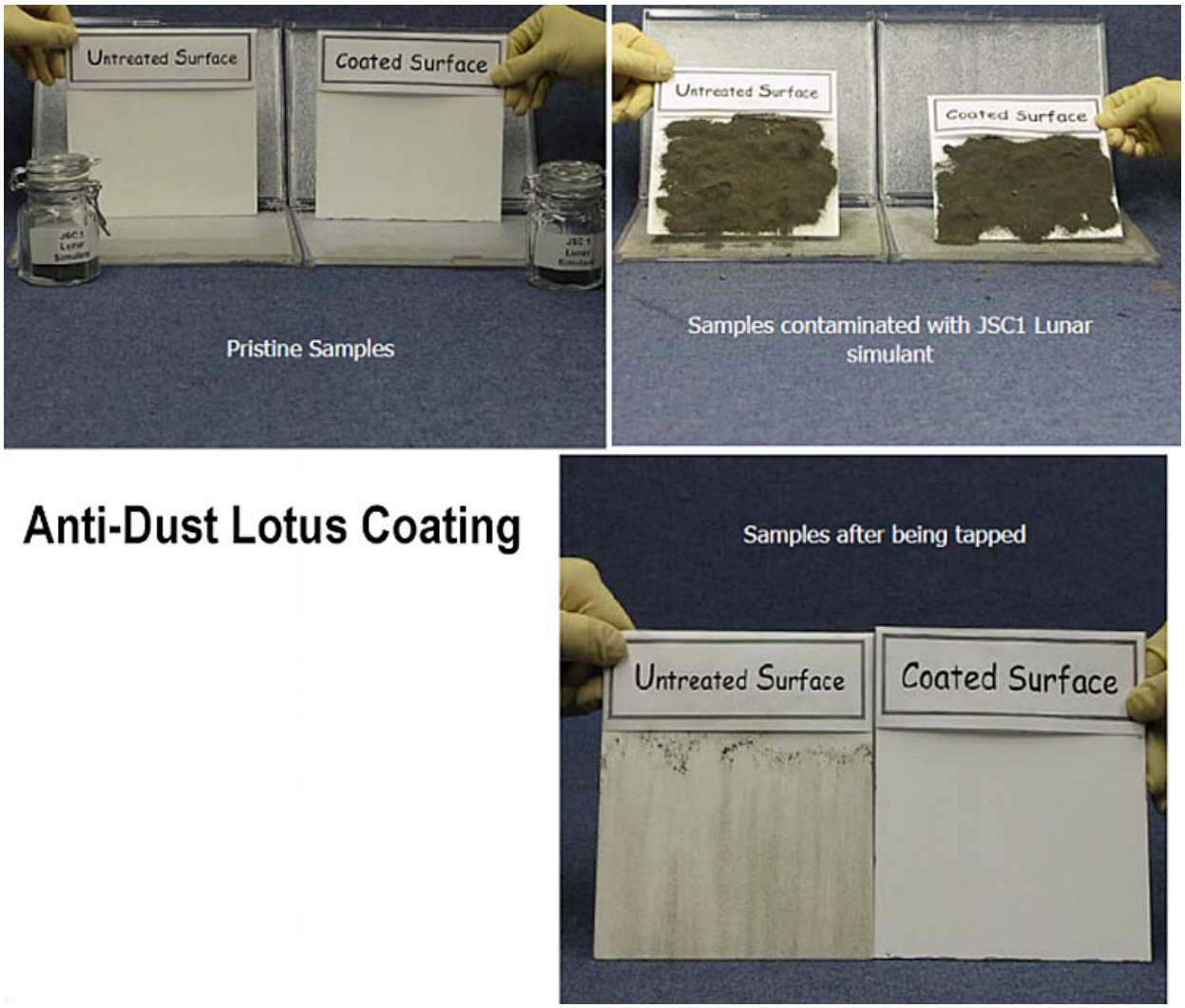

Figure 3.25. Anti-dust coating comparing untreated and treated surfaces of a pristine sample(top left), samples contaminated with JSC1 lunar simulant (top right) and samples after being tapped (bottom right). This demonstrates how anti-dust lotus coating can help protect surfaces.

3.4.3.3 Tilted Surface, e.g., Solar Panel (NASA GRC)

Settled dust can be removed via two-axis gimbal articulation integrated into a solar panel array for a Precursor Mission for Human Exploration of Mars. The arrays are able to tilt 45 degrees for Sun tracking and for dust mitigation (McNatt et al. 2016).

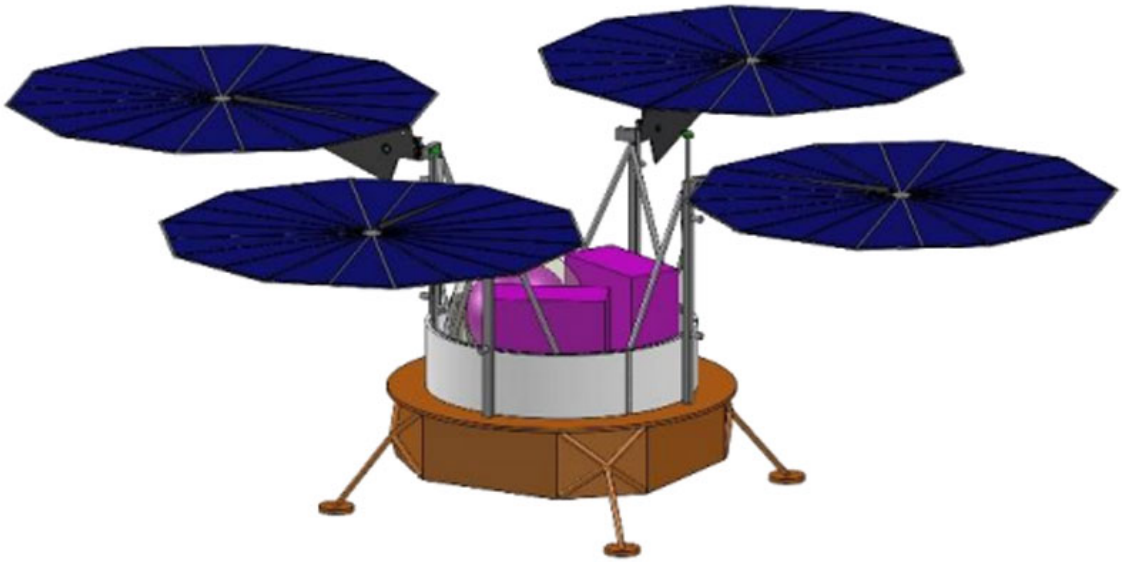

Figure 3.26. Mars ISRU concept lander with 5.6-meter diameter Ultraflex solar arrays. The arrays have the ability to tilt up for 45 degrees both for Sun tracking and for dust mitigation. Settled dust is removed via two-axis gimbal articulation.

3.4.3.4 Piezoelectric Vibration (NASA JPL)

Piezoelectric vibrational actuators are incorporated into the structural supports of solar photovoltaic panels for the purpose of occasionally inducing vibrations in the panels in order to loosen accumulated dust. Provided that the panels were tilted, the loosened dust would slide off under its own weight (Dawson et al. 2004).

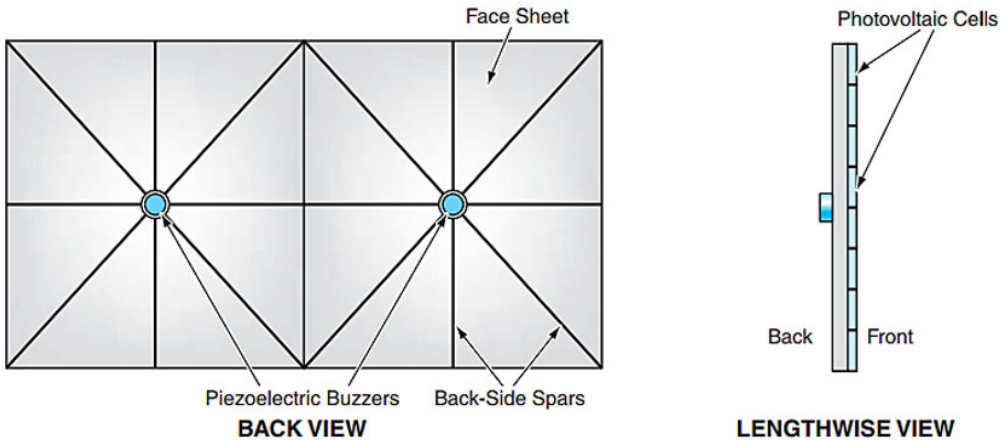

Figure 3.27. Piezoelectric buzzers showing the back view and the lengthwise view. The piezoelectric buzzers would be mounted at nodes of a grid of spars that support a solar photovoltaic panel.

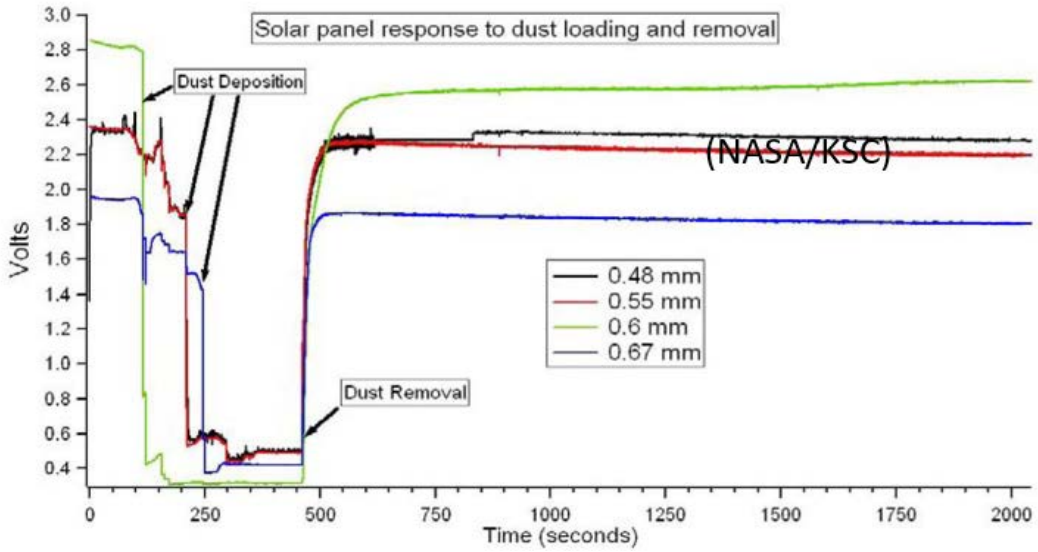

Figure 3.28. Solar panel responses to 50–75 µm JSC-1A dust deposition and removal under high vacuum conditions. Removal was accomplished using dust shields of four different electrode spacings: 0.48 mm, 0.55 mm, 0.6 mm, and 0.67 mm.

3.4.3.5 Mechanical Wiper (NASA JPL)

Electroactive polymers (EAP) produce a large displacement in response to an applied voltage. Using a bending EAP type material, a dust wiper was developed to remove dust particles that accumulated on the surface of an optical window (Bar-Cohen 1999, 2001).

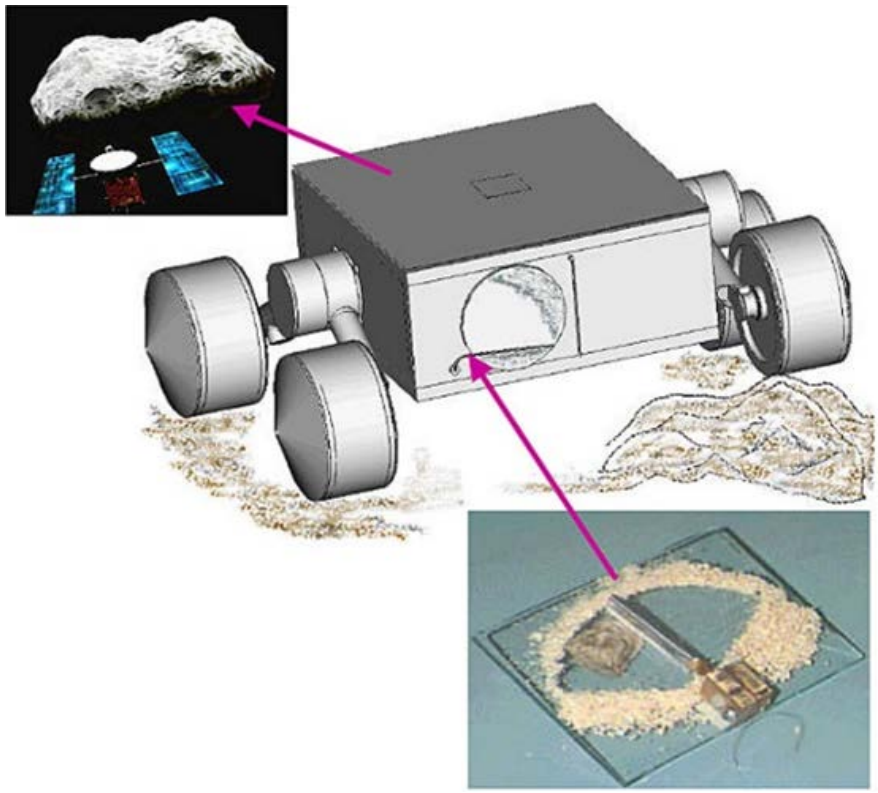

Figure 3.29. MUSES-CN Nanorover EAP Dust Wiper. Y. Bar-Cohen, JPL

3.4.3.6 Dust Removal Tool (Honeybee Robotics)

The Dust Removal Tool (DRT) was designed for the Mars Science Laboratory to expose the natural surfaces of martian rocks obscured by layers of pervasive martian dust. The DRT was integrated with the MSL rover in early 2011 and began a series of successful surface operations shortly after the rover landed at Mars' Gale Crater in August 2012. It has been used frequently to examine areas of potential scientific interest, prior to drilling, analysis with ChemCam, or other contact science.

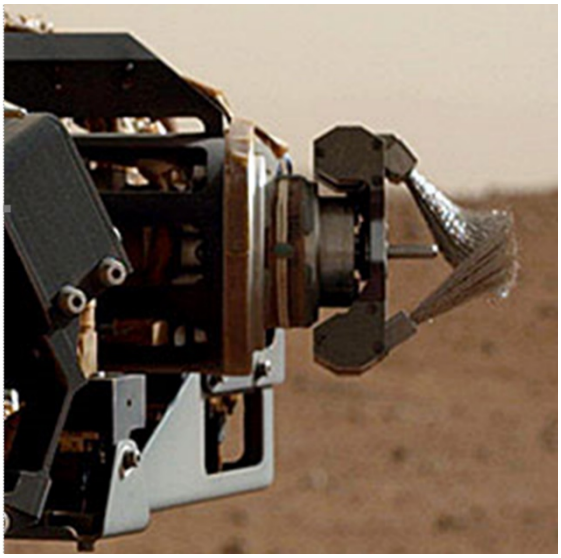

Figure 3.30. Dust Removal Tool (DRT). https://www.honeybeerobotics.com/portfolio/dust-removal-tool

4 The Ring of Power

4.1 Creating Permanently Illuminated Oases

As Wettergreen suggests (Wettergreen 2014), it appears possible to have continuous collective illumination over multiple points; this is the default hypothesis for having a rover chase the sunlight around Shackleton Crater rim area. Indeed, Bussey has shown that collective illumination over two points around SC, lit complementarily, increases illumination from 86% to 94% (Bussey 2010). **Figure 4.1** indeed shows some points are complementary lit, e.g., A1 (89.68°S, 166.0°W) and B1 (89.44°S, 141.8°W) (when one site is dark, the other is often illuminated). Collectively, points A1 and B1 are illuminated for over 8 continuous months, and more than ~94% of the year. This gives basis to finding collective illumination considering multiple points on the rim, looking for complementarity in illumination. In addition, as they reflect to a common region, one seeks proximity of these points to each other. The new idea is to place TFs (reflectors) at these points, one illuminated while others may have dimmed. In this way, increasing the time of continuous illumination becomes possible with TFs at key locations, reflecting the sunlight wherever needed. The reflectors (i.e., TFs, the terms may be used interchanged in this chapter) could raise tens of meters above the ground, where there is increased illumination (Bryant 2009), as exemplified for B1 in **Table 4.1**.

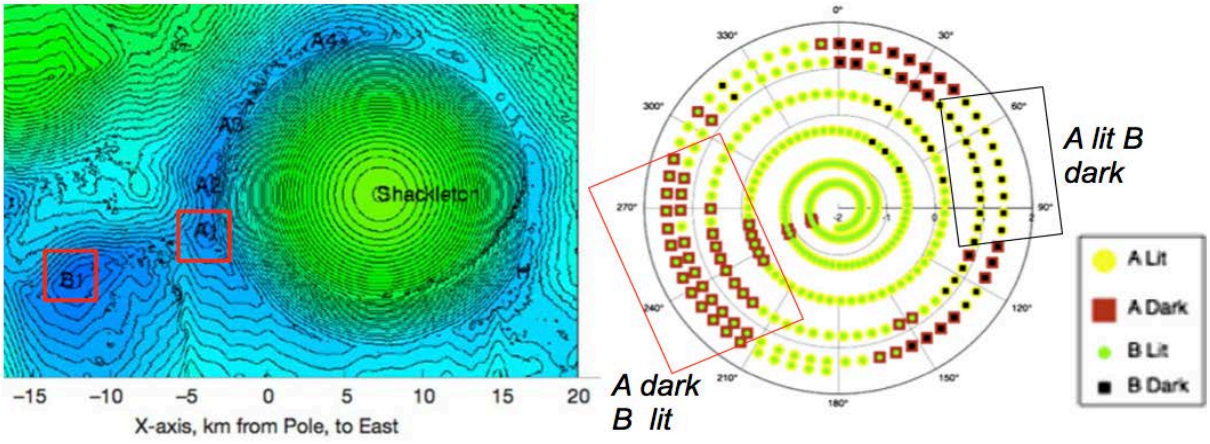

Figure 4.1. Left shows points A1 to A4 and B1 (base sites, (Bryant)); right shows detailed illumination profile for Points A1 and B1 (Bussey, 2010). Collectively Points A and B appear to be lit 94% of the time. Due to solar symmetry only need 6 months of data were plotted, from mid-summer to mid-winter.

Table 4.1. Fragment from Table 1.2 Solar illumination metrics for site B1 tower heights (Bryant, 2009).

Tower Height (m)	Solar Illumination Statistics, Assumed Uniform Distribution Multilayer Average Illumination			Distribution from 2009 to 2028 Multilayer Average Illumination		
	0%	50%	100%	0%	50%	100%
2.0	97.01	94.79	91.67	97.08	94.89	91.99
32	97.60	95.67	92.69	97.71	95.79	93.03
64	97.89	96.15	93.41	97.98	96.27	93.78

This opens, for the first time, the avenue to developing a *Continuous* Solar Power Infrastructure at the south pole.

4.2 The Search for an Optimal Installation of the Power Infrastructure

The focus of the following sections is to identify location combinations near Shackleton Crater that provide near-continuous access to sunlight. *An added constraint is that the resulting reflector placement locations must share line of sight with a surface region, enabling this target surface region ('energy oasis') to have near-continuous access to sunlight year-round.* We analyzed regions both inside and outside the crater; this section is focused mainly on the inside regions where ISRU operations would occur.

In the beginning of the work we attempted to reach illumination 100% of the time during the year. Specifically, we searched for location combinations achieving 100% sunlight in 2020, at any time at least one location seeing the Sun; as tower height would be too high, we reduced the requirement to 99%. The initial analysis, for computational reasons, considered only a limited area, shown in **Figure 4.2**, within a circle of 40 km radius from the south pole, which did not include the heights of Malapert and Leibnitz. These were considered only to the end of the study, and a set of simulations with the extended terrain was performed (presented at the end of the section) with the effect the *illumination numbers decreased by ~1% compared to the initial model.* Not all scenarios and trade-offs were repeated We decided to not adjust down all numbers, as we did not have the exact values, but rather to show the results of the limited model, and give the warning that the numbers did not consider the effect of Malapert, Leibnitz, or lunar eclipses.

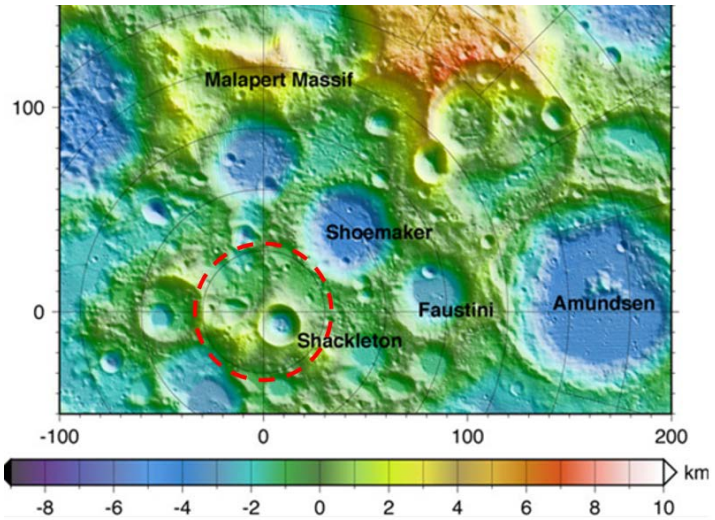

Figure 4.2. Shows the south pole region and, with red line, the delimitation of the area considered in the initial model.

Locations are identified and evaluated using a process involving two illumination simulation and analysis methods and a set-cover algorithm. Results are presented that demonstrate the trade-off between number of locations and height above surface level to achieve near-continuous access to sunlight near Shackleton Crater. The solutions span from three locations 25 meters above surface level to single locations 775–800 meters above surface level.

The workflow developed for the specified optimization task is presented in the following. At high level this involves the following tasks: generate 3D model of south pole region; perform illumination simulation; search region for placement location combination that maximizes combined sunlight availability; determine minimum reflector height required for target (e.g.,

100%, 99%, etc.) sunlight availability; and generate projection coverage map. The specific objective is to determine location sets with near-continuous illumination.

4.3 Illumination Simulation

Illumination data in this work is obtained through simulation using two separate methods: a ray-tracing method and a horizon method. Both methods, however, first require terrain data.

4.3.1 *Terrain Data Generation*

To simulate illumination conditions around Shackleton Crater, a 3-dimensional terrain model is generated for the crater and its surrounding area. The source of terrain data in this work is the Lunar Orbiter Laser Altimeter (LOLA) on the Lunar Reconnaissance Orbiter (LRO), which provides spatial terrain coordinate data with roughly *10-meter horizontal accuracy and 1-meter vertical accuracy* (Riris 2007; Smith et al. 2010; Anthony et al. 2008). To construct a 3D model of the area of interest, approximately 23 million coordinate points (latitude, longitude, radius) are collected, covering all latitudes within 1.5° of the south pole. To facilitate processing, roughly 330,000 of the original 23 million coordinate points are used in the creation of the 3D surface model. This reduction is intended to provide a sufficient balance between the accuracy of the model and the time required to perform the illumination simulation, and the tools developed for this task enable rapid follow-up analysis at higher terrain resolution if desired. The result is a *3D model covering 6,300 square kilometers with a spatial resolution of approximately 40 meters*. Note that this resolution is achievable despite a significant reduction of the raw dataset as a result of the high degree of data concentration in the south pole region due to the polar mapping orbit of the LRO (Vondrak et al. 2010). The raw lat-long-radius data is then converted to a stereographic projection. Because this work makes use of raw LOLA data, some processing is required before obtaining a usable 3D terrain model. Spurious data points, for example, are identified by converting the raw data to a gridded mesh and computing the Laplacian of the surface. The identified spurious data points are then removed from the original raw data, and a 3D STL model is exported. This is illustrated in **Figure 4.3.**

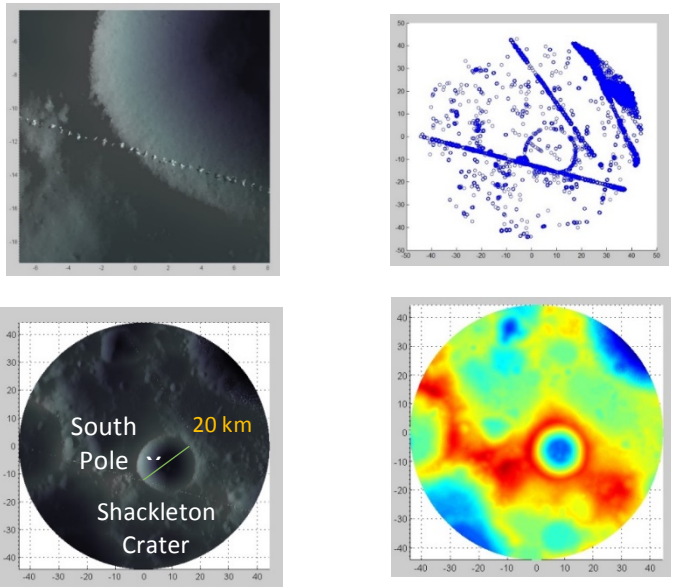

Figure 4.3. LRO LOLA data used to generate 3D model of lunar South Pole region. The top images demonstrate the spurious data identification by converting raw data to a gridded mesh and taking the Laplacian of the surface. The bottom images show the exported STL model from the spurious data points.

4.3.2 *Ray-tracing Method*

The first illumination simulation method, ray-tracing, is implemented to allow for a bird's-eye view assessment of illumination conditions in and around Shackleton Crater. In this method, lines are drawn from a light source to simulate rays of light. Terrain illumination is then determined based on the intersection of these rays with the terrain surface (Glassner 1989). Through this method, it is possible to generate a series of synthetic images, with each image showing the illumination conditions for the area of interest at a given instant in time. This approach served as the basis for several prior illumination studies for this region (Bussey et al. 2010; Bussey et al. 1999; Henrickson & Stoica 2016).

Illumination simulation in this case is performed by generating synthetic imagery using Blender, an open-source 3D computer graphics software product. The created 3D terrain model is imported, and a virtual camera is situated above Shackleton Crater, looking downward. The virtual camera, using an orthographic lens to eliminate perspective distortion, is configured to image roughly 1,600 square km with 960×960 pixels, yielding a spatial resolution of 40 meters. Note that the selection of this camera resolution is driven not only by a trade-off between spatial resolution and required rendering time, but also by the spatial resolution of the 3D surface model itself. That is, using the selected configuration, polygon geometry is not visible in the rendered images.

To simulate incoming sunlight, a lamp object is added to the scene and configured to emit uniform directional rays. Lamp orientation keyframes are then created with the purpose of simulating the changing direction of incoming sunlight in a lunar-fixed reference frame over the course of a year. Keyframes are created using NASA JPL HORIZONS ephemeris data (Giorgini et al. 1998) logged in 6-hr increments for the entirety of 2020, yielding 1,465 frames. Again, the toolset developed for this analysis enables rapid follow-up analysis with higher temporal resolution if desired. For validation purposes, select synthetic images are qualitatively compared with satellite imagery. One such comparison is shown in **Figure 4.4**, in which a synthetic image generated with the developed toolset is shown next to an image taken by the advanced Moon Imaging Experiment (AMIE) on board the ESA SMART-1 spacecraft in similar lighting conditions (Online Resource, ESA). Selection of the year 2020 additionally allows for direct comparison with the previously mentioned Bussey results for quantitative validation (Bussey 2010). For example, the ray-tracing implementation in this work indicates that 89.68°S 163.97°W is illuminated approximately 82.5% of the year. This percentage closely matches the result of 81% found for the same location in the aforementioned Bussey illumination study (Bussey 2010), and matches even better when we apply the ~1% correction indicated by the extended model.

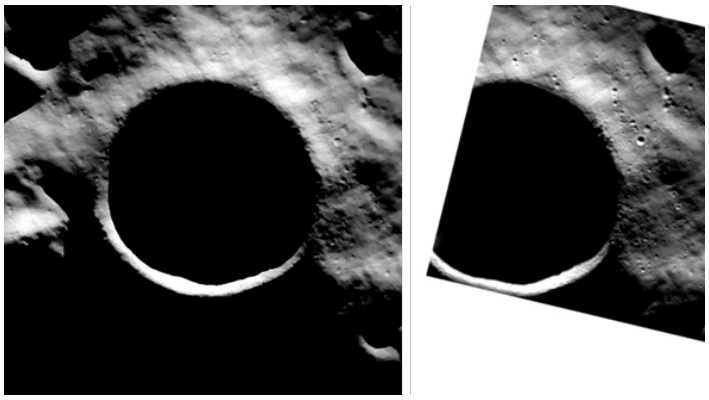

Figure 4.4. Comparison between satellite and generated synthetic imagery of Shackleton Crater, (left) Synthetic, (right) SMART-1.

4.3.3 *Horizon Method*

The second implemented illumination simulation method, the horizon method, takes a ground-based observer approach in assessing illumination conditions. In this method, an observer location is specified, a 360° view of terrain elevation at the observer location is generated, and this terrain elevation data is then compared with the known path of the Sun (see **Figure 4.5**). Whereas the *raytracing method* shows illumination conditions *over a region at a given instant in time*, the *horizon method* shows illumination conditions for *one specific location over some period of time.* The horizon method is less frequently used in the literature, but it was used in a recent study by Gläser focused on assessing illumination conditions at the lunar south pole (Gläser et al. 2014).

Given the location of an observer (x_o,y_o,z_o), and the location of a terrain coordinate point (x_t,y_t,z_t), the relative azimuth

(ϕ) and elevation (θ) of the terrain location can be found with

$$dx = x_o - x_t,\ dy = y_o - y_t,\ dz = z_o - z_t$$
$$d = (dx^2 + dy^2)^{1/2},\ \phi = tan^{-1}(dx/dy)$$
$$\theta = tan^{-1}(dz/d)$$

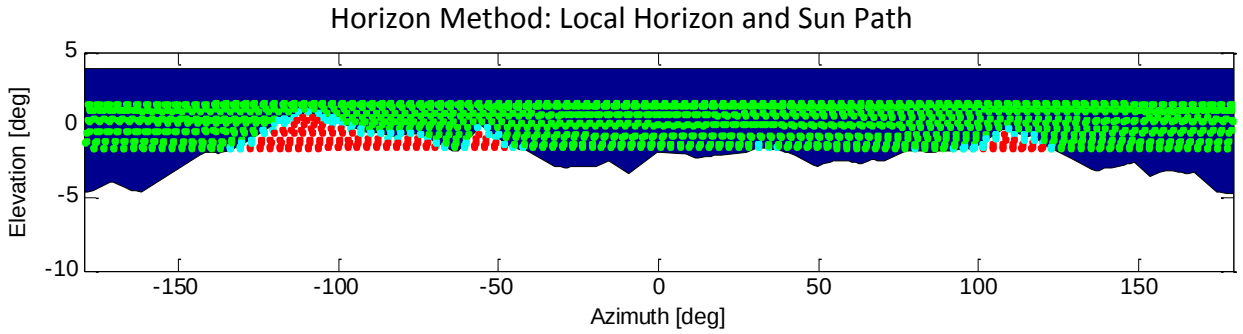

Figure 4.5. Horizontal method plot. This is generated by plotting the local horizon at a given location and comparing that with the path of the Sun. Green indicates that the solar disk is fully visible. Yellow indicates partial visibility; and red indicates no visibility.

Once azimuth and elevation values are found for every terrain surface coordinate, the horizon elevation can be approximated by subdividing 360° into small angular arcs ($\Delta\phi$) and identifying the maximum elevation value within each arc. This process is illustrated in **Figure 4.6**.

For validation purposes, results obtained with this work's implementation of the horizon method are compared with those reported in the mentioned Gläser study at specific locations. This comparison is shown in **Table 4.2**. As can be seen, the two implementations are in close agreement with one another.

4.3.4 *Search Process*

The two implemented illumination simulation methods each have strengths and weaknesses. Ray-tracing can generate illumination data for large regions, but it is essentially limited to assessing lighting conditions at ground level. (The method used in Henrickson & Stoica 2016 for

assessing illumination conditions 100 meters above ground level can only be used as a rough low-end estimate, as it consistently yields false negatives when the Sun azimuth is negative.)

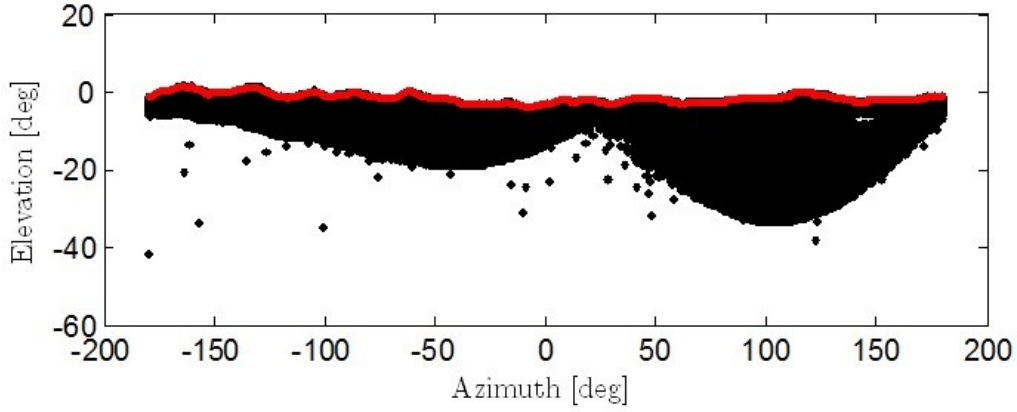

Figure 4.6. Terrain surface panorama view generated 20 meters above surface level at 89.8499°S 151.7244°W. Computed horizon line highlighted in red.

Table 4.2. Annual Illumination Percentages: Horizon Method Results Compared with Gläser 2014 Results.

Location	Height	Gläser 2014¨	Henrickson& Stoica 2016
89.6871°S 197.2887°E	0 m	81.3%	80.8%
89.6856°S 196.7626°E	0 m	76.2%	78.8%
89.4516°S 222.7581°E	10 m	92.6%	92.6%
89.4544°S 222.8445°E	10 m	91.9%	93.1%

The horizon method is capable of performing vertical positioning sunlight availability analysis, but it can only do so for one position at a time. To identify reflector placement locations, *a search process is developed that leverages the strengths of these two methods.* At a high level, this process uses the ray-tracing method to identify candidate placement location combinations. For each candidate combination, the horizon method is used to incrementally increase the height of the reflectors until the collective annual illumination percentage reaches 99% (those solution may in fact provide ~98% when Malapert would be included). From here, redundant reflectors are eliminated, and projection coverage is assessed. Placement combination solutions are then stored for batch evaluation, allowing for identification of optimal solutions.

4.3.5 *Ray Tracing vs. Horizon Method: Cross-Verification*

Before proceeding to the location combination search, a final cross-verification is performed by comparing the combined annual illumination percentages for various sets of points using the two methods. One set of locations (found with the developed search method) is shown here, demonstrating that the two methods closely agree when considering both visibility of the center of the Sun and the upper edge of the Sun. This shows that the two illumination methods not only agree with similar published implementations, but that they additionally agree with one another.

In performing this analysis, various visualization functions were written to facilitate analysis. **Figure 4.7**, for instance, plots Sun locations relative to each of three location horizons when the Sun is not visible to any of the locations.

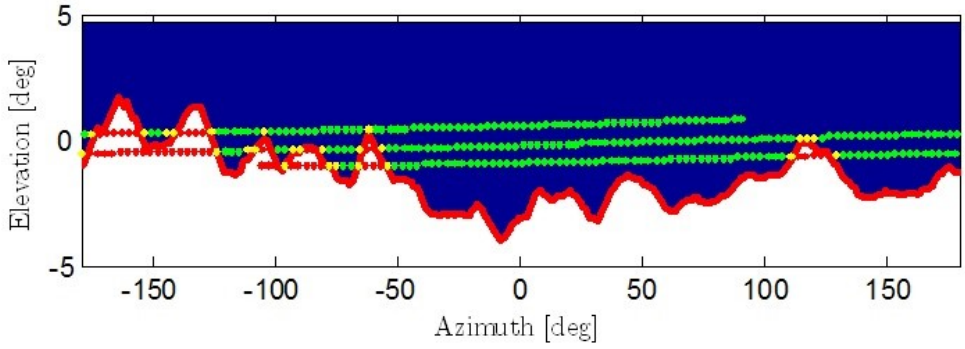

Figure 4.7. Portion of 2020 Sun path relative to local horizon (red line) viewed from 20 meters above surface level at 89.8499°S 151.7244°W. Green indicates that the solar disk is fully visible. Yellow indicates partial visibility; and red indicates no visibility.

Percentage of Year Center of Sun is Visible

Set of Locations	Ray-Tracing	Horizon
89.6872°S, 196.9855°E	98.6%	98.4%
89.4626°S, 224.7396°E		
89.3848°S, 217.9394°E		

Percentage of Year Upper Edge of Sun is Visible

Set of Locations	Ray-Tracing	Horizon
89.6872°S, 196.9855°E	99.5%	99.2%
89.4626°S, 224.7396°E		
89.3848°S, 217.9394°E		

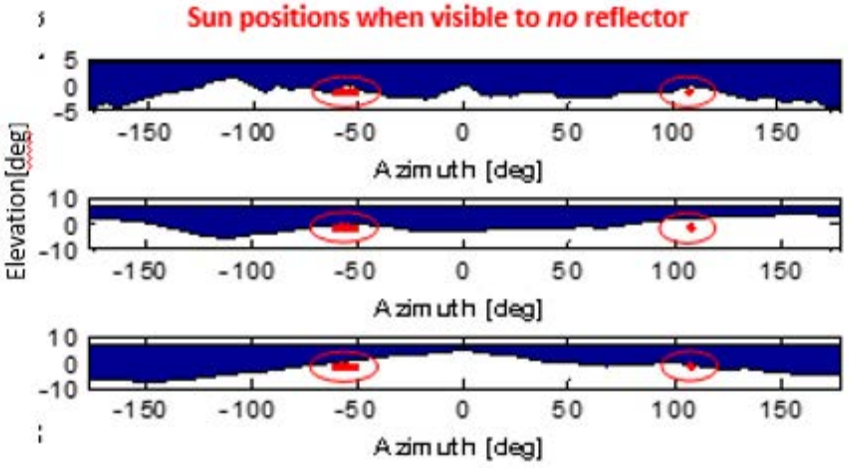

Figure 4.8. Sun locations relative to each of three location horizons when the Sun is not visible to any of the locations.

4.3.6 *Reflector Placement Search Process*

At a high level, the search process involves first identifying ground-level location combinations using the synthetic imagery generated with the ray-tracing method, and subsequently raising these location heights above ground level using the horizon method until the combined annual illumination of the location set reaches the target %, e.g., 99% or 100%. This process starts out with what is essentially a greedy set-cover algorithm. The goal here is to determine the number of locations that are required in a specified region to collectively equal the

max possible annual illumination percentage within that region. That is, if at least one part of the region is illuminated 95% of the year, the task is to determine the number of locations that are required to ensure that at least one location in the set has access to sunlight 95% of the year.

The set-cover algorithm works as follows: first, a point (Point 1) within the search region is selected. In this case, the point is randomly selected from a list of the *n* points that receive the most annual illumination. (The assumption here is that combinations with high annual illumination percentages will typically contain at least one point that is illuminated more than is average for the region. This is largely done to reduce computation time.) The location with max illumination percentage while Point 1 is dark is then identified. Following this, the location with max illumination while Points 1 and 2 are dark is found. This is repeated until the combined annual illumination percentage of the set either reaches 100%, or until there are no additional locations in the region that would improve the set's combined annual illumination percentage (**Figure 4.9**). This process is repeated *n* times, generating *n* sets of various numbers of locations. Please note that this process does not necessarily give the global optimum solution.

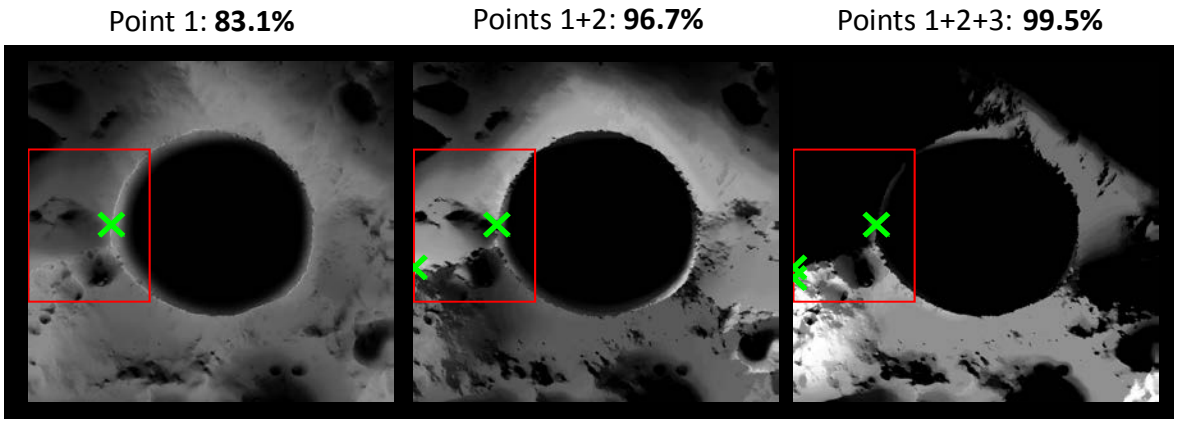

Figure 4.9. Illustration of the set-cover algorithm. The red box denotes the region of interest (identified locations are constrained to this box). Point 1 is shown in the left-most image (a stacked image including all 1,465 synthetic images); it is illuminated 83% of the year. The middle image shows the result of stacking and normalizing all images in which Point 1 is not illuminated. The point of max illumination in this set is identified, and the combined set illumination percentage increases to almost 97%. A third location is found using this process, which increases the annual illumination to 99.5%, and so on.

As mentioned, the second step of the search process is to then take the sets of locations found at ground level and increase their heights above ground level until target illumination is achieved. **Table 4.3** shows four locations at ground level with 99.2% annual illumination. Incrementally increasing the height above ground level raises this to 100% at 100 meters above ground level. **Figure 4.10** shows the local horizon at ground level and 75 m above ground level for these four locations; Sun positions are plotted for times in which only a single location in the set has access to sunlight.

It is evident when looking at the 75 m AGL figure (**Figure 4.10**) that, at this height, there are no times in which the first location is the only location in the set that can see the Sun. This means that this location has become redundant for this height. Removing this location from the set will not decrease the combined illumination percentage of the set at this height. This process of identifying location redundancy and removing the location from the set is crucial in generating minimum height/minimum reflector solution sets for continuous annual sunlight availability.

Table 4.3. Implementation of step 2 using the horizon method. Here the reflector heights are found to achieve 100% of the combined annual sunlight availability (in reality ~99% due to shadows from Malapert and Leibnitz and lunar eclipses).

Locations	0 m	50 m	75 m	100 m
89.6872°S, 196.9855°E	99.2%	99.7%	99.9%	100%
89.4626°S, 224.7396°E				
89.3848°S, 217.9394°E				
89.7794°S, 203.6978°E				

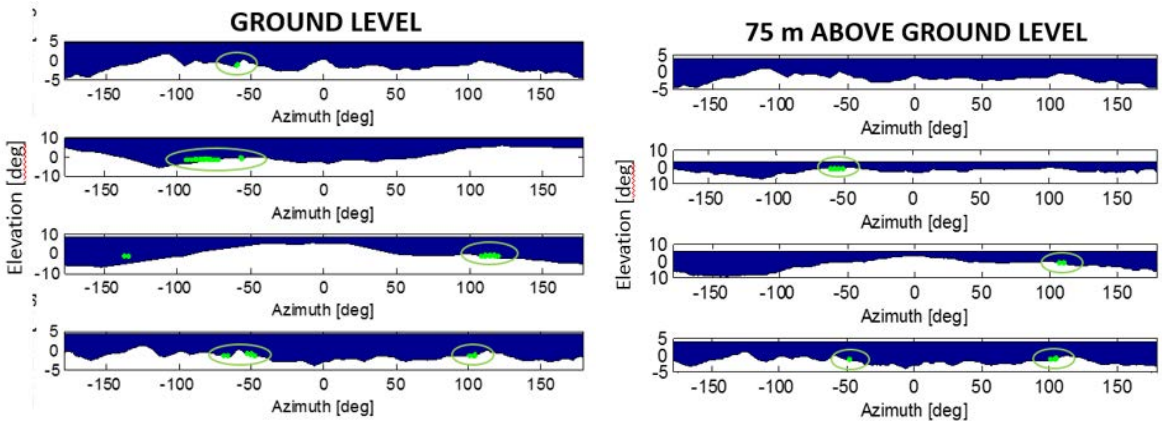

Figure 4.10. Sun position when visible to reflectors at ground level (left) and 75 m above ground level (right). This illustrates that increasing reflector height can yield redundant reflectors.

As reflector height above ground level is increased for a given combination, some of the reflector locations may become redundant. That is, removing one or more of the reflectors may not reduce the collective annual illumination percentage. Redundant reflectors in a given location set are identified by evaluating the illumination time histories for each individual reflector in the set. For each reflector, times are identified in which the selected reflector has exclusive line of sight with the Sun. If a single reflector never has exclusive line of sight with the Sun throughout the year, it is redundant. If multiple reflectors are redundant in this way, they are sequentially removed from the set in order of decreasing distance from the "center" of the location set.

4.3.7 *Identify Location Combination Candidates*

As described, the implemented ray-tracing method is used to identify candidate reflector placement combinations. Previous work done in this area (described in Henrickson & Stoica 2016) made use of a recursive grid search to assess location combinations within a region. Our more recent work significantly improved search performance by instead using a greedy set cover algorithm (Slavík 1996). In the implemented search algorithm, a number of pixels are first selected within a given region. In this case, these pixels are selected randomly out of a set of the n most illuminated pixels. For example, in a 200 × 200 pixel search region (40,000 pixels total), the 1,000 most illuminated pixels are identified, and 100 of those are then selected at starting points for placement combinations. For each of the selected initial pixels (Point 1), the location with maximum illumination while Point 1 is dark is found (Point 2). The location with maximum illumination while Points 1 and 2 are both dark is then found, and so on, until the annual

illumination of the set either reaches 100% or remains constant with additional locations added to the set.

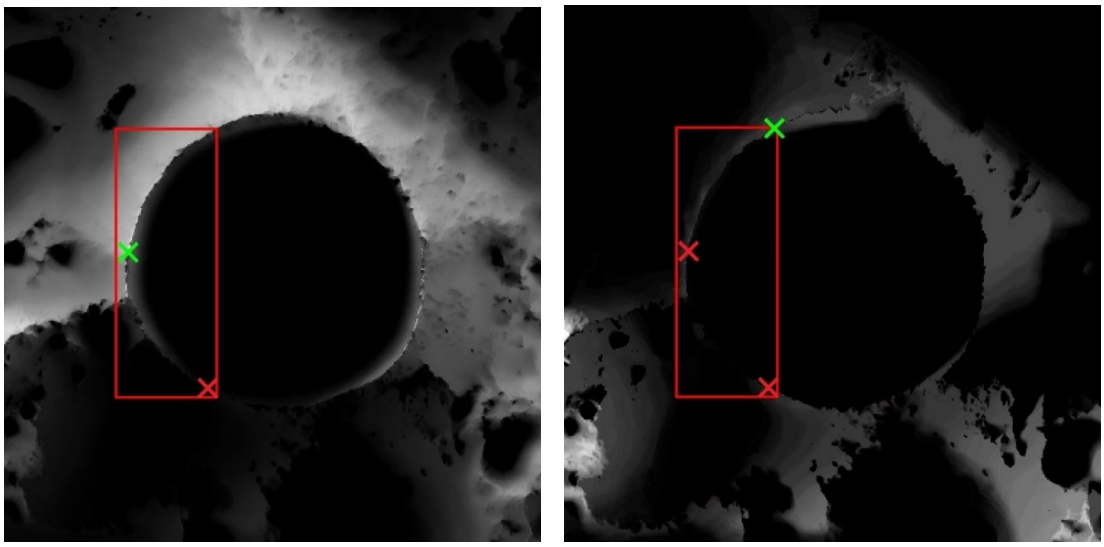

Figure 4.11. Annual illumination map only including times in which Point 1 (in red) does not have access to sunlight. Point 2 (in green) is the location of maximum annual illumination within the search area (outlined in red). The annual illumination map only includes times in which Points 1 and 2 (both in red) do not have access to sunlight. Point 3 (in green) is the resulting location of maximum annual illumination within search region (outlined in red).

The search algorithm implemented in this work is several orders of magnitude faster than the recursive grid algorithm described in Henrickson & Stoica (2016), enabling dramatically more rapid assessment of large search regions and allowing for consideration of 10 or more reflectors. To illustrate, Henrickson & Stoica (2016) cite an example scenario involving placing three reflectors in a 10,000 pixel region—an original search space of 166 billion combinations is reduced to 41 million combinations through use of the recursive grid algorithm. Using the set cover algorithm implemented in this work, the same initial search space of 166 billion combinations is effectively reduced to 30,000, since the algorithm is simply identifying the point of max illumination within the search region once per reflector. This represents a roughly 1,000× decrease in required computation time relative to the recursive grid algorithm.

4.3.8 *Increase Height until Target Illumination Level is Reached*

The candidate placement location combinations found using the described set-cover algorithm are based on the synthetic imagery generated using the ray-tracing method that describes illumination conditions at ground level. Location combinations that do not achieve the target annual illumination, 99% in the initial case at ground level are incrementally raised above ground level and analyzed using the horizon method until the combination reaches 99% annual illumination. The height required to achieve 99% illumination is then logged, allowing for later evaluation of the solution space.

4.3.9 *Assess Projection Coverage*

Recalling the motivation of this work—using solar reflectors to project near-continuous sunlight to an "energy oasis"—the projection coverage of each identified location set must be evaluated. The energy oasis in this case is the region of terrain that is visible to all reflectors in a given set. The location and size of the energy oasis is unique to each reflector placement set.

Projection coverage for each placement combination is performed, through the use of Blender, by sequentially placing an omnidirectional lamp at each reflector position and rendering an image that gives a map of all ground regions that are visible to that location. This is done sequentially for each reflector position in the combination, yielding one line-of-sight (LOS) coverage map for each reflector. **Figure 4.12(a)** gives an example LOS map for a reflector placed 300 meters above the surface level at a location on the rim of Shackleton Crater. Note that, due to the slope of the crater, this reflector is incapable of redirecting sunlight to a region directly downslope from its position. This is typical of reflectors placed at the peak of the crater's rim. This dead-zone effect can be mitigated through the use of multiple reflectors. **Figure 4.12(b)**, for instance, shows the resulting combined LOS map when an additional reflector is considered.

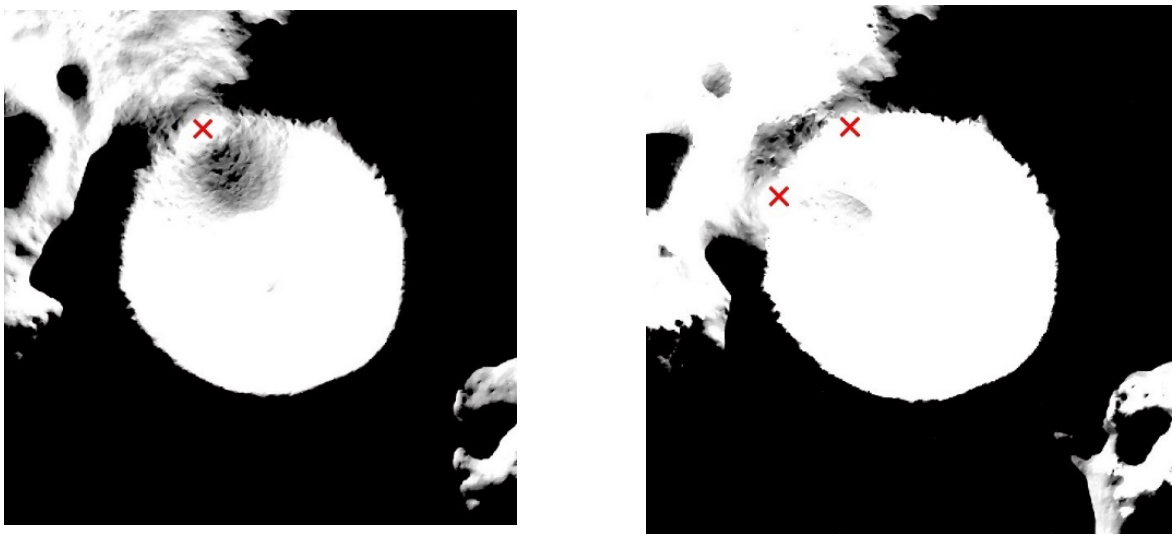

Figure 4.12. (a) White region indicates line of sight for reflector placed 300 meters above surface level (placed where the red x is). (b) *Combined* line of sight maps for two reflectors (marked in red) placed 300 meters above surface level. Points in white would have direct line of sight to at least one of the two reflectors. There are no gray points but there are regions with mixtures of white points and black points

Although there is no drop-off due to atmospheric scattering in the lunar environment when "retransmitting" sunlight in this fashion, there is a drop-off that must be accounted for in modeling sunlight projection coverage. An observer on the lunar surface viewing a solar reflector receives the full amount of available of solar flux as long as the full solar disk can be seen via the reflector. If only a portion of the solar disk is visible, however, the observer only receives the corresponding percentage of the solar flux. The sunlight projection drop-off for a given reflector is therefore found by computing the apparent size of the reflector at a given location and comparing with the apparent size of the solar disk. This provides an upper threshold for the amount of sunlight that a given ground location would receive when redirected from a specified reflector size and location.

Based on results presented in the TransFormers Phase I NIAC study (Stoica et al. 2014), the reflectors in this work are modeled as being circular and 40 meter in diameter. The apparent angular diameter of the mirror can then be computed for every terrain coordinate point and compared with the angular diameter of the Sun to determine projection coverage drop-off.

The resulting sunlight projection coverage map including this drop-off effect for the two reflector locations shown in **Figure 4.13(a)**. In this figure, pixels values range from 0 (black) to 100 (white), representing the percentage of the solar disk that would be visible at each location in either of the reflectors. This representation shows the region in which sunlight can be projected for at least a period of the year.

To ensure near-continuous access to sunlight, however, a true energy oasis must be visible to every reflector in the system. **Figure 4.13(b)**, therefore, shows the energy oasis region corresponding to the sunlight projection region shown. In this figure, pixel values are again scaled from 0 (black) to 100 (white), representing the minimum percentage of solar disk that can be seen via reflector continuously throughout the year.

Note that this work approximates the Sun as having constant angular diameter throughout 2020. Additionally, changes in apparent reflector angular diameter based on the attitude of the mirror are not modeled—the reflectors are assumed to be capable of projecting sunlight in any direction, and further development of the reflector system is necessary before further analysis of this specific nature is warranted.

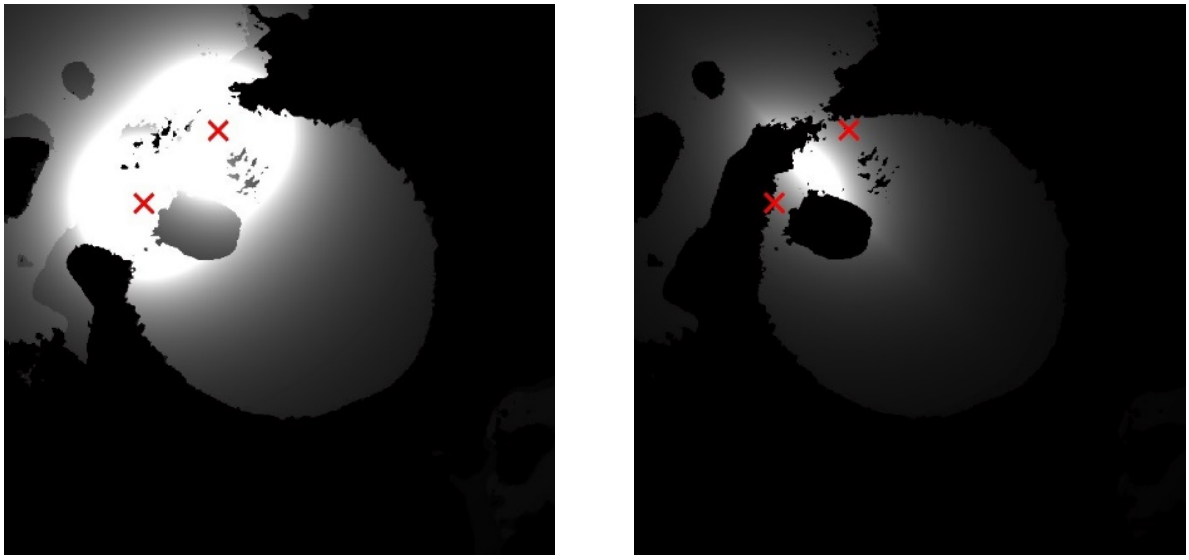

Figure 4.13. (a) Sunlight projection coverage map including distance-based drop-off for two-reflector system with reflectors placed 300 meters above ground level (marked in red). This represents the region in which sunlight can be projected at least part-time in the year 2020. (b) Energy oasis region (ground region visible to all reflectors) corresponding to sunlight projection coverage map. This represents the region in which sunlight can be projected near-cont*inuously* throughout the entirety of the year 2020.

Even when assuming an omnidirectional redirection capability, these coverage projection maps are time-dependent. Although the combined annual illumination percentage of the set is ~99%, each reflector goes through periods of complete and partial darkness, which affects its projection capability. **Figure 4.14** shows snapshots from an animation demonstrating this for three reflectors placed on and to the west of the rim of Shackleton Crater. The left plot shows the natural sunlight availability, and the right plot shows potential sunlight availability in the presence of the reflectors (installed 100 m above surface level). Note that there are periods in which one or two of the reflectors go dark.

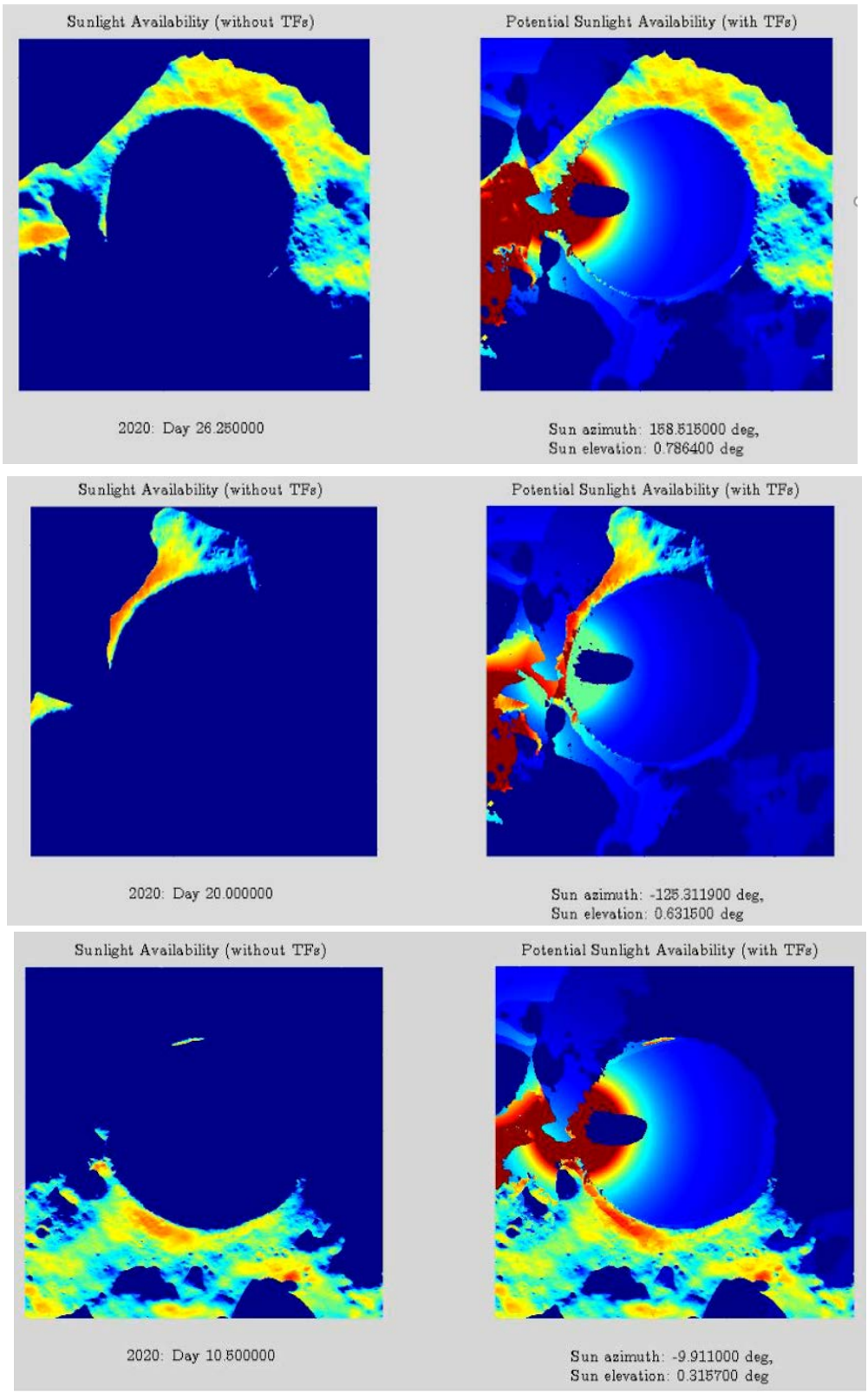

Figure 4.14. Snapshots from an animation of sunlight availability without (left) and with reflectors (right). Reflector projection coverage represents potential sunlight availability. It does not mean that the entire area is illuminated at once. The reflectors are likely only able to project to one area at a time. Reflector projection area intensity scales with percentage of sun visible.

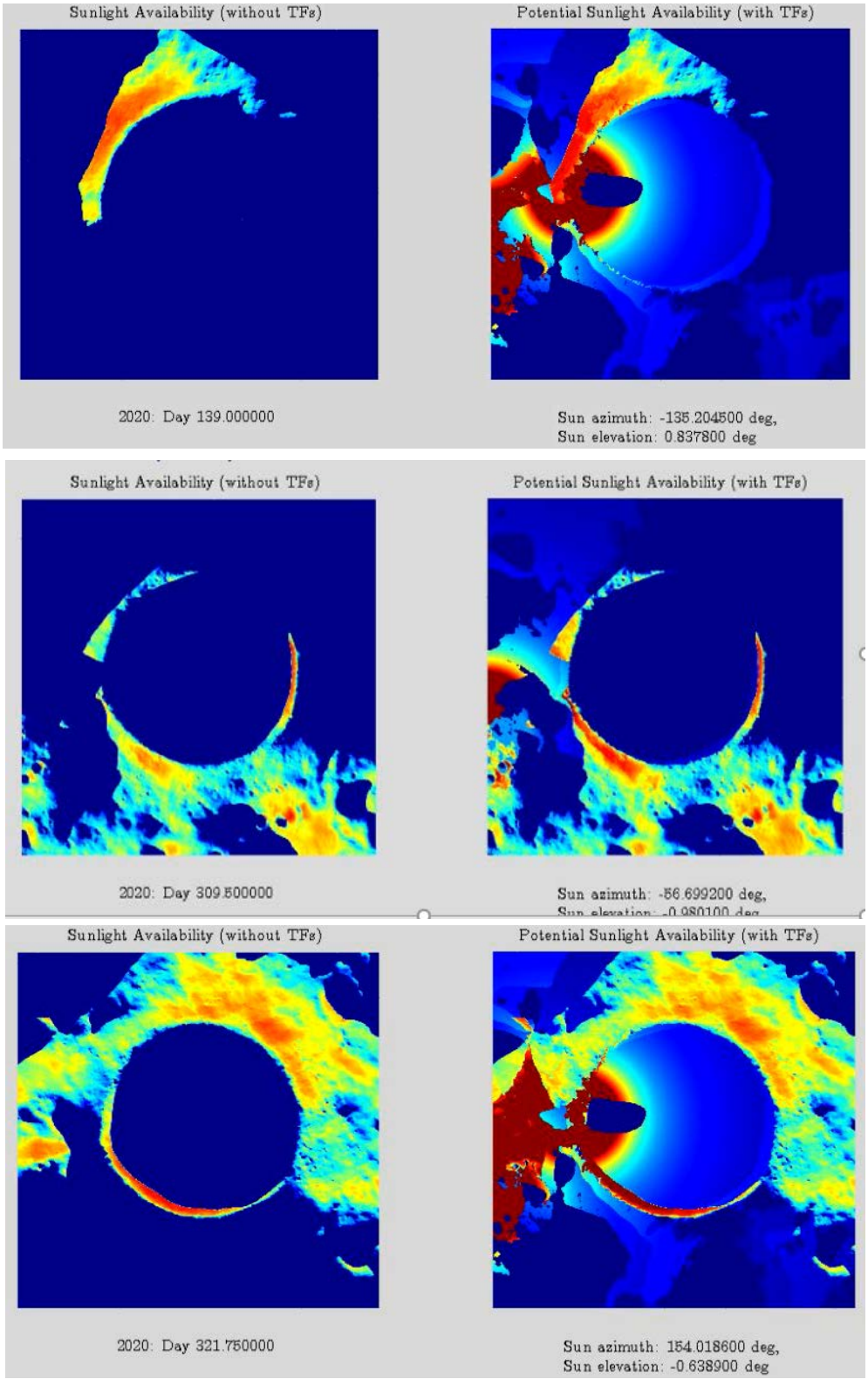

Figure 4.15. Snapshots from animation of sunlight availability. The frames on the right represent areas that could be illuminated by reflectors, i.e., potential sunlight availability. The reflectors are likely only able to project to one area at a time. Reflector projection area intensity scales with percentage of sun visible.

One should emphasize that the right-most subplots in **Figure 4.15** indicate *potential* sunlight availability. The reflectors are assumed to be able to redirect sunlight in any direction here, but they can still only redirect to one location at a time. This will drive some additional analysis.

Before moving forward one need to show a reflectance effect from the illuminated on the rim to points inside the crater. **Figure 4.16** shows the results of a simulation, in which points inside SC receive photons from the illuminated rim itself, not from TFs. **Figure 4.17** shows an elevation map of the crater.

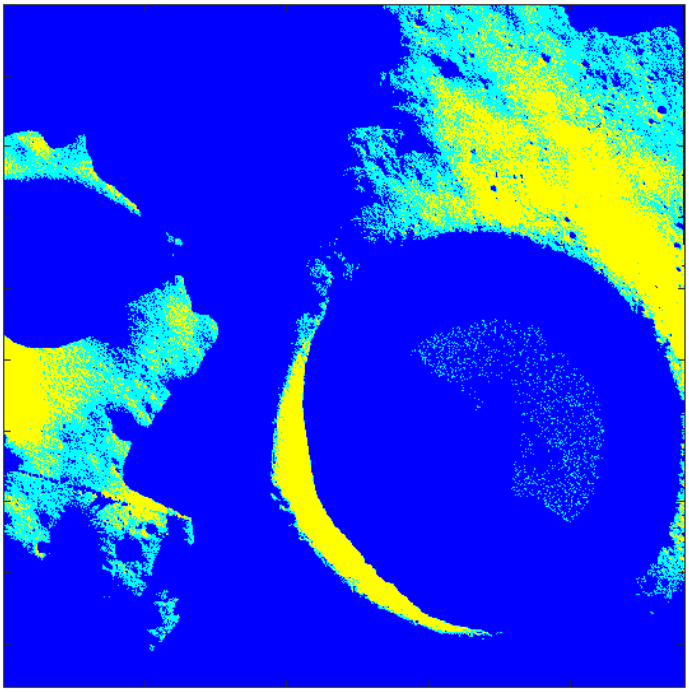

Figure 4.16. Illumination simulation detail showing the reflectance effect inside the crater – jet colors (Work by Giuseppe Governale during an internship at JPL in Stoica's lab).

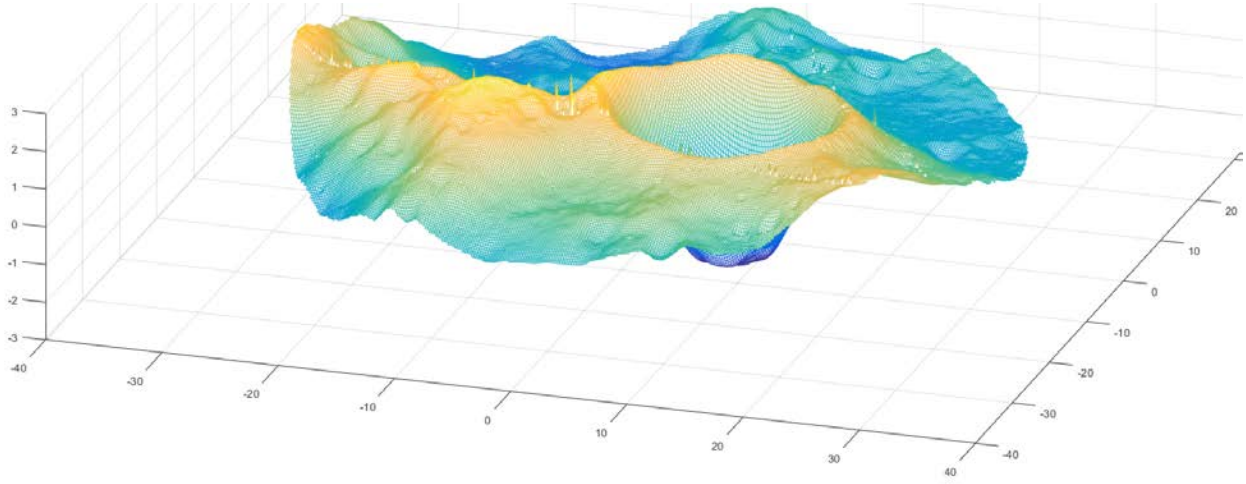

Figure 4.17. Elevation map of the imported coordinate points. (Work by Giuseppe Governale during an internship at JPL in Stoica's lab).

4.4 Results and Trade-offs

The developed search process finds solar reflector position combinations in which at least one reflector has access to sunlight throughout 99% of the year (in this specific case, the year 2020). It is important to note that every solution presented here achieves 99% annual illumination—the remaining task is to identify the best solution. Evaluating solutions relative to one another, however, is contingent on cost and performance factors related to the mission concept that have not yet been finalized. For this reason, results presented here do not necessarily attempt to definitively identify the best reflector placement combination; rather, results are given to illustrate the trade-off between reflector height and number of reflectors when considering placement in the vicinity of Shackleton Crater.

In this section, a summary of solutions is first given, focused on the trade-off between number of reflectors and required placement height. Following this, specific placement combinations on the rim of Shackleton Crater are detailed, and solutions focused on the ridge west of the crater are discussed.

4.4.1 *Number of Reflectors vs. Height*

Table 4.4 shows the required reflector height necessary to achieve 99% annual sunlight availability for sets of *n* reflectors placed around the rim of Shackleton Crater. These results represent the minimum height with fewest reflector solutions for a search that evaluated thousands of placement combinations involving up to 10 reflectors placed around Shackleton Crater. Note that although combinations of up to 10 reflectors were considered, solutions involving more than three or four reflectors are rare because locations quickly become redundant as their height above ground level is increased.

The presented results match intuition in the sense that increasing reflector height reduces the number of reflectors required to ensure that at least one reflector has access to sunlight year-round. The solution involving four reflectors is included to illustrate that increasing the number of reflectors beyond three does not reduce the required reflector height to achieve 99% sunlight availability for the search area focused on the rim of Shackleton Crater. This indicates that, based on the results found to date, any near-continuous solar power solution strictly on the rim of Shackleton Crater will require at least one location at a height of 300 meters above surface level.

Table 4.4. Required height for *n* reflectors placed on rim of Shackleton Crater to achieve 99% annual sunlight availability.

Number of Reflectors	Reflector Height [m]
1	775
2	450
3	300
4	300

4.4.2 *Single-Reflector*

Because the Sun is always within roughly 1.5° of the horizon at the lunar poles, we intuitively expect that a location with sufficient height above surface level should be able to achieve near-continuous annual access to sunlight. Two such solutions are found here for locations on the rim of Shackleton Crater. For both solutions, the required height is roughly 775 meters—this is the minimum height found to date for a single-reflector, near-continuous solar power solution.

Figure 4.18 shows the placement location and corresponding energy oasis map for a reflector placed 775 meters above ground level at 89.7841°S 156.2906°W. Recall that the energy oasis is the region in which the reflector system can guarantee near-continuous projected solar energy throughout the year 2020. **Figure 4.19** shows location and corresponding oasis map for one reflector placed 775 meters above surface level at 89.8522°S 151.2430°W. Note that the sunlight projection fall-off shown in each oasis map here is based on a 40-meter diameter reflector.

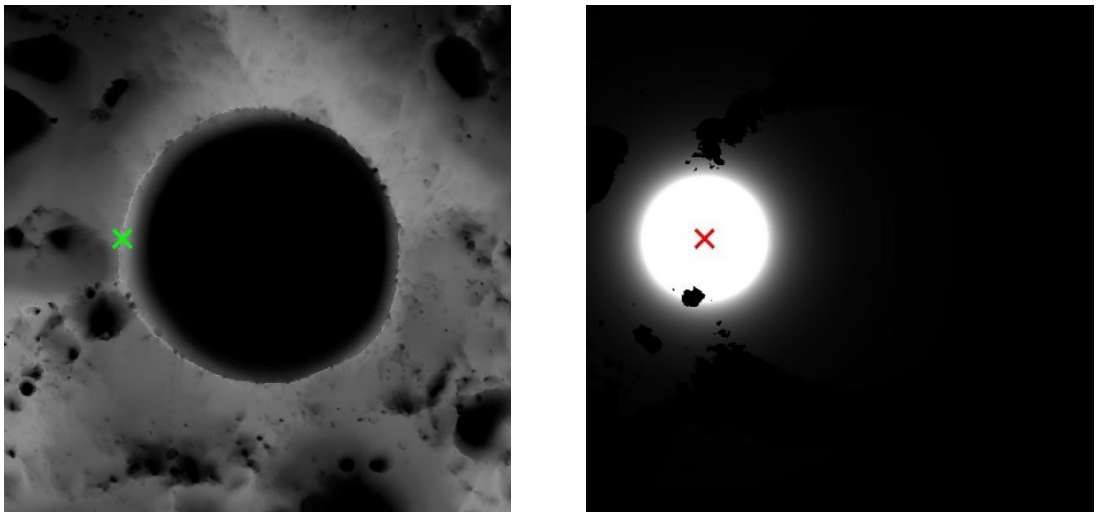

Figure 4.18. Location (left) and corresponding oasis map (right) for single reflector placed 775 meters above ground level at 89.7841°S 156.2906°W.

Figure 4.20 shows the relationship between height and annual illumination percentage for a reflector. From this, it is apparent that, although a single reflector requires a placement height of nearly 800 meters to reach 99% annual illumination, 98% annual illumination could be achieved with a reflector placed at nearly half this height. This work, targeting 99% annual illumination solutions, focuses on results accordingly; however, this result indicates that the difference between 99% and 98% solutions may dramatically affect practical feasibility.

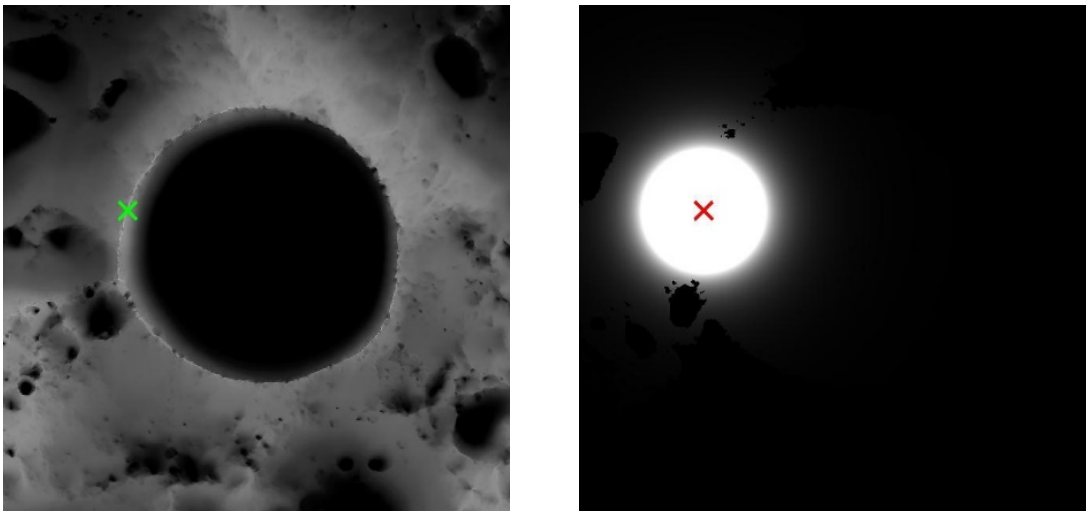

Figure 4.19. Location (left) and corresponding oasis map (right) for single reflector placed 775 meters above ground level at 89.8522°S 151.2430°W.

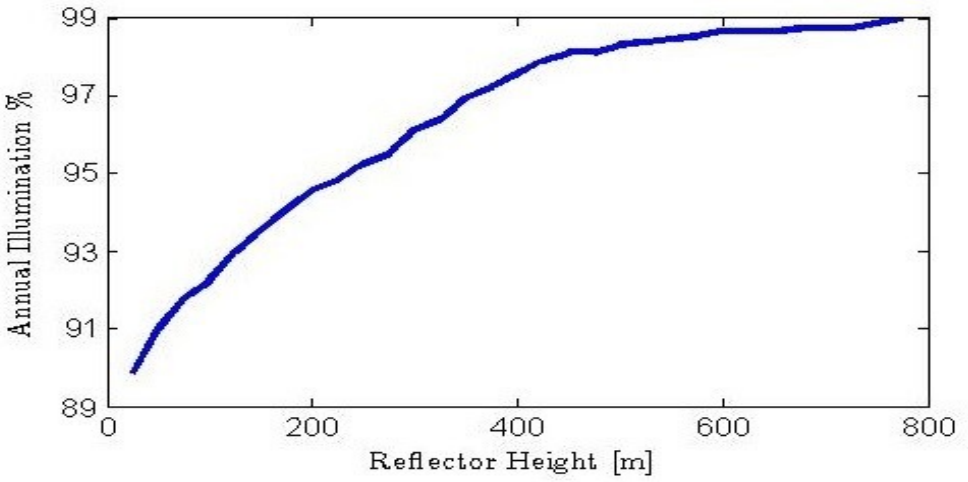

Figure 4.20. Annual illumination percentage vs. height for reflector placed at location shown in Figure 4.18.

4.4.3 *An Infrastructure with Two Reflectors*

In scenarios involving multiple locations, no single reflector needs continuous access to sunlight; rather, at nearly all times, a single location in the set needs access to sunlight. Because individual reflectors do not require continuous sunlight, using multiple locations reduces the required height of each reflector. **Figure 4.21** and **Figure 4.22** show solutions involving two reflectors placed 450 meters above surface level. Increasing the number of reflectors from one to two therefore decreases the required placement height from 775 meters to 450 meters. Note that the effective size of the resulting energy oasis, however, decreases in size when considering two reflectors. This is in part simply due to the fact that reflectors at lower heights have line of sight with smaller terrain regions. Additionally, the energy oasis is in a sense limited by its weakest link—that is, since the energy oasis map shows the maximum amount of projected sunlight that can be continuously guaranteed to a given location, it is limited by the most distant reflector. The usable size of a resulting energy oasis region for cases involving multiple reflectors is therefore driven by both the height of the reflectors and the distances between them. Decreasing reflector height decreases oasis size, and decreasing distance between reflectors increases oasis size. Finally, **Figure 4.23** shows collective illumination percentage vs. reflector height for the placement combination shown. It is evident from this that 98% annual illumination could be achieved with two reflectors placed roughly 450 meters above surface level.

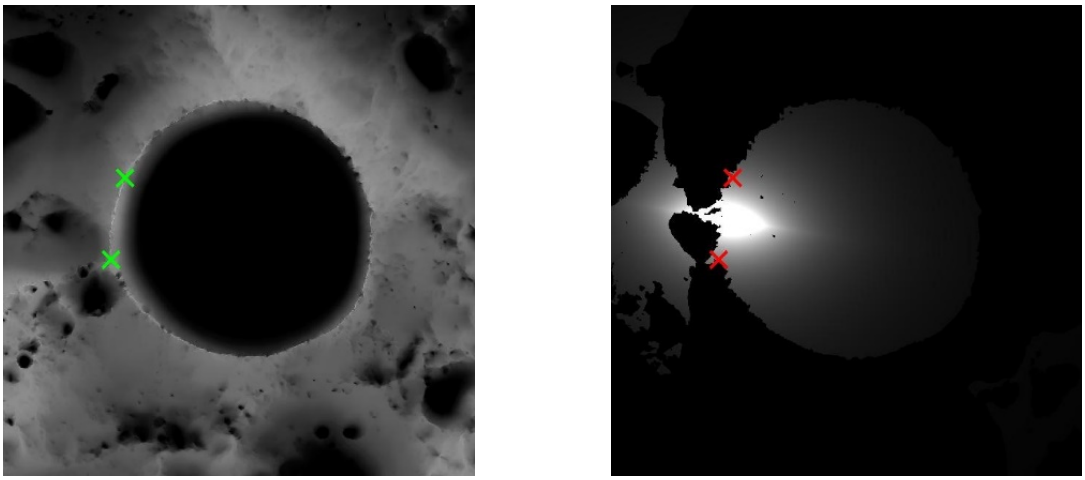

Figure 4.21. Location (left) and corresponding (right) oasis map for two reflectors placed 450 meters above ground level at 89.9029°S 145.2301°W and 89.6876°S 162.8645°W.

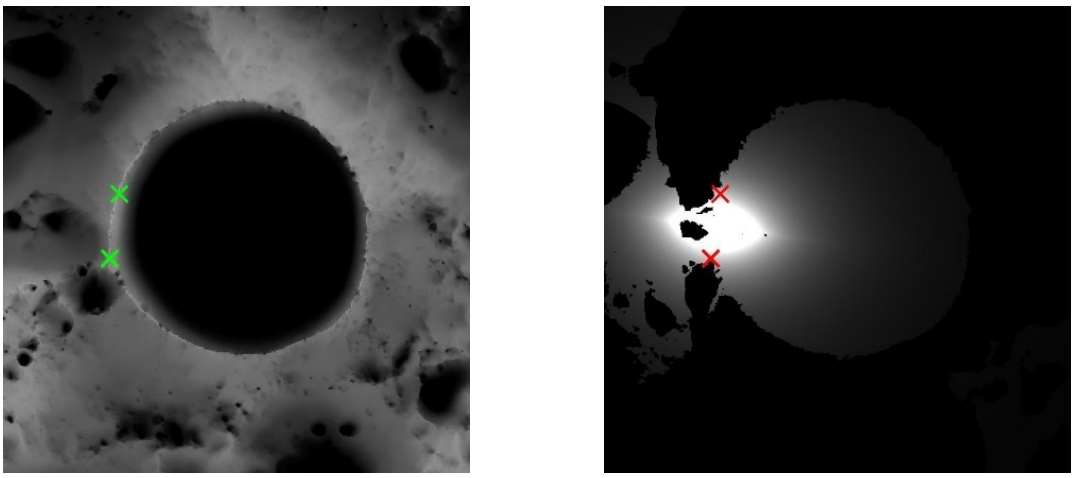

Figure 4.22. Location (left) and corresponding oasis map (right) for two reflectors placed 450 meters above ground level at 89.8587°S 151.6178°W and 89.6876°S 162.8645°W.

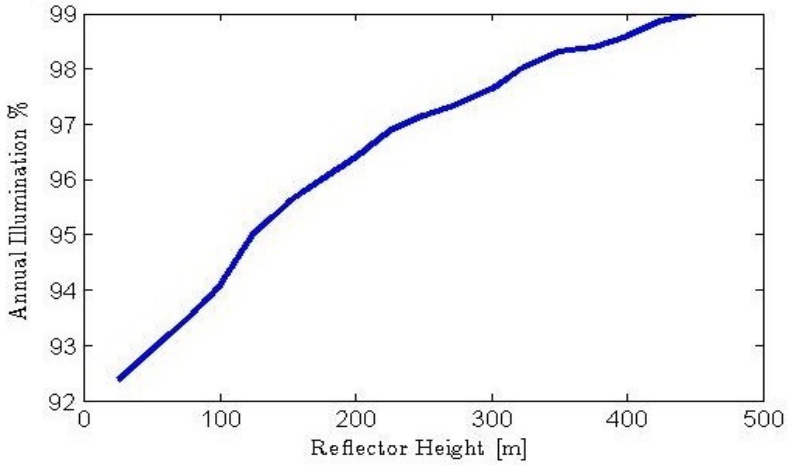

Figure 4.23. Annual illumination percentage vs. height for reflectors placed at locations.

4.4.4 *An Infrastructure with Three Reflectors*

Solutions involving three reflectors have been found, however, for these solutions, distances between reflectors become inhibitive with regard to creating an easily usable energy oasis. **Figure 4.24** shows the locations and corresponding oasis map for a set of three reflectors placed 300 meters above surface level. As expected, increasing the set from two to three reflectors reduces the required placement height (from 450 to 300 meters), but the increased distances between the locations reduces the percentage of solar flux that can be guaranteed continuously within the resulting energy oasis. Implementation of such a solution would therefore likely require increasing the size of the reflectors beyond 40 meters in diameter. **Figure 4.25** shows how collective illumination percentage increases with reflector height for this placement combination. It is apparent that 99% annual illumination can be achieved with reflectors placed approximately 300 meters above surface level.

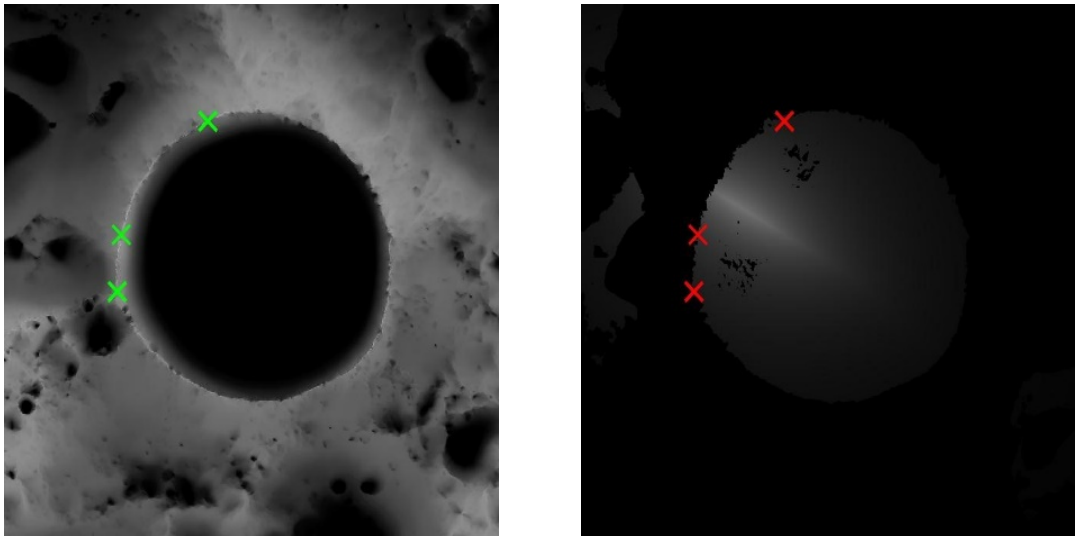

Figure 4.24. Location (left) and corresponding oasis map (right) for three reflectors placed 300 meters above ground level at 89.8172°S 153.5004°W, 89.8262°S 52.8422°E, and 89.6876°S 162.8645°W.

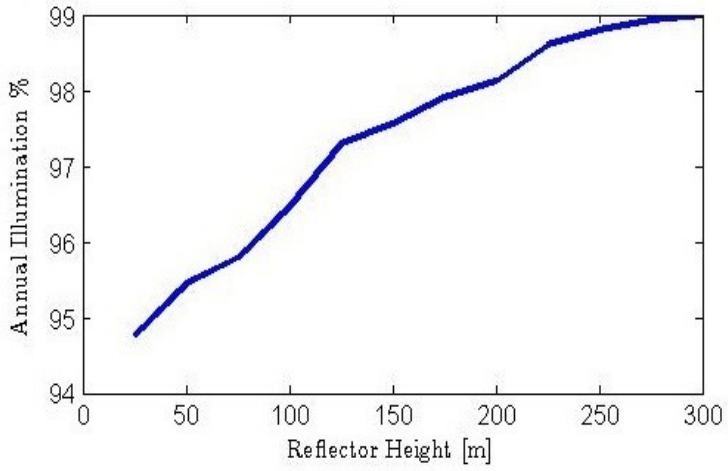

Figure 4.25. Annual illumination percentage vs. height for reflectors placed at locations.

Figure 4.26 illustrates how sunlight availability changes in the oasis region as reflector diameter is changed from 40 to 60 meters**.** This example demonstrates the trade-off between distance between reflectors and reflector size required to produce a usable energy oasis.

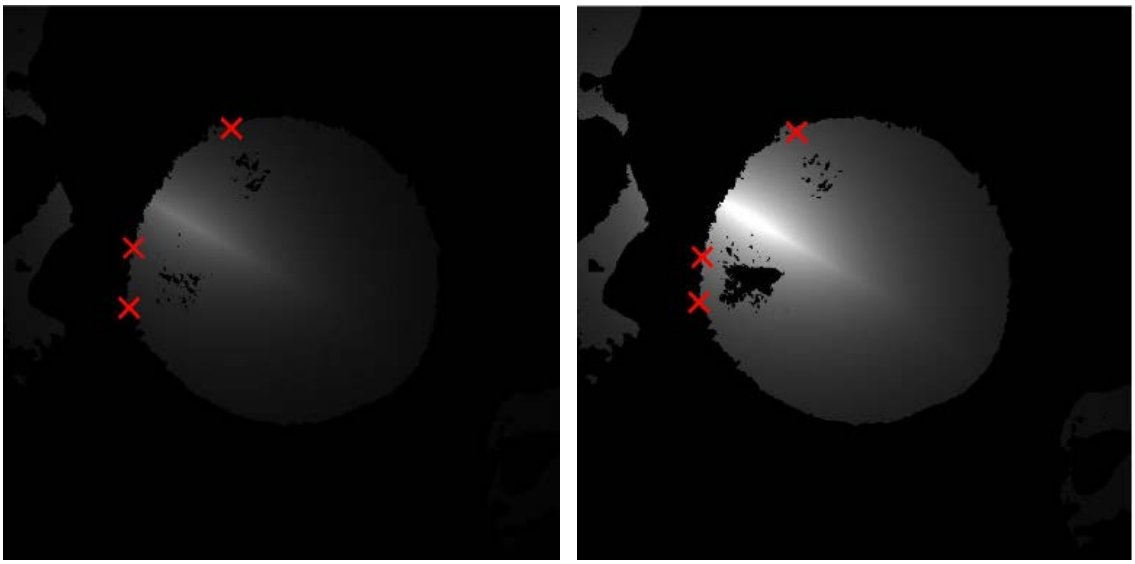

Figure 4.26. Illumination with 40m reflectors (left) vs 60 m reflectors (right)

4.5 Outside the Crater Illumination: the Western Ridge Infrastructure

All previously discussed results are limited strictly to the rim of Shackleton Crater. The connecting ridge just west of Shackleton Crater, however, offers additional near-continuous solar power solutions with their own strengths and weaknesses. **Figure 4.27** shows a solution in which three reflectors are able to achieve 99% annual illumination at a height of merely **25 meters**. For the solution involving three reflectors 25 meters above surface level, however, increasing reflector size would not improve conditions—the identified locations simply do not share line of sight with a sizable region of terrain. This solution is therefore poorly suited for a power infrastructure involving sunlight reflection and redirection, but it could prove useful for an alternate infrastructure involving solar power collection.

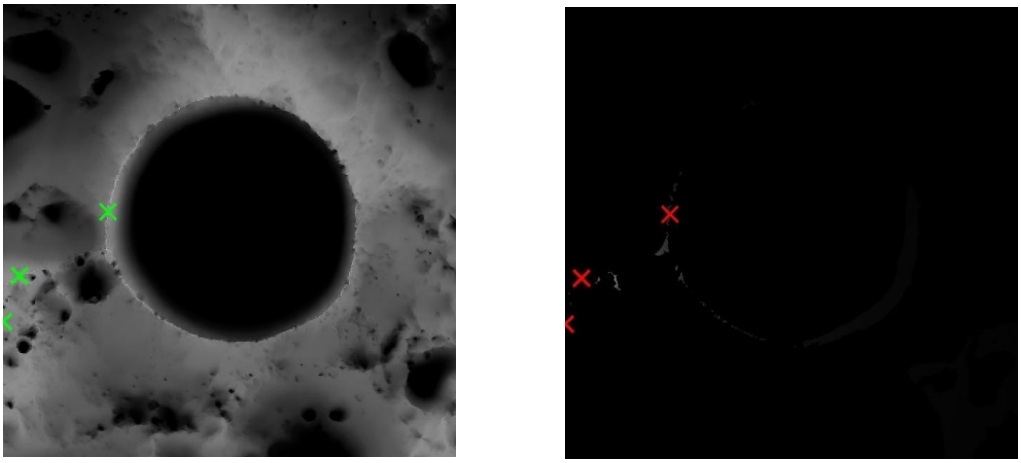

Figure 4.27. Location and corresponding oasis map for three reflectors placed 25 meters above ground level at 89.7860°S 155.6875°W, 89.3724°S 142.8592°E, and 89.4989°S 138.1404°W.

4.6 Extended Terrain Model and 65 m High Reflectors

While the initial terrain model covered ~5,000 km^2, this analysis uses an updated terrain model that includes Malapert Mountain and covers ~37,000 km^2 (**Figure 4.28**). The analysis maximizes 2020 sunlight availability for a specific scenario in which we considered a maximum of three reflectors, placed **65 m** above ground level.

The approach was as follows:

- Build improved 3D terrain model of lunar south pole
- Increase resolution of model around Shackleton Crater
- Increase size of region modeled to include Malapert and other distant peaks
- Generate new set of synthetic imagery
- Perform placement search at ground level
- Perform detailed analysis of identified location sets at 65 m above ground level
- To allow modeling of large areas, generation now accounts for curvature of the Moon

While narrower in focus, as this analysis only looks at locations which are 65 m above ground level, the analysis has the most accurate numbers, as they were obtained with the larger area and higher-resolution terrain map that includes Malapert Mountain.

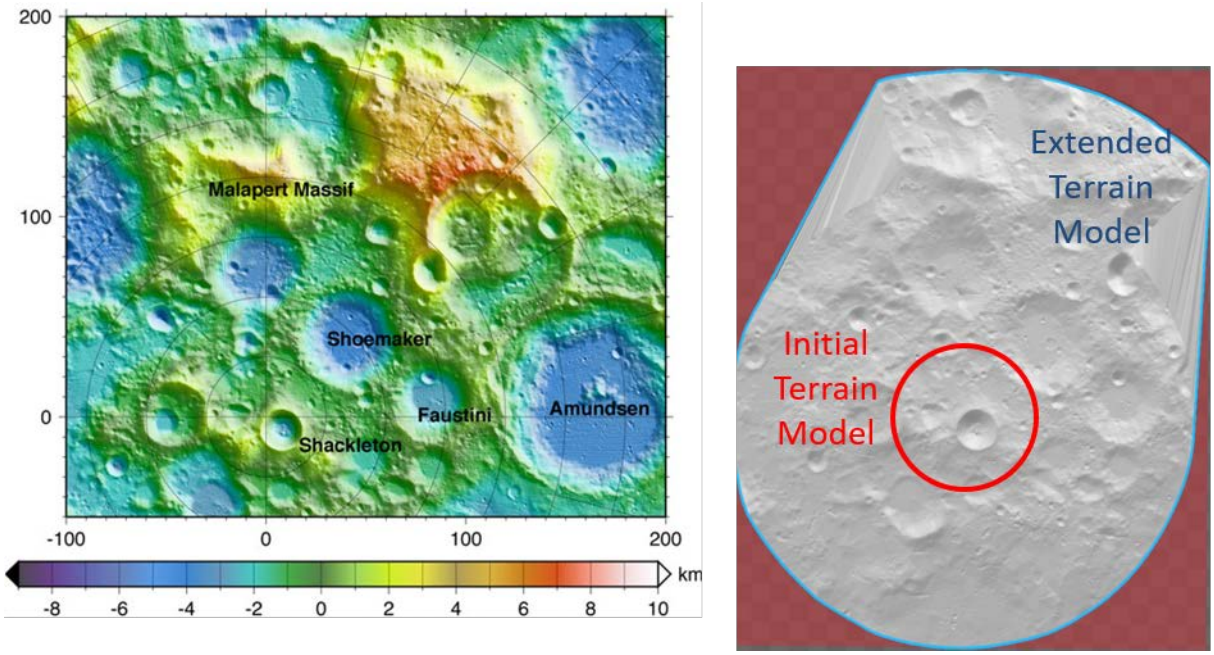

Figure 4.28. South pole region showing Shackleton Crater, and the initial terrain model of smaller area, around the crater, circled in red, and the much larger extended terrain model which included Malapert Mountain.

Figure 4.29 shows the updated synthetic imagery. A reduction in illumination is noticeable (we estimated ~1% reduction).

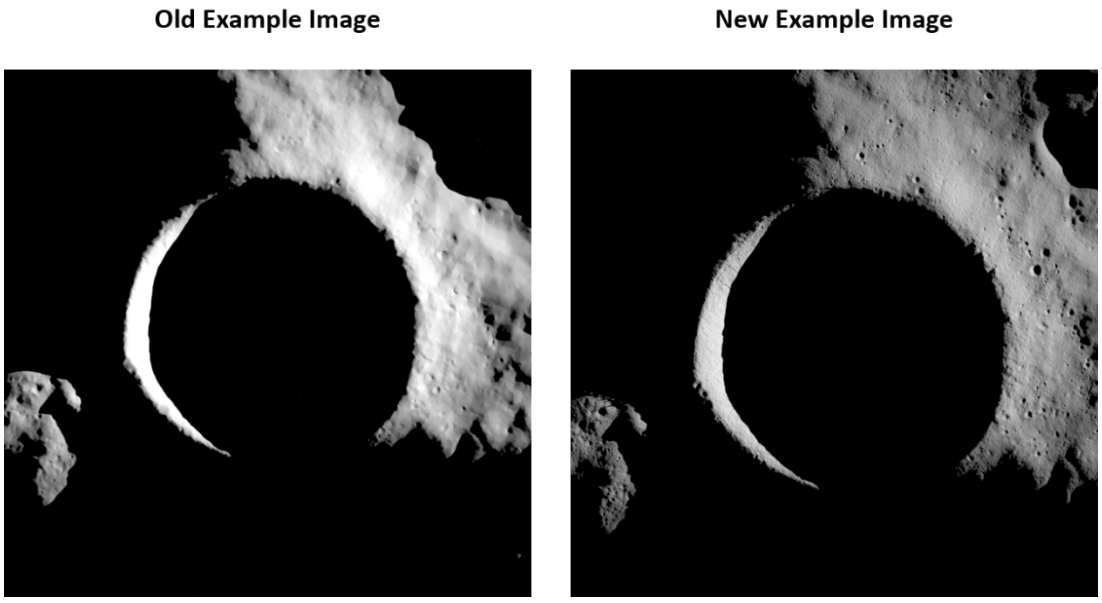

Figure 4.29. Comparison of illumination between the reduced terrain zone and extended topographical zone. One notices reduced illumination level as Sun is partly blocked by far away mountains

This Malapert "correction", which has reduced all our illumination numbers by about 1% (in points we have redone simulations), changed our terminology to "near-continuous".

4.6.1 *Single Reflector at 65 m Above Ground Level*

- **Location 1:**
  - 2020 illumination: **92.0%** (29.5 days in dark);
  - *Max continuous sunlight:* **4,013 hrs** (167.2 d);
  - *Max continuous darkness:* **61 hrs** (2.5 d)

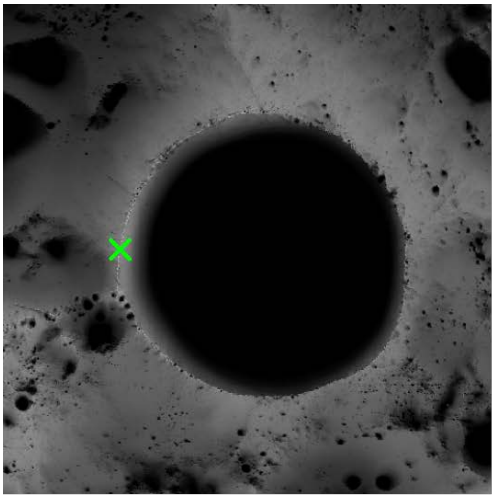

"Illumination": clear line of sight between point and **upper edge** of Sun

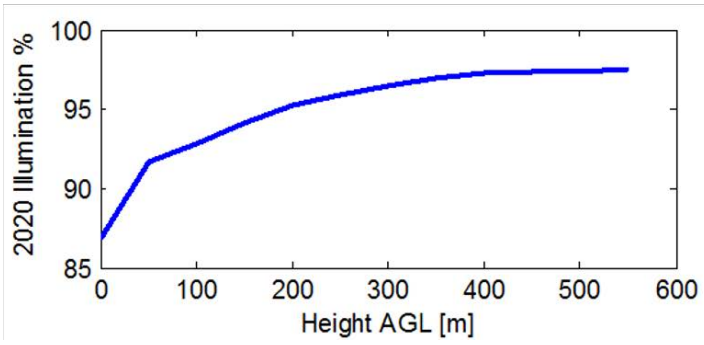

Figure 4.30. Point 1, best 65 m reflector location, and 2020 % of illumination for selected point as increases with height at that point.

Figure 4.31 shows a topographic map around Point 1. A further zoom-in is shown in **Figure 4.32**.

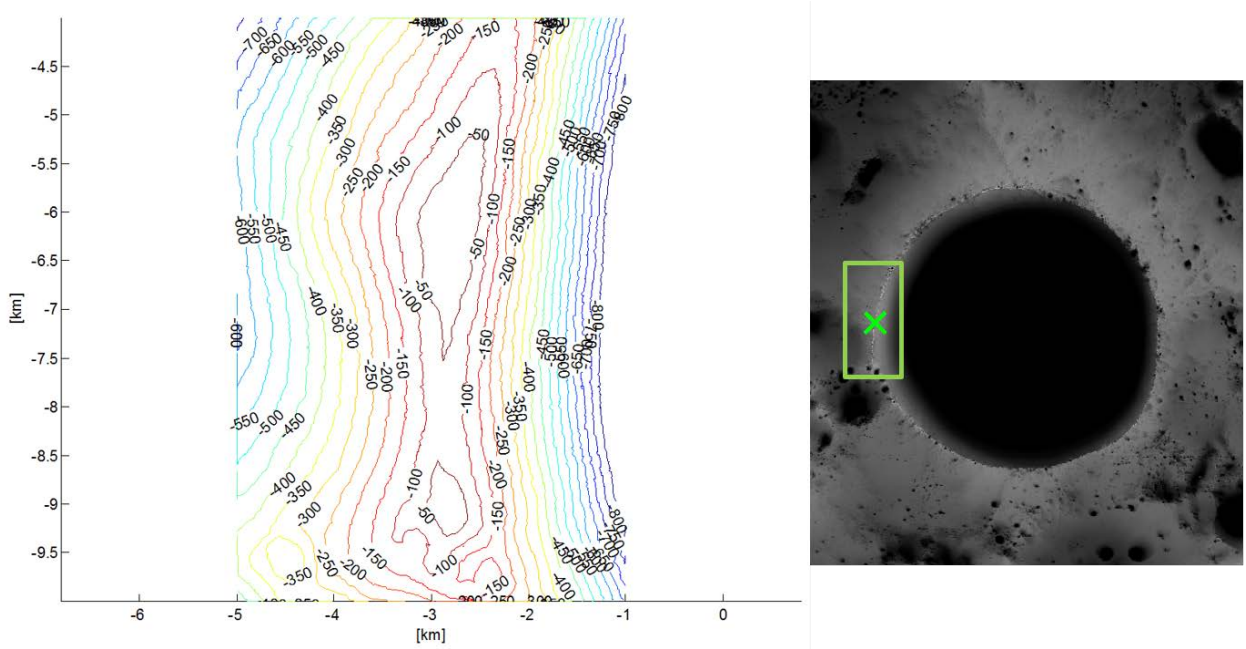

Figure 4.31. Topographic map of the region around Point 1 (for tower 1)

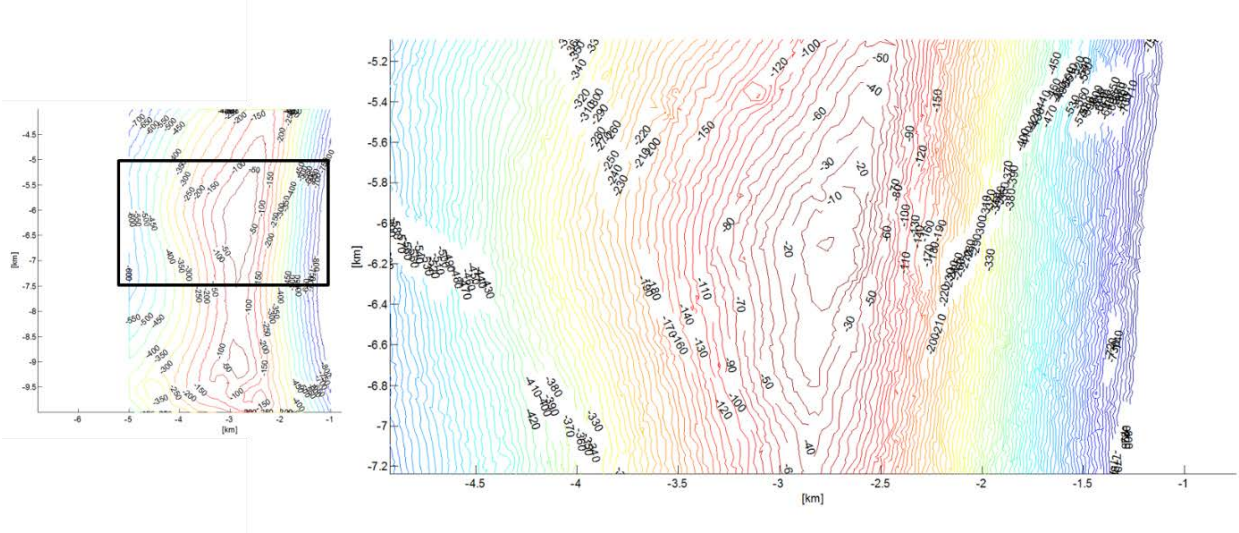

Figure 4.32. Zoom in of area around Point 1

4.6.2 *Two Reflectors at 65 m Above Ground Level*

- **Combined set:**
  - 2020 illumination: **95.9%** (14.8 days in dark)
  - Max continuous sunlight: **5,114 hrs** (213.1 d)
  - Max continuous darkness: **40 hrs** (1.7 d)

- Location 1:
  - 2020 illumination: **91.7%** (30.5 days in dark)
  - *Max continuous sunlight:* **4,008 hrs** (167.0 d)
  - *Max continuous darkness:* **63 hrs** (2.6 d)
- Location 2:
  - 2020 illumination: **77.6%** (82.0 days in dark)
  - *Max continuous sunlight:* **2,101 hrs** (87.5 d)
  - *Max continuous darkness:* **213 hrs** (8.9 d)

4.6.3 *Three Reflectors at 65 m Above Ground Level*

- **Combined set:**
  - 2020 illumination: **97.0%** (11.1 days in dark)
  - *Max continuous sunlight:* **5,119 hrs** (213.3 d)
  - *Max continuous darkness:* **35 hrs** (1.5 d)
- Location 1:
  - 2020 illumination: **92.0%** (29.5 days in dark)
  - *Max continuous sunlight:* **4,013 hr** (167.2 d)
  - *Max continuous darkness:* **61 hr** (2.5 d)
- Location 2:
  - 2020 illumination: **90.8%** (33.7 days in dark)
  - *Max continuous sunlight:* **3,980 hr** (165.8 d)
  - *Max continuous darkness:* **86 hr** (3.6 d)
- Location 3:
  - 2020 illumination: **79.2%** (76.2 days in dark)
  - *Max continuous sunlight:* **2,788 hrs** (116.2 d)
  - *Max continuous darkness:* **228 hr** (9.5 d)

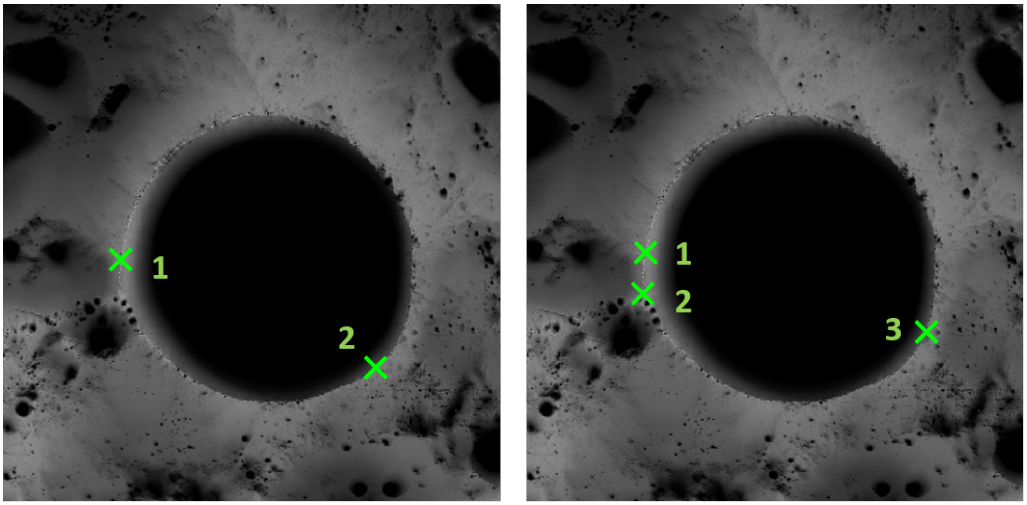

Figure 4.33. Best placement for 2 towers and 3 towers, respectively.

We illustrated that a combined set of three reflectors 65 m above the ground, at selected locations, would reduce the longest duration of darkness from 61 h, with one reflector, to 35 h. This shows how to obtain shortest duration for a given height/mass of a tower. Another way to formulate the optimization problem would be to determine the minimum infrastructure that would ensure fewer than "X" hours of darkness, which would depend on the capacity of an energy storage system.

4.7 Conclusions of the Illumination Studies

First, it is possible to obtain near-continuous (99% of the year) access to sunlight at the lunar south pole. Previous studies have identified locations in near-continuous sunlight at the lunar south pole, but this work has found several placement location and height *combinations* that allow for near-continuous access to sunlight in the year 2020. Second, the trade-off between location height and number of locations required to collectively achieve near-continuous access to sunlight on the rim of Shackleton Crater has been quantified—99% annual illumination can be achieved using three locations at a height of 300 meters, two at a height of 450 meters, or one at a height of 775 meters. Third, solar reflectors placed around the rim of Shackleton Crater would be capable of creating an energy oasis in which sunlight can be nearly continuously redirected. The size and power availability within the resulting oasis region has been shown to highly depend on solar reflector height, positioning, and size, but solutions exist. Finally, near-continuous solar power is achievable at near-ground level heights in the ridge region directly west of Shackleton Crater. A set of three locations 25 meters above ground level have been found in which at least one location is illuminated throughout 99% of the year 2020.

4.8 Lunar Eclipse and Need for Energy Storage

At least twice a year, the moon passes through the shadow cast by the Earth. First, the moon passes through the penumbra, where the Sun's light is only partially obscured. The penumbra results in only a slight darkening of the moon (~10%). The contribution to the irradiance comes both from direct and diffuse sunlight. The scattered photons (just refracted-bent) connects the solar disk with the Moon, illuminating it directly. Then it enters the umbra, and the Moon turns red. When the Moon is entirely in the umbra, this is called the totality phase. During this period of time, of 4 hr of eclipse, of which 1.7 hr is a total eclipse, the power infrastructure does not receive solar energy from the Sun and must rely on stored energy. Storage could be on batteries. An interesting alternative is thermal storage in a system that heats lunar, which is the lunar analogue to the Magaldi system prototyped on Earth.

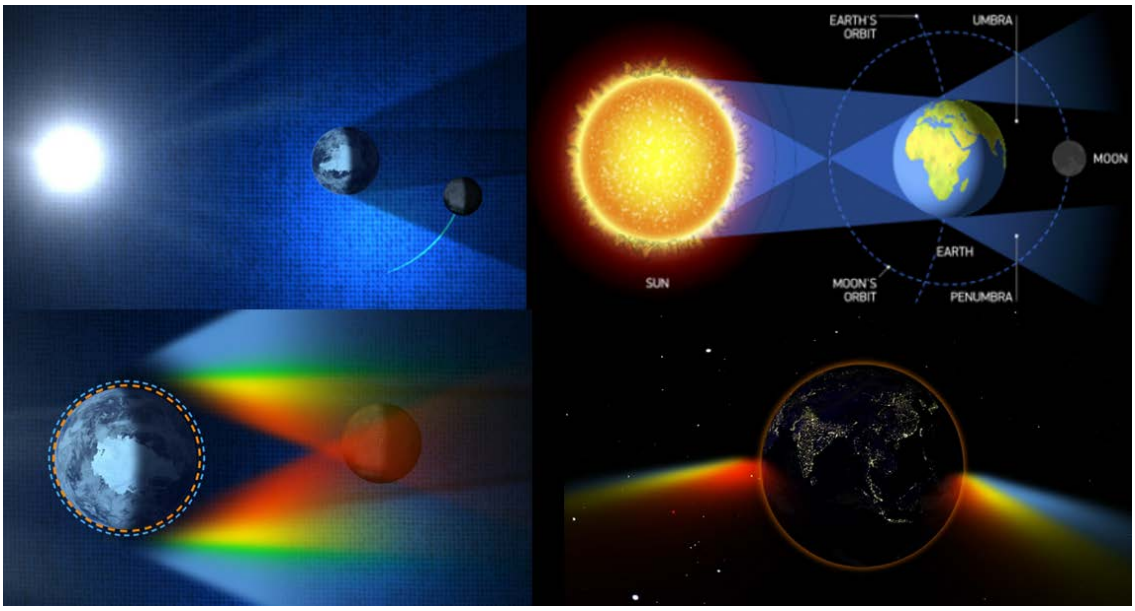

Figure 4.34. Moon in eclipse: Moon enters penumbra, then umbra, during which for about 1.7 hr, there is no sunlight as the Earth blocks Sun rays. An extremely small amount of scattered photons reach the Moon.

4.9 Communication to Earth

Shackleton Crater rim also has a favorable position for continuous communication with Earth. While the best visibility to some part of Earth is ~60% and the entire Earth is ~50% of the sidereal month, Shackleton Crater rim has direct LOS with the peaks of Malapert Alpha and Leibnitz Beta (about 120 km away), with 100% visibility of the Earth and can ensure a relay for continuous communication coverage to Earth (Bryant 2010).

Thus, the communication from SC rim to Earth would be via either direct or via relay (orbiter; or a relay on Malapert, 4.2 km elevation; or Leibnitz, 6.0 km elevation).

The recommendation for mid- to long-term is to use the continuous communication to Earth via a mountain relay, once the value of locations are confirmed. The recommendation for short-term is, however, to use the more affordable alternative of intermittent (60% of time) direct to Earth (DTE) communications, via TFs on the rim of SC, and further relaying communication through the infrastructure.

4.10 Node to Node Reflection or Beaming and an Extended Lunar Utilities Infrastructure

Reflecting or beaming energy node to node would ensure maintaining the thermal regime on TFs and may act as a relay transmission. **Figure 4.35** illustrates a ring of power with TFs beaming to each other around the crater rim.

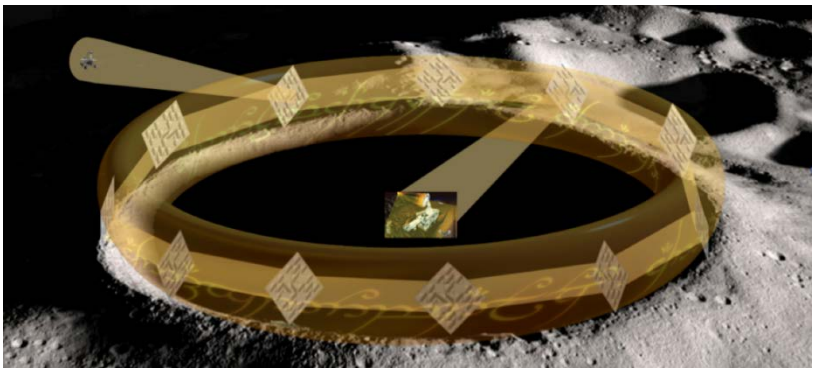

Figure 4.35. A "ring of power" vision for an energy infrastructure at the lunar south pole, with multiple reflecting TFs around Shackleton Crater beaming at each other and at rovers in the area.

Figure 4.36 illustrates the concept of a solar power infrastructure (SPI), which extends tens of km from south pole. SPI establishes the fundamentals of a new business model for lunar robotic missions, eliminating barriers of entry, lowering costs, and allowing incremental spending. Users would be able to execute missions without interrupts/hibernation. Robots could be deployed without RTGs, with limited thermal management, resulting in lower upfront costs (paying "as you go" only after confirmed successful landing).

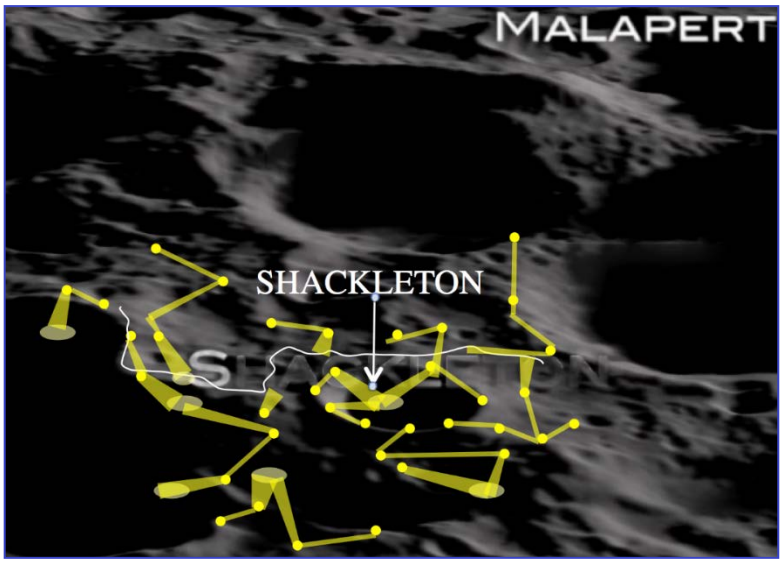

Figure 4.36. A lunar utilities infrastructure (LUI) built on a solar power infrastructure (SPI) extending for tens of kilometers around the solar south pole. The approximate extent is depicted as 100 × 100 km. SPI would heat and power many robots at the south pole and provide sunlight for successive missions for both NASA and its partners, for robots and humans. It would also serve as a communication/data infrastructure.

5 Conclusions

5.1 Summary of the Findings

This report documents the findings of the Phase II study entitled "TransFormers for Lunar Extreme Environments: Ensuring Long-Term Operations in Regions of Darkness and Low Temperatures". We met the goals set forth in the proposal and eliminated the main risks for advancing the concept. We have shown that it is possible to achieve continuous exploration and ISRU operations inside Shackleton Crater powered by a set of reflectors strategically placed on the rim. The reflective TransFormers would be placed in areas of abundant year-round solar illumination at the lunar south pole to redirect sunlight into shaded areas in their vicinity to power and warm up robotic systems operating in that area; relay communication is also provided. The specific scenarios are for prospecting rovers and for regolith processing, to obtain water from icy regolith in permanently shaded craters and from it the fuel for enabling sustainable travel to Mars.

The power needs to be provided by a lunar utilities infrastructure based on TFs are determined from the estimated needs for water. An affordable sustainable architecture of getting humans to Mars with lunar propellant was formulated, based on using 7.5 t/day of LH_2/LO_2 propellant, which translates to 10 t/day of ISRU water extracted at the lunar poles. In such a context, we determine power needs for prospecting, excavation, and processing of regolith. The estimated power needed (for 10% water in regolith) is ~0.6 MW for water extraction, and additional 2–4 MW electric power for obtaining the propellant. We targeted the design and trade-offs for the power infrastructure based on these values.

The rim of Shackleton Crater can sustain a lunar utilities infrastructure needed for such production. Multiple TFs would be needed, since no point on the rim receives year-round illumination, unless kilometers-tall towers are built, and then the reflector size would also increase to deal with the increase in transmission distance, at least for simple reflectors. Terrain maps using topographic data at ~10 meter level resolution were built based on LOLA data.

A search for pairs of points that together offered maximum received illumination was performed; the analysis determined locations where, at ground level and at a number of heights above ground, TF reflectors can be placed such that at least at one in the pair receives illumination during the entire year. For example, a single tower at 800 m at a point on the rim could receive ~99% illumination, or two towers of 400 m, or three towers of 300 m, etc. Scenarios of intermittent operation can be imagined, with a stop in production and hibernation of equipment; however, architectures including energy storage would be preferred, e.g., via batteries or other energy storage methods.

Tradeoffs on how the overall reflective surface is distributed are also considered. About 5,000 m^2 of surface could be realized in a single 80 m diameter reflector; alternatively, four 1250 m^2 surfaces of 40 m diameter reflectors could provide the same reflective area. Their placement is a matter of tradeoff. Mobile TFs have been considered, yet, especially as the towers get taller, the prospect of moving towers hundreds of meters tall on the rugged crater rim implies additional stability problems that are beyond the scope of this study; building smooth roads or rails may help.

Reflective surfaces from aluminized Kapton are presented and surfaces of 1,250 m^2 are shown to fit within 1 m^3. An inflatable tower 133 m tall could be packed within 10 m^3 and have a mass below 1,000 kg.

5.2 Broader Implications

5.2.1 *Collaborations*

Several close collaborations have been established through this work:

- **Collaboration Engagement with Texas A&M:** Co-I Prof. John Valasek provided oversight to graduate student James Henrickson. Jim has been instrumental to this study. He has spent over 6 months at JPL, funded by the NIAC and also by a Texas A&M Fellowship. Working with Adrian Stoica, Jim performed the illumination studies using LOLA data and implemented the algorithms searching for optimal pairs of TFs.
- **Collaboration with Joel Sercel, TransAstra:** Joel has been a consultant and developed an ISRU alternative.
- **Caltech Lunaport:** Caltech hosted a one week competition for formulating missions to the Moon. Adrian gave talks and mentored the 2 competing teams, both adopting a TransFormers inspired architecture for solar power. Adrian is still in contact with the alumni for bringing the vision to reality.

5.2.2 *Public Engagement, Media and Outreach*

- **Invited Talks** by Adrian Stoica at several Universities, including U. Oslo, Norway (where he also visited Rjukan and toured the mirror system on the mountain), U. Kyushu, Japan, U. Canterbury, UK
- **Media:**
  - Rick Stella (2015) “NASA wants to terraform the moon with a fleet of autonomous robots”
    - https://www.digitaltrends.com/cool-tech/nasa-is-considering-terraforming-the-moon-with-autonomous-robots/
  - Dyani Sabin (2016) “Giant Robot Mirrors Could Help Mine the Moon for Rocket Fuel”
    - https://www.inverse.com/article/20132-transforming-robot-mirrors-could-enable-lunar-mining
  - Jessica Hall (2017) “Liquid mirror: inside the temple planned for the Moon’s south pole”
    - https://www.extremetech.com/extreme/246778-liquid-mirror-inside-temple-planned-moons-south-pole
  - NASA Lunar Science Institute PodCast:
    - http://cosmoquest.org/blog/365daysofastronomy/2013/12/17/dec-17th-future-lunar-explorers-could-be-transformers/

5.2.3 *Contributions to Space Concepts*

The most important contributions of this Phase II study are as follows:

- The sustainable and affordable architecture for human travel to Mars with lunar propellant (Wilcox Architecture);
- The concept of a solar power infrastructure on the rim of SC to provide (collective) quasi-continuous solar illumination inside SC, and the extended version of the SPI, providing energy to tens of km around the south pole;
- The concept of a lunar utilities infrastructure, which extends the SPI with data communications.

Other important contributions include:

- The understanding that one can set the basis of both a first element of infrastructure and a first customer with a Discovery-class mission, which would accommodate a TF and a prospecting rover. The TF would provide power for the rover to explore inside a PSR on the Moon. This mission would prove the concept, return valuable science by confirming and characterizing the water in the PSR, and remain as a first node of infrastructure for use by future missions.
- Setting up the fundamentals of a new business model for lunar robotic missions, which eliminates barriers to entry, lowers costs, and allows incremental, periodic payments as opposed to upfront full payment at a time when is uncertain mission will land and deploy successfully. Thus,
  - Users would be able to execute missions without interrupts/hibernation.
  - Users would be able to send rovers without RTGs, and with only very limited thermal management; the costs for maintaining thermal regime and getting power will not happen when building the rovers, but will rather start only after confirmed successful landing of those rovers, with payments distributed over time, proportional to the level of power service provided.

5.2.4 *Publications*

Stoica (2014), A.; M. Ingham; L. Tamppari, et al., “Transformers for extreme environments NIAC phase I final report”, *NASA Institute for Advanced Concepts*, 2014.

Quadrelli (2015), M. B.; A. Stoica; M. Ingham; A. Thakur, “Flexible electronics-based TransFormers for extreme environments”, *SPACE and Astronautics Forum and Exposition*, AIAA, 2015.

Stoica (2016), A., “A lunar south pole solar power infrastructure”, *SPACE and Astronautics Forum and Exposition*, AIAA, 2016.

Henrickson (2016), J. & Stoica, A., “Optimal placement of solar reflectors at the lunar south pole”, *Proceedings of the 2016 IEEE International Conference on Systems, Man, and Cybernetics*, 2016.

Mantovani, J., Stoica A, Alkalai, L., Wilcox, B. Quadrelli M., and Ingham M., TransFormers for Ensuring Long Term Operations in Lunar Extreme Environments, Joint meeting of the Space Resources Roundtable, Inc. (SRR); 7th; 7–9 Jun. 2016; Golden, CO; United States, Joint meeting of the Planetary and Terrestrial Mining Sciences Symposium (PTMSS); 7th; 7–9 Jun. 2016; Golden, CO; United States

Henrickson (2017), J. & Stoica, A., "Reflector Placement for Providing Near-Continuous Solar Power to Robots in Shackleton Crater", *IEEE Aerospace Conference*, Big Sky, MT, 2017, doi: 10.1109/AERO.2017.7943944.

Salazar (2017), R.; Murthy, S.; Pellazar, C.; Stoica, A., "TransFormers for Lunar Extreme Environments: Large Origami Deployable Solar Reflectors", *IEEE Aerospace Conference*, Big Sky, MT, pp. 1–7, 2017, doi: 10.1109/AERO.2017.7943717.

Wilcox (2017), B., "An Architecture for Sustainable Human Exploration of Mars Enabled by Water from the Lunar Poles", *IEEE Aerospace Conference*, 2017, 10.1109/AERO.2017.7943895.

5.3 Technology Assessment and Increase in TRL

We estimate that we have matured this technology concept to close to TRL 3. To further advance the technology, funding through the NASA Space Technology Mission Directorate Game Changing Program will be sought, with the follow-on intent to prepare for a Discovery-class mission.

To further mature the TF technology, we would perform: a) a new round of simulations, with more precise parameters for chosen mission criteria (e.g., 300 days mission of a minimum of 300 W provided in an oasis within a specified perimeter, etc., with highest terrain resolution, etc.; simulations would take in consideration additional factors such as rigidization of the inflatable, variations in surface on which the towers are mounted, etc.; b) ground tech demos of TF folding/unfolding with origami methodologies, including photovoltaic cells to power themselves, redirecting sunlight in various environments; and c) microgravity demos of scaled versions of TFs unfolding in microgravity environments.

5.4 Recommendations

We recommend the preparation of a mission powered by a solar reflector placed on the rim of Shackleton Crater, for which the preliminary steps are:

- Build and test on Earth a fully functional TransFormer:
  - Use a reflective surface of ~10 m diameter to project power to a simple rover with solar panels, at ~1 km distance; place reflective surface in transparent enclosure with direct sunlight but no air movement (to avoid winds which would affect the structure on Earth, but do not exist on the Moon), use in low bandwidth/intermittent communication.
- Formulate a mission scenario at SC based on the TF/Prospector rover pair:
  - Landing would be outside the crater in the vicinity of the rim.
  - The rover would place the TF on the rim.
  - The rover would descend into SC only deep enough to reach the edge of the PSR. It would operate in and out of that region retreating often to the area at the edge where TF would project sunlight.
  - Once confidence in the operational capabilities and performance of the TF is built up, the Prospector rover could venture further into the PSR.

5.5 Vision of the Future

TransFormers introduce a new way of looking at missions in extreme environments, with the idea that we can control local zones of interest, creating favorable micro-environments within extreme environments. This works very well for robotic explorers, robotic mining, and processing of in-situ resources, providing a survivable region around them; it also works very well for human exploration as a safe means of warming up regions where astronauts would live and work. An entire region around a lunar base can be "climatized", receiving direct or indirect (through multiple reflections) sunlight, making the area habitable to humans and other terrestrial life.

We envision an infrastructure that will include solar energy capturing and redirecting nodes, energy storage nodes, transmission by multiple modalities including direct reflection, concentrated reflection, conversion and retransmission by microwave or laser, and receiving stations with warm up and battery charging capabilities. The infrastructure would be a benefit for all, as governments and private partners would join forces in an international scientific and economic cooperation on the Moon.

This lunar utilities infrastructure would in time extend over a region of tens of square kilometers, capturing or redirecting solar energy from many points receiving solar illumination, transmitting data locally and providing communications to Earth, facilitating the development of a lunar economic zone.

6 APPENDIX A: Wilcox Architecture Details

These are excerpts from (Wilcox, 2017), from which Figure A.1 was also taken. A simplified schematic of the figure was shown in **Figure 2.19** at page 2-21,

The self-propelled tanks fueled with LH_2/LO_2 on the moon departs for other places using an integrated rocket engine. We assume that the tanks are sized so that two such lander tank pairs could be filled by the ISRU infrastructure in each lunar sidereal month (27.3 days). This period is chosen so that the lander tank pairs can launch into any orbital plane desired because the moon has returned to the same position (relative to the fixed stars) as it had on the previous launch.

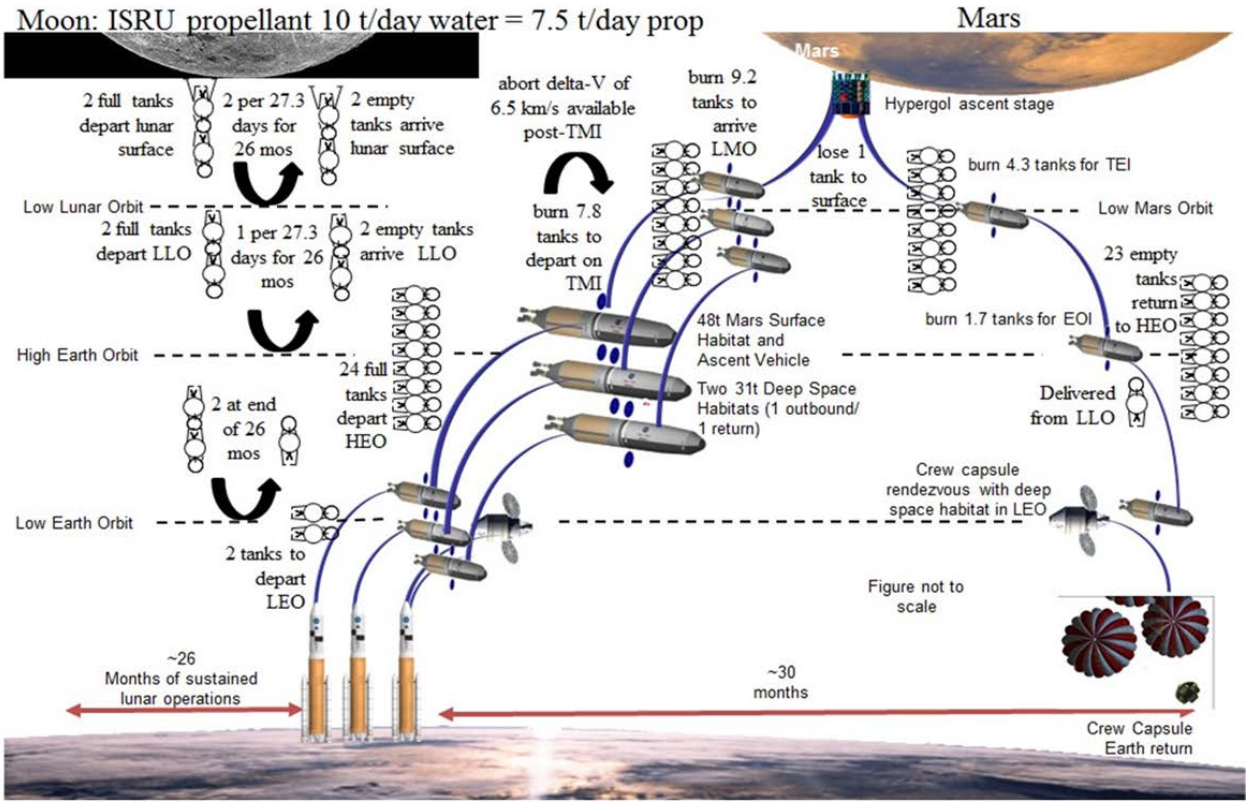

Figure A.1. "Bat Chart" showing logistical flow with time moving from left to right and spatial relationships bottom to top. Lunar propellant production proceeds continuously on 26-month cycles, delivering 24 full tanks to HEO as needed to propel payload stack to Mars and back.

Each sidereal month two lander tank pairs launch from a lunar polar crater. These two depart close enough together that, after a ΔV of 1.74 km/s, the two space-version tanks can separate from their lander-version first stages which performed the launch, and they mate together into a "spacetank-pair" as seen in the upper right of **Figure A.1**. The two lander-versions each rendezvous and mate with an empty space-version tank, and have enough propellant to de-orbit and land back at the ISRU plant in a configuration so the process can repeat endlessly.

The resulting spacetank-pair immediately departs Low Lunar Orbit (LLO) because the thermal environment of LLO is very unfavorable for maintaining zero boiloff due to the high temperature (~400 K) of the illuminated face of the moon. A High Earth Orbit (HEO) is chosen such that the spacetank-pair can expend most of the lower stage propellant in delivering a full

space-version tank to HEO, and yet have sufficient propellant in the tank to rendezvous with an empty tank at HEO and return to LLO so that both tanks are empty. They wait in LLO until the next two lander-tank pairs launch from the lunar pole, where they become the next pair of "empties" to return to the surface for refueling. The ΔV that accomplishes this (having 2 full tanks depart LLO with one full tank arriving HEO and two empty tanks arriving LLO) is 1.87 km/s from the LLO orbit.

This architecture accumulates space-version tanks in HEO for future use. Occasionally, it will be desired to ferry hardware launched from Earth up from Low Earth Orbit (LEO) to HEO. For that occasion, two full space-version tanks will be mated together, and the lower one with provide 2.10 km/s ΔV to the stack to get to LEO, where the full upper tank will separate and the lower "booster" tank will still have enough propellant to return to HEO, arriving empty. In this architecture, we thus have ΔV assumptions of 2.10 km/s to get between LEO and HEO, 1.87 km/s to get between HEO and LLO, and 1.74 km/s to get from LLO to the lunar surface. This is a total of 5.71 km/s to go from LEO to the lunar surface, a bit in excess of the difference between Earth escape velocity and Earth orbital velocity (3.27 km/s) added to lunar escape velocity (2.38 km/s, for a combined total of 5.65 km/s). We also see that our assumed launch ΔV from the lunar surface into LLO is slightly more than the minimum 2-1/2 times lunar escape velocity, as required by orbital mechanics to allow at least one complete orbit around the moon. Additional margin could be provided for the ΔVs in getting from LEO to HEO and from HEO to LLO by raising the LEO orbit where payloads from Earth are deposited. Any further margin must be provided by improving the PMF of the two variants of the standardized self-propelled tanks without sacrificing the zero-boiloff capability. This is because we have assumed integer deliveries: 2 tanks launch from the lunar surface to deliver 1 full tank to LLO (returning 2 empty to the surface); 2 tanks depart LLO to deliver 1 full tank to HEO (returning 2 empty to LLO); two full tanks depart HEO to deliver 1 full tank to LEO (returning 1 empty to HEO).

Minimum-energy Hohmann transfer opportunities happen every 29.0 sidereal lunar months (26.0 solar months). Our architecture launches two lander-tank-pairs every sidereal month, resulting in one full tank arriving in HEO. So a total of 29 full tanks arrive in HEO for use in the Human-Mars Exploration Architecture.

Of these 29 tanks, we plan to use 24 to launch a stack of payloads from HEO by way of an Oberth Maneuver at the top of the Earth's atmosphere. The payloads would originally be launched from Earth into LEO. Four additional tanks in HEO are sent to LEO to pick up these payloads and bring them to HEO. (As previously mentioned, one space-tank pair can deliver one fully-fueled nominal mission, the outbound DSH and the spent Mars Ascent Vehicle (MAV) will be left mated together in Low Mars Orbit (LMO), the Mars Habitat will be left on the surface of Mars, and the other DSH will return with 23 of the 24 space-version tanks to HEO for re-fueling and re-use.

The one space-version tank not returned from Mars back to HEO is used to de-orbit the MSHAV. The ΔV to "stop and drop" from LMO is 4.1 km/s. For the space-version tank we have conceived here, the payload that one such tank can push through this ΔV is 48.4 t. So we assume the mass of the MSHAV is 48.4 t, including any landing gear, terminal propulsion, and/or other systems required to get the payload safely on the surface after separation from the space-version tank at zero relative velocity with respect to the Mars surface. The one space-version tank used for this maneuver crashes onto Mars.

Iterative calculations show that, using 24 fully-fueled space-version tanks to depart HEO, and given that the MSHAV has a mass of 48.4 t, then the two DSH's each could have a mass

departing HEO of up to 30.6 t each, with one DSH and 23 empty tanks arriving back in HEO at the end of the mission. The masses and ΔVs associated with each maneuver over the mission are shown in Table 1.

One nice feature is that, following TMI, there is abundant propellant to perform a direct-return abort of the stack. If the crew were to re-arrange the stack to preserve only those tanks which are full and one deep-space habitat, they could abort back to Earth with 6.48 km/s of ΔV available to get onto an Earth-intercept trajectory and to perform Earth-Orbit Insertion.

Of course a minimum of two such lander-version tanks are needed for this architecture, so this would put almost 6.4 t of whatever mass is needed for the ISRU infrastructure on the moon. We might imagine that we could emplace some small ISRU "unit" which is capable of slowly fueling the standardized tanks. Ultimately we need to get to a production rate of 10 t/day of water or 7.5 t/day of fuel, but in the cold, dark lunar polar crater it is possible that we could fuel the tanks much more slowly than that during the bootstrapping process. So we might imagine that the initial 6.4 t of equipment we could land might represent this minimum-rate but "complete" ISRU plant, in the sense that it is capable of mining the regolith, extracting the water, and processing it into LH_2/LO_2.

The dry mass of a space-version of the tank is 9.0 t. Loaded with 12.3 t of propellant, it could reach LLO from LEO, arriving empty. The total launch mass is 21.4 t, slightly less than the catalog launch capacity of the Falcon 9 (22.8 t). Both for this case and the launch of the lander version on the Falcon Heavy, we have not considered the shroud volume, launch adapter, or similar issues. The two lander version tanks that arrive at the moon would offload their payloads (presumably the equipment needed for such offloading is included in the 6.4 t equipment mass). Those payloads would then begin to fill the two lander-version tanks. Even before they are completely full, they could ascend to LLO and pick up two space-version tanks launched on Falcon-9s and bring them to the surface. At that point the architecture could begin stockpiling, if slowly, full space-version tanks in HEO. As fast as full tanks arrive in HEO, they would need to be replenished via launches of Falcon-9s.

7 Bibliography

Al-Jammaz (2004), K.; A. Diaz; F. Hernandez; et al., "Elements for a sustainable lunar colony in the south polar region", *Science and Technology Series*, vol. 108, pp. 515–527, 2004.

Andreas (2007), E. L., "New estimates for the sublimation rate for ice on the Moon", *Icarus*, vol. 186, Issue 1, pp. 24-30, 2007.

Andrews, D. R. (2014), Colaprete, A., Quinn, J. et al "Introducing the Resource Prospector (RP) Mission", AIAA SPACE 2014 Conference and Exposition, AIAA SPACE Forum, (AIAA 2014-4378)

Anthony (2008), W. Y., Novo-Gradac, A. M., Shaw, G. B., "Lunar transmitter for the lunar orbit laser altimeter (LOLA) instrument", *Conference on Lasers and Electro-Optics*, 2008.

Bar-Cohen (1999), Y. "Electroactive Polymer (EAP) Actuating a Dust Wiper Miniature Robotic Arm", *SPIE Newsletter*, International Technical Group on Robotics and Machine Perception, 1999.

Bar-Cohen (2001), Y., "Electroactive Polymers as Artificial Muscles - Reality and Challenges", *42nd AIAA Structures, Structural Dynamics, and Material Conference*, 2001.

Braeunig, "Liquid Oxygen & Liquid Hydrogen", Online resource, [last accessed: 11/10/2017], http://www.braeunig.us/space/comb-OH.htm.

Bryant (2009), S., "Lunar Pole Illumination and Communications Maps Computed from Goldstone Solar System Radar Elevation Data", *The Interplanetary Network Progress Report*, vol. 42-176, 2009, http://ipnpr.jpl.nasa.gov/progress_report/42-176/176C.pdf.

Bryant S. (2010), "Lunar Pole Illumination and Communications Statistics Computer from GSSR Elevation Data", *SpaceOps* 2010, Conference, Huntsville, AIAA-2010-1913.

Bussey (1999), D. B. J.; Spudis, P. D.; Robinson, M. S.; "Illumination conditions at the lunar south pole", *Geophysical Research Letters*, vol. 26, no. 9, pp. 1187–1190, 1999, doi: 10.1029/1999GL900213.

Bussey (2003), D. B. J.; Lucey, P. G.; Steutel, Donovan; et al., "Permanent shadow in simple craters near the lunar poles", *Geophysical Research Letters*, vol. 30, Issue 6, pp. 11-1, 2003, doi:10.1029/2002GL016180.

Bussey (2010), D.; J. McGovern; P. Spudis, et al., "Illumination conditions of the south pole of the moon derived using kaguya topography", *Icarus*, vol. 208, no. 2, pp. 558–564, 2010.

Colaprete, A.; R. C. Elphic; W. M. Farrell; et al., "Lunar Polar Volatiles: Assessment of Existing Observations for Exploration", *Online* resource, [last accessed: 11/10/2017], https://ssed.gsfc.nasa.gov/dream/docs/PolarVolatiles_HEOMD_Hurley.pdf

Collier (2013), M. R.; W. M. Farrell; T. J. Stubbs, "The lunar dust pendulum", *Advances in Space Research*, 52.2, pp. 251-261, 2013.

CottonInfo, "Fundamentals of energy use in water pumping", *Online resource*, http://www.cottoninfo.com.au/sites/default/files/documents/Fundamentals%20EnergyFS_A_3a.pdf, [last accessed: 11/10/2017]

Crump (2008), et al, "Mode Control for High Performance Laser Diode Sources", *nLight Corp*, Vancouver, WA, 2008.

Dawson (2004), S.; Mardesich, N.; Spence, B.; While, S.; "Solar Array Panels with Dust-Removal Capability", *NASA Tech Briefs*, Pasadena, 2004.

De Rosa (2012), D., et al. "Characterisation of potential landing sites for the European Space Agency's Lunar Lander project", *Planetary and Space Science*, 74.1, pp. 224–246, 2012.

Dominguez (2017), J. A., et al., "Comprehensive Modeling of Superficial Dust Removal via Electrostatic and Dielectrophoretic Forces in Extraterrestrial Exploration Mission", *Annual Meeting of the Electrostatics of America*, Ottawa, Ontario, 2017.

ESA, "Smart-1 view of shackleton crater at lunar south pole", *Online resource*, http://goo.gl/bNmh7d, [last accessed: 11/11/2017]

Feldman (2001), W. C.; S. Maurice; D. J. Lawrence; et al., "Evidence for water ice near the lunar poles", *J. Geophys Res*., 106, pp. 23,231–23,251, 2001.

Giorgini (1998), J.; Yeomans, D.; Chamberlin, A. et al., "Horizons, JPL's on-line solar system data and ephemeris computation service", *Users guide*, 1998.

Gläser (2014), P.; Scholten, F.; De Rosa, D., et al., "Illumination conditions at the lunar south pole using high resolution digital terrain models from LOLA", *Icarus*, vol. 243, pp. 78–90, 2014.

Glassner (1989), A. S., "An introduction to ray tracing", *Elsevier*, ISBN: 9780122861604.

Governale (2017), G., "Lunar south pole thermal modeling and analysis: satellite topographic data and terrain thermal properties integration", *Master thesis*, JPL, 2017.

Hayne (2015), P. O.; A. Hendrix; E. Sefton-Nash, et al., "Evidence for exposed water ice in the Moon's south polar regions from Lunar Reconnaissance Orbiter ultraviolet albedo and temperature measurements", *Icarus*, vol. 255, pp. 58-69, doi:10.1016/j.icarus.2015.03.032.

Henrickson (2016), J. & Stoica, A., "Optimal placement of solar reflectors at the lunar south pole", *Proceedings of the 2016 IEEE International Conference on Systems, Man, and Cybernetics*, 2016.

Henrickson (2017), J. & Stoica, A., "Reflector Placement for Providing Near-Continuous Solar Power to Robots in Shackleton Crater", *IEEE Aerospace Conference*, Big Sky, MT, 2017, doi: 10.1109/AERO.2017.7943944.

Johansen (2017), M. R. et al., "History and Flight Development of the Electrodynamic Dust Shield", *Kennedy Space Center*, FL, 32899, USA: NASA, 2017.

JPL (2006), "MSL Solar Feasibility Study", *Jet Propulsion Laboratory, JPL D-33463*, Pasadena, CA. March 20, 2006.

Koenning, T. P.; H. G. Treusch, "Power Beaming with Diode Lasers", *Dilas Online Assets*, http://dilas.com/assets/media/whitepapers/DILAS_SSDLTR_08_Power_Beaming_with_Diode_Lasers.pdf, [last accessed: 11/10/2017].

Landis (2002), G. A. & Jenkins, P. P., "Dust Mitigation for Mars Solar Arrays", *IEEE*, 2002.

Larson, Thomas K. (1999), Zuppero, Anthony C. Schnitzler, Bruce G. et al. “Origin of How Steam Rockets can Reduce Space Transport Cost by Orders of Magnitude”, “Space Technology & Applications International Forum (STAIF-99)”, Jan 31, 1999 to Feb 4, 1999 in Albuquerque: “16th Symposium on Space Nuclear Power and Propulsion” Session: “Affordable Space Fission Power and Propulsion” http://neofuel.com/moonice1000/

Lavoie (2016), T.; P. D. Spudis, “The Purpose of Human Spaceflight and a Lunar Architecture to Explore the Potential of Resource Utilization”, *AIAA SPACE Forum*, 2016, doi:10.2514/6.2016-5526.

Mackey (2016), P. J., et al., “Electrodynamic Dust Shield for Space Application”, *ASCE Earth and Space Conference*, Orlando, FL, USA, 2016.

Magaldi (2015), M.; De Michele, P. S., “Device and method for storage and transfer of thermal energy originated from solar radiation based on fluidization of a bed of particles”, *USA Patent, (US 8,960,182 B2)*, 2015.

Maghanga (2011), Christopher M., et al. "Spectrally selective reflector surfaces for heat reduction in concentrator solar cells: modeling and applications of TiO2:Nb-based thin films", *Applied optics*, 50.19, pp. 3296–3302, 2011.

Margiotta (2010), D. V., et al., “The Lotus Coating for Space Exploration: a Dust Mitigation Tool”, *SPIE Proceedings*, 2010.

Margiotta (2011), D. V., et al., “Desert Research and Technology Studies Exposure of Lotus Coated Electrodynamic Shield samples”, *AIAA 3rd Atmospheric Space Environment Conference*, 2011.

McNatt (2016), J.; Landis, G., “Design of Photovoltaic Power System for a Precursor Mission for Human Exploration of Mars”, *IEEE Photovoltaic Specialists Conference (PVSC)*, 43rd, 2016.

Miller (2014); D. J. Lawrence; D. M. Hurley, “Identification of surface hydrogen enhancements within the moons Shackleton Crater”, *Icarus*, vol. 233, pp. 229–232, 2014.

MSL (2006) “MSL Solar Feasibility Study”, JPL, 2006. Jet Propulsion Laboratory. JPL D-33463, Pasadena, CA. March 20, 2006.

NASA (2006) “Final Environmental Impact Statement for the Mars Science Laboratory Mission”, Vol 1, NASA 2006, https://nnsa.energy.gov/sites/default/files/nnsa/multiplefiles2/NASA%202006%20Mars%20SL-FEIS%20Vol%201%20&%202.pdf

NASA, “Mars Fact Sheet”, *Online resource*, [last accessed: 11/10/2017], https://nssdc.gsfc.nasa.gov/planetary/factsheet/marsfact.html.

NASA Space Technology Roadmaps, *Online resource*, [last accessed: 11/10/2017], http://www.nasa.gov/offices/oct/home/roadmaps/.

Nozette (2001), S.; P. D. Spudis; M. Robinson, et al., “Integration of lunar polar remote-sensing data sets: Evidence for ice at the lunar south pole”, *J. Geophys. Res.*, vol. 106, pp. 23,252–23,266, 2001.

S. Nozette, (2007), S., P.D. Spudis, B. Bussey, and J. Plescia, "The strategic value of robotic precursors to human lunar polar exploration", Workshop on Science associated with lunar exploration architecture. Feb-March, 2007, https://www.lpi.usra.edu/meetings/LEA/whitepapers/Nozette_polar_strategy_FINAL.pdf

O'Connor (2015), K. & Abraham, N., "Lotus Coating, Mitigating Surface Contamination", *NASA Tech Briefs Webinar*, 2015.

Ohandley (2001), D. A.; E. E. Rice; R. J. Gustafson, "ISRU support for a self-sustaining lunar colony (SSLC)", *39th AIAA Aerospace Sciences Meeting and Exhibit*, vol. 3, 2001.

Overton, G., "Cryolasers target >80% power conversion efficiency", *Online resource*, http://www.laserfocusworld.com/articles/print/volume-49/issue-10/newsbreaks/cryolasers-target-80-power-conversion-efficiency.html, [last accessed: 11/10/2017]

Quadrelli (2015), M. B.; A. Stoica; M. Ingham; A. Thankur, "Flexible electronics-based transformers for extreme environments", *SPACE and Astronautics Forum and Exposition*, AIAA, 2015.

Riris (2007), H.; Sun, X.; Cavanaugh, J. F., et al., "The lunar orbiter laser altimeter (LOLA) on NASA's lunar reconnaissance orbiter (LRO) mission", *Defense and Security Symposium*, International Society for Optics and Photonics, 2007.

Ritcher (1993), S. W., "Experimental Determination of in Situ Utilization of Lunar Regolith for Thermal Energy Storage", NASA, Final Technical Report, NSA 1.26:191050, https://ntrs.nasa.gov/search.jsp?R=19930007428

Sanin (2017), A. B.; I. G. Mitrofanov; M. L. Litvak, et al., "Hydrogen distribution in the lunar polar regions", *Icarus*, vol. 283, pp. 20–30, 2017.

Schnitzler, (1997) Bruce G.; Zuppero, Anthony C, Thomas K. Larson, "Nuclear-heated steam rocket using lunar ice", AIAA 97-3172, 33rd AIAA/ASME/SAE/ASEE Joint Propulsion Conference & Exhibit July 6–9, 1997 / Seattle, WA, http://neofuel.com/moonicerocket/

Schrunk (2007), D. G.; B. L. Sharpe; B. L. Cooper; M. Thangevelu, "The first lunar base", *The Moon: Resources, Future Development, and Settlement*, pp. 83–95, 2007.

Sercel, Joel, and Peterson, Craig, "Power Requirements Estimate for Lunar Ice ISRU", *TransAstra Technical Report*.

Smith (2010), D. E.; Zuber, M. T.; Neumann, G. A., et al., "Initial observations from the lunar orbiter laser altimeter (LOLA)", *Geophysical Research Letters*, vol. 37, no. 18, 2010.

Spudis (2010), P. D., et al., "Initial results for the north pole of the Moon from Mini-SAR, Chandrayaan-1 mission", *Geophysical Research Letters*, vol. 37, Issue 6, L06204, doi:10.1029/2009GL042259.

Spudis (2010), P. D.; T. Lavoie, "Mission and Implementation of an Affordable Lunar Return", Submitted to Space Manufacturing 14, *Online resource*, http://www.spudislunarresources.com/Papers/Affordable_Lunar_Base.pdf.

Spudis (2013), P. D.; D. B. J. Bussey; S.M. Baloga, et al., "Evidence for water ice on the Moon: Results for anomalous polar craters from the LRO Mini-RF imaging radar", *J. of Geophys. Res.: Planets*, vol. 118, pp. 2016–2029, doi:10.1002/jgre.20156, 2013.

Spudis (2016), P. D., "The Value of the Moon", *Smithsonian Books*, ISBN: 9781588345035.

Stoica (2014), A.; M. Ingham; L. Tamppari, et al., "Transformers for extreme environments NIAC phase I final report", *NASA Institute for Advanced Concepts*, 2014.

Stoica (2016), A., "A lunar south pole solar power infrastructure", *SPACE and Astronautics Forum and Exposition*, AIAA, 2016.

Sims (2003), R. A., et al. "Development of a transparent self-cleaning dust shield for solar panels." *Proceedings ESA-IEEE joint meeting on electrostatics*. 2003

Slavík (1996), P., "A tight analysis of the greedy algorithm for set cover", *Proceedings of the twenty-eight annual ACM symposium on Theory of computing*, ACM, pp. 435–441, 1996.

Stankie (2014), C. G., "Electrodynamic Dust Shield Demonstrator", *Final report: Lunar and planetary science and exploration*, presentation, 2014.

Thomson (2012), B.; D. Bussey; C. Neish, et al., "An upper limit for ice in Shackleton Crater as revealed by LRO mini-RF orbital radar", *Geophysical Research Letters*, vol. 39, no. 14, 2012.

Vasavada (1999), A. R.; D. A. Paige; S. E. Wood, "Near-Surface Temperatures on Mercury and the Moon and the Stability of Polar Ice Deposits", *Icarus*, vol. 141, pp. 179–193, 1999.

Vondrak (2010), R.; Keller, J.; Chin, G.; Garvin, J., "Lunar reconnaissance orbiter (LRO): observations for lunar exploration and science", Space Science Reviews, vol 150, no. 1-4, pp. 7–22, 2010, doi:10.1007/s11214-010-9631-5

David Wettergreen, (2014) Nomadic Exploration: Following routes of solar sustenance and temperate climate, NIAC 2014 Symposium, Cocoa Beach, FL, 2014

Wilcox (2007), Brian H, Litwin, Todd E., et al. "ATHLETE: A cargo handling and manipulation robot for the moon", Journal of Field Robotics, Volume 24, Issue 5 (May 2007) Special Issue on Space Robotics, Part III, pp. 421–434.

Wilcox (2017), B., "An Architecture for Sustainable Human Exploration of Mars Enabled by Water from the Lunar Poles", *IEEE Aerospace Conference*, 2017

Wikipedia, "Oberth Effect", *Online resource*, https://en.wikipedia.org/wiki/Oberth_effect

Williams, D. R., "Ice on the moon: a Summary of Clementine and Lunar Prospector Results", *Online resource*, https://nssdc.gsfc.nasa.gov/planetary/ice/ice_moon.html [last accessed: 11/10/2017]

Zuber (2012), M. T.; J. W. Head; D. E. Smith, et al., "Constraints on the volatile distribution within Shackleton Crater at the lunar south pole", *Nature*, vol. 486, no. 7403, pp. 378–381, 2012.

Zuppero, A. (2005) Propulsion to Moons of Jupiter Using Heat and Water Without Electrolysis Or Cryogenics, Space Exploration, 2005

8 Acknowledgement of Support

Many thanks to all who made this study possible, and who are acknowledged in the following.

Experts and Academics:

- David Evans, Chairman of DSEA Group, Dundee UK for coordinating the creation of a set of videos related to TransFormers; thanks to the anonymous UK students who did the animations;
- Jim Torresen, U. Oslo, Norway, for hosting Adrian Stoica, and organizing his viewing of the reflecting mirrors at Rjukan;
- Robert Skelton, TAMU, for insightful discussions and sharing his great knowledge and passion for tensegrity systems;
- Robert Shishko, JPL, for sharing his knowledge and enthusiasm about lunar missions and economics of space missions;
- Saptarshi Bandyopadhyay, Jean Pierre De la Croix, and other colleagues in the robotics section at JPL, for their review of the report and for their comments.

Students, who had an important contribution in simulations and experimental research:

- Giuseppe Governale, for performing thermal analysis for TransFormers illuminated on the rim and for the ground of Shackleton Crater and robotic equipment illuminated by TransFormers while operating in the crater; Giuseppe also analyzed the lunar eclipses and the Magaldi system and its applicability to the Moon;
- Sheila Murthy and Chase Pellazar, for theoretical and experimental work with reflectors;
- Keenan Albee, Benjamin Donitz, Seth Eisner, Leon Kim, Hunter Hall, Matthew Howard, Dakota Pierce, Divya Srivastava, and Yvonne Villapudua for participating in an A-team exercise and brainstorming related to using a power infrastructure to enable a lunar economy.

Other collaborators:

- JPL management for their suggestions during the review and for their support during this study;
- Mary Young and Samantha Ozyildirim of JPL, for their help in bringing this report to correct expression and proper form, much appreciated;
- Juliana Echternach, University of Southern California and Luigi Mascolo, University of Turin, JPL interns, for their help with editorial and technical verification support;
- Michelle Judd, the Managing Director Caltech's Keck Institute of Space Studies (KISS) for the initial support during the 2014–2015 KISS Workshop and her support ever since;
- Ilana Gatt, Caltech, for getting Adrian Stoica involved as a mentor and expert in the 2017 Caltech Space Challenge, a 5-day international student space mission design competition at Caltech, focused on the LunaPort, which is a launch and supply station for deep space missions.